VELOCITY DEPENDENCE OF TRANSIENT HYPERFINE FIELDS FOLLOWING COULOMB EXCITATION

By

ALLAN WILLIAM MERSON GIBB, B.Sc.

A Thesis

Submitted to the Faculty of Graduate Studies

in Partial Fulfilment of the Requirements

for the Degree

Doctor of Philosophy

McMaster University

March 1973

DOCTOR OF PHILOSOPHY
(Physics)

McMASTER UNIVERSITY
Hamilton, Ontario.

TITLE: Velocity Dependence of Transient Hyperfine Fields Following Coulomb Excitation

AUTHOR: Allan William Merson Gibb, B.Sc. (University of Manitoba)

SUPERVISOR: Professor J. A. Cameron

NUMBER OF PAGES: xi ,189

SCOPE AND CONTENTS:

This thesis studies the velocity dependence of the transient magnetic field that is experienced by ions while slowing down in polarized ferromagnetic materials. Thick targets of $Fe_{80}Rh_{20}$, $Fe_{70}Pd_{30}$, and $Fe_{85}Pt_{15}$ alloys were bombarded by 5 to 10 Mev alpha particle, 35 Mev ^{16}O, and 20 Mev ^{12}C beams from the McMaster Tandem van de Graaff accelerator. The precession angles of Coulomb-excited rhodium, palladium and platinum nuclei that recoil and stop in the ferromagnetic target were measured using the technique of perturbed angular distributions following Coulomb excitation. The singles mode, in which gamma ray events are accepted irrespective of projectile scattering angle, was employed. A detailed theoretical analysis was developed to indicate how the double average over projectile scattering angle and energy required in a thick target singles experiment would modify the observed rotation angle. Calculations were carried out using the Coulomb excitation theory of Alder et al and the transient

field theory of Lindhard and Winther. The doubly-averaged transient field contribution to the rotation angle was found, in general, to be somewhat smaller than the transient field contribution before averaging, but the difference was not large for the cases of interest.

The data analysis permitted the separation of transient and average static rotations. The transient rotation as a function of initial recoil velocity was shown to be adequately described within experimental error by the Lindhard and Winther theory in both low and high velocity regimes. The average static field was seen to vary with the choice of projectile, but was not noticeably affected by changing the target coolant from water to liquid nitrogen.

Indirect feeding of a nuclear state, by Coulomb excitation of a higher-energy state and subsequent decay to the state of interest, was found to modify the observed precession angle of the state. The theory of this effect was developed for both singles and backscatter coincidence experiments; indirect feeding corrections were applied to the 295 kev state in ^{103}Rh and the 211 kev state in ^{195}Pt. The g-factor of the 211 kev state in ^{195}Pt was measured to be .164(66).

The g factors of the first 2+ states in ^{104}Pd, ^{108}Pd, and ^{110}Pd were measured from the average of 6, 7 and 8 Mev alpha particle bombardments of a $Fe_{70}Pd_{30}$ target. The analysis assumed that (1) the transient field rotation was negligible

at these bombarding energies and (2) the g factors of the 2+ states were not very different from the g factor of the first 2+ state in ^{106}Pd, which had been measured using a radioactive source. The results were $(^{104}Pd)g_{2+} = .479(91)$, $(^{108}Pd)g_{2+} = .396(46)$; $(^{110}Pd)g_{2+} = .389(36)$.

ACKNOWLEDGEMENTS

I would like to take this opportunity to acknowledge the contributions of other people to this work.

To my research supervisor, Dr. J. A. Cameron, thanks are due for his interest in, insight into, and assistance with the research project. His enthusiasm and sense of humour were very much appreciated.

To the other members of the supervisory committee, Dr. J.A. Kuehner and Dr. W. Smeltzer, I extend my thanks for their guidance and helpful suggestions; thanks are due also to Dr. R. G. Summers-Gill and Dr. R. Kelly, who agreed to act as stand-ins on very little advance notice.

To Dr. L. Keszthelyi and Dr. Z. Zamori, I express my thanks for their collaboration on the early experiments and their continued interest in this work. I acknowledge helpful discussions with Dr. J. A. Davies and Dr. R. Kelly on the subject of radiation damage.

To the PAC-rats, Stephen Barrett, Peter Kerr, Bev Kenyon, and Mike Byrnes, I express my thanks for their cooperation in setting up the experiments and baby-sitting the accelerator. Special thanks to Steve Barrett, who gave unselfishly of his time over many experiments, and to Bev Kenyon, who designed and built a logic box that worked well.

To the accelerator staff, master knob-twiddlers all, my appreciation for taming the accelerator beast. Special thanks to Mr. H. Blanchard for his help on electronics problems.

To Mrs. H. Kennelly, who typed the thesis, my thanks for being there when it counted most.

A special acknowledgement is due my wife, Adaire, who was able to put up with me while I was writing the thesis; my thanks for her tireless assistance with the drawings (where her professional touch is evident).

Finally, an acknowledgement to our new son, Brendan, who managed to arrive before the thesis did.

TABLE OF CONTENTS

LIST OF FIGURES

LIST OF TABLES

CHAPTER I

INTRODUCTION

Magnetic moment measurements for ground and excited states of nuclei are important because comparison of magnetic moments with theoretical predictions provides a test of nuclear models.

A wide variety of techniques has been developed for measuring magnetic moments of excited states of nuclei. All methods of measurement employ the fact that, in the presence of a magnetic field $\underline{H}$, the interaction of the moment $\underline{\mu}$ with the field $\underline{H}$ produces an interaction energy $\underline{\mu}\cdot\underline{H}$ and a torque on the nucleus $\underline{\tau} = \underline{\mu}\times\underline{H}$. $\underline{\mu}$ is related to the nuclear spin I by $\underline{\mu} = g\mu_N\underline{I}$ where μ_N is the nuclear magneton and the proportionality constant g is known as the nuclear g-factor. A technique such as recoilless resonance absorption (Mossbauer effect) measures the hyperfine interaction energy $\underline{\mu}\cdot\underline{H}$ directly. The method used in this thesis,perturbed angular distributions following Coulomb excitation (Chapter 2), makes use of the fact that when $\underline{H}$ has a fixed direction in space, the torque exerted on the nucleus causes the nucleus to precess with constant angular velocity ω (for constant H) about the direction of the field $\underline{H}$. The angular frequency ω is given by $\omega = -\frac{g\mu_N H}{\hbar}$ (independent of magnetic substate quantum number) where H is the

magnitude of the perturbing field, and μ_N and $\hbar$ are the nuclear magneton and Planck's constant/2π respectively.

The technique used in this thesis is a particular application of the general method of perturbed angular correlations. The usefulness of perturbed angular correlations is based on the fact that the precession of the nucleus while in the excited state causes a rotation of the angular distribution pattern of de-excitation gamma rays from that state. When this angular distribution pattern is anisotropic, the nuclear precession can be detected as a change in gamma ray count-rate at a particular angle. If, as in the experiments described herein, the detection method is only sensitive to rotation angles occurring during time intervals that are long compared to the mean life of the decaying excited state, then the observed time-averaged rotation angle is equal to $\omega\tau$ where τ is the mean life of the excited state.

Since $\omega\tau = -\frac{\mu_N}{\hbar}(gH\tau)$, a measurement of $\omega\tau$ constitutes a measurement of the product $gH\tau$. To extract the magnetic moment by measuring the nuclear g-factor, g, it is necessary to know the values of H and τ from independent measurements.

Mean lives can be measured in a variety of ways; the process used depends upon the order of magnitude of the mean-life. For the mean lives of 1-200 picoseconds considered in this thesis, the Doppler shift method and the "plunger" technique are useful. In addition, a measurement of the "upgoing" transition probability

in Coulomb excitation of a nuclear level provides a measurement of the E2 mean life of the level because the Coulomb excitation probability is directly related to the probability of decay of the level by an E2 transition. For a state which can decay only in E2 mode, this constitutes a measurement of the total mean life; for states which decay by an E2/M1 admixture, the total mean life can be deduced if the E2/M1 mixing ratio has been measured.

The perturbed angular correlation method was first described by Brady and Deutsch[B4] and was first successfully applied in 1951 by Aeppli et al.[A3] to the 247 kev 85 nanosecond state of ^{111}Cd. The applicability of the technique depends upon the mean life of the nuclear state. If the mean life is too long, then even in the absence of an external field, internal fields acting on the nuclei cause transitions between magnetic substates in such a manner as to make the substate populations more equal; this tends to destroy the anisotropy of the angular distribution.

For short mean lives, the converse problem presents itself; the value of the perturbing field H must be large enough to produce an observable rotation angle ($\omega\tau > 10^{-3}$ radians). External fields of tens of kilogauss can be used for states with nanosecond mean lives; however, many nuclear states have mean lives as short as 10^{-12} seconds. The required perturbing field (hundreds of kilogauss) far exceeded any external magnetic

field available in the laboratory in the mid 1950's.

The scope of the technique was extended upon the discovery of the large hyperfine field acting on dilute non-magnetic impurities imbedded in ferromagnetic iron (Grace (1955), - paramagnetic impurities; Samoilov (1959) - diamagnetic impurities.
While this field has a constant direction within a ferromagnetic domain, in an unmagnetized sample the domains are randomly oriented. Most of the domains can be aligned by placing the sample in an external field of a few kilogauss. By studying the nucleus of interest as a dilute impurity in magnetized iron, using the aligned internal hyperfine field as the perturbing field, rotation angles have been measured for states with mean lives as short as 2×10^{-12} seconds.

Hyperfine fields can be measured in a variety of ways. Nuclear magnetic resonance (NMR) and nuclear specific heat measurements require macroscopic amounts of material and are most useful for measurements on nuclear ground states whose magnetic moments have been measured in independent experiments. NMR measures the magnetic field on nuclei near or in the domain walls, while the remaining techniques sample the hyperfine field throughout the material. For measurements on excited states, Mossbauer effect and perturbed angular correlations must be used. In almost all cases for non-isomeric states, Mossbauer experiments require that the substate splittings be greater than the natural line widths and that the recoilless fraction be large enough to be useful; these requirements make the

Mossbauer effect generally applicable only to states with mean lives greater than 10^{-9} seconds and excitation energies less than 200 kev.

The first g-factor measurement using the internal hyperfine field in iron was performed by Metzger[M2] (1961) using the nuclear resonance fluorescence technique. Since 1963, many short-lived states have been investigated using the perturbed angular correlation technique on nuclei imbedded in various ferromagnets.

Several processes have been developed for imbedding the nuclei of interest in the ferromagnetic matrix of atoms. One process employed is the alloying by melting or diffusion of trace amounts of radioactive parent material into the ferromagnetic matrix. The parent nucleus then beta decays to the excited state of interest in the daughter nucleus. The beta decay imparts a recoil energy of $\lesssim 1$ kev to the daughter nucleus; this is sufficient to cause the nucleus to recoil through the lattice and to come to rest at a different location in a time less than 10^{-12} seconds. A related process is ion implantation, in which radioactive parent atoms are implanted at a controlled energy (usually ten to several hundred kev) into an initially pure ferromagnetic material. In this process, most of the interesting atoms find themselves relatively close to the surface of the ferromagnetic lattice; the depth distribution can be varied by altering the incident ion energy. The

need for a source of radioactive parent atoms can be removed if one uses an on-line process such as Coulomb excitation or a nuclear reaction to excite the nuclear level of interest. These processes involve collisions between target atoms and a beam of ions of Mev energy from a particle accelerator. The initial recoil energies of the target atoms can be as large as 20 Mev or more. These recoiling atoms stop in a time of $< 10^{-12}$ seconds, and impart all of their kinetic energy to the lattice during this stopping time.

For all of the processes described, the fact that the ions undergo predominantly nuclear collisions when their energy has degraded to 250 kev or so means that they will be very effective in displacing lattice atoms (radiation damage) in this energy region. This dynamic interaction between lattice and recoiling atom forces the experimenter to proceed with caution when considering the final site of the recoiling atom, and the final hyperfine environment that it sees.

A relative of the method employed in this thesis is the ion implantation perturbed angular correlation technique (IMPACT). The method employs Coulomb excitation to excite the nuclei of interest and detects the de-excitation gamma-ray in coincidence with the projectile that caused the excitation. By detecting the scattered particles at angles close to 180°, one chooses to look only at gamma rays which have very anisotro-

pic angular distributions; this makes the angular distribution very sensitive to small rotations, but the method is limited by the fact that the Coulomb excitation cross-section must be high enough to produce a reasonable coincidence count rate, a fact which dictates the use of heavy ion beams (e.g. ^{16}O ions) in most cases. The targets in IMPACT experiments consist of a thin layer of target material coated on the front surface of a ferromagnetic magnetized foil (usually iron). Coulomb excitation of the interesting nuclei occurs in the surface layer, and detection of the backscattered projectiles ensures that the excited atoms recoil into the ferromagnetic backing in a narrow forward cone. The use of heavy ions with tens of Mev of energy as projectiles (e.g. 35 Mev ^{16}O) means that the recoiling Coulomb-excited atoms can have large energies (eg 20 Mev) and correspondingly large recoil velocities. This is to be compared with typical recoil energies of 100 kev for the ion implantation process, 1 keV for the beta decay process, and 0 kev for the Mossbauer effect.

Measurements of g-factors using the IMPACT technique yielded several negative g-factors for short-lived 2^+ states in even-even nuclei. Since these results disagreed with all previous g-factor measurements on such states using beta decay and ion implantation, a systematic study of the Coulomb excitation results was undertaken. Taken collectively, the data seemed to indicate the existence of an impulsive rotation imparted to the nucleus in a time $\lesssim$ 1 picosecond and comparable in magnitude

to the rotation angles measured for short-lived states using beta decay and ion implantation. Followup experiments confirmed that the impulsive rotation was associated with the slowing down of the ion in the ferromagnetic backing[H3]. The apparent absence of such an impulsive rotation for experiments employing beta decay and ion implantation seems to indicate that the interaction is negligible at low recoil velocity. Since an electric quadrupole interaction cannot produce a rotation of the angular distribution pattern, the rotation has been ascribed to the existence of a large transient magnetic perturbation of the same sign as the external magnetizing field. Lindhard and Winther[L1] have developed a theory which accounts for this transient field as a function of recoil velocity in terms of an enhancement of the conduction electron spin density at the nucleus of the moving ion. If v is the relative velocity of ion and electron, their theory predicts a $\frac{1}{v}$ dependence of the field down to a velocity v_p and a constant non-zero value for the field below v_p.

An understanding of the transient magnetic field acting on a Coulomb-excited nucleus is important because it could permit the nuclear g-factor to be measured for very short-lived states ($\lesssim$ 1 psec) without requiring a precise knowledge of either the internal field seen after the ion comes to rest or the mean-life of the state. An understanding of the transient field behaviour for low recoil velocities is especially important because the ion spends most of its stopping time at low velocities

where the field is largest.

One obvious way to study the velocity dependence of the transient field is to vary the initial recoil velocity by changing the incident beam energy. The beta decay results correspond essentially to zero initial recoil velocity. The IMPACT technique is not suitable for scanning the whole velocity range because 1) using heavy ions as projectiles, the Coulomb excitation probability becomes prohibitively low while the incident ion still has an appreciable energy, and 2) using light projectiles, the signal-to-noise ratio is poorer because the background is relatively higher in both particle and gamma ray windows.

The singles technique employed in the present work uses light projectiles (^{4}He) to achieve low recoil velocities; the method removes the coincidence condition and accepts gamma rays irrespective of the angle at which the projectile is scattered This has the effect of attenuating the angular distribution coefficients by a factor of 10 or more. The loss in sensitivity due to averaging over scattering angle and the smaller Coulomb excitation probability associated with the use of light projectiles can be more than compensated by the use of alloy targets in which the target material is alloyed with iron in concentrations of from 5 up to 50 atom percent. In this kind of experiment, since the recoil velocity of the target atom is uniquely related to the angle of scatter of the incident projectile, the

acceptance of all scattering angles implies that the interesting target atoms will have a range of initial recoil velocities. It is not obvious that a single recoil velocity adequately characterizes the velocity distribution in this case; consideration of this point is important if it is desired to study the transient field as a function of recoil velocity. This thesis studies the singles technique in detail and demonstrates that, given a model for the transient field, it can be used in conjunction with a light projectile (^{4}He) to investigate the expected velocity dependence of the transient field at low recoil velocities. Conclusions about this low-velocity dependence are drawn on the basis of a comparison between the experimental data and the theoretical predictions.

Chapter 1 has presented a brief introduction to the transient field phenomenon in order to place the present work in historical perspective. The second chapter presents short summaries of relevant areas of physics theory; this section will prove useful to readers not thoroughly familiar with the use of perturbed angular distributions following Coulomb excitation in transient field studies. In chapter three, Lindhard and Winther's theory of the transient field is combined with a careful analysis of the singles perturbed angular distribution technique to predict how the transient field will modify the observed rotation angle. A method for studying the low-velocity dependence of the transient field as a function of incident projectile

energy is developed. Chapter four is an unexciting but necessary description of the hardware used to perform the experiments. In chapter five, various aspects of the data analysis are discussed and the results are presented, chiefly in the form of graphs and tables. These results are analyzed and compared with the results of other workers in chapter six. Finally, chapter seven summarizes the conclusions that can be drawn from the present work; a discussion of the significance of these conclusions completes the thesis.

CHAPTER II

THEORY

The purpose of this chapter is to provide a very brief theoretical discussion of those aspects of physics theory which relate to the subject of this thesis. No attempt at completeness has been made. Each discussion is heavily weighted in favour of those points of the theory which will find application elsewhere in the thesis.

A. COULOMB EXCITATION

This development is based upon the excellent review article of reference Al.

By Coulomb excitation is meant the excitation of a nuclear excited state through the interaction of the charged nucleus with the electromagnetic field of a charged nuclear projectile. Because the interaction potential is well-known, namely the simple Coulomb potential, an extensive and detailed theoretical analysis of the Coulomb excitation process is possible[Al], and calculations based on this analysis permit the outcome of many Coulomb excitation experiments to be predicted with considerable quantitative accuracy.

The motion of the projectile in the Coulomb field of the nucleus is essentially characterized by the dimensionless quantity η defined by $\eta = \frac{Z_P Z_T e^2}{\hbar v}$ where Z_P and Z_T are atomic

numbers of projectile and target, e = electronic charge, $\hbar$ = Planck's constant, v = relative velocity of projectile and target nuclei. η measures the effective strength of the interaction. For $\eta << 1$, the Coulomb field produces only a small distortion of the incident wave and the collision process can be treated by the Born approximation in which the incident particle is treated as a plane wave. However, if the repulsive interaction is not sufficiently strong, the nuclei can come close enough together for nuclear reactions to occur. The condition that the interaction be strong enough to obviate consideration of competing nuclear reactions imposes the requirement that $\eta >> 1$; in this case the particle is sufficiently well-localized that the collision may be approximately described by considering the incident particle to move along a classical trajectory for the duration of the interaction. For inelastic collisions, it is a further condition that the energy loss of the projectile be small compared to the bombarding energy, E, so that the effect of the excitation on the projectile's classical motion can be neglected.

Under these assumptions, the nuclear excitation can be treated in terms of the time-dependent electromagnetic field of the projectile acting on the nucleus. The excitation probability can be expressed in terms of the same nuclear matrix elements that determine radiative transitions between nuclear states. The Coulomb excitation process is related to the

nuclear properties of the excited states through these matrix elements.

In many cases, a semi-classical treatment of Coulomb excitation is adequate; a detailed quantum mechanical treatment introduces, in most instances, only small corrections. One begins by noting that, in view of the assumption that the orbit of the particle is negligibly affected by the excitation, the differential Coulomb excitation cross-section can be written as a product of two factors

$$d\sigma_{exc} = P d\sigma_R ,$$

where $d\sigma_R$ is the classical Rutherford scattering cross-section, and P is the probability that the nucleus is excited in a collision in which the particle is scattered into solid angle $d\Omega$. P can be expressed in terms of the amplitudes, b_{if}, for transition from an initial nuclear state i to various final states f. Because it is usually the case that the probability for excitation in a single encounter is very small, first order time-dependent perturbation theory can be used to provide an expression for the excitation amplitudes b_{if}.

$$b_{if} = \frac{1}{i\hbar} \int_{-\infty}^{\infty} \langle f|H(t)|i\rangle e^{i\omega t}\, dt$$

where $\omega = \frac{\Delta E}{\hbar} = \frac{E_f - E_i}{\hbar}$ is the nuclear frequency associated with excitation energy ΔE, and $H(t)$ is the interaction Hamiltonian; for non-relativistic velocities, the main interaction is the

Coulomb energy. To evaluate the matrix element $\langle f|H(t)|i\rangle$, it is convenient to expand the Coulomb potential in terms of multipole components. One obtains

$$b_{if} = \frac{4\pi Z_p e}{i\hbar} \sum_{\lambda,\mu} \frac{1}{2\lambda+1} \langle I_i M_i | M(E\lambda,\mu) | I_f M_f \rangle S_{E\lambda,\mu}(\xi)$$

where I and M denote the total angular momentum quantum number and magnetic quantum number respectively of the initial (i) and final (f) states and $M(E\lambda,\mu)$ is the electric multipole moment of order λ. One point worth noting is the fact that the matrix elements are functions of purely nuclear parameters; all of the information about the role of the Coulomb interaction is contained in the integral over orbital parameters, $S_{E\lambda,\mu}(\xi)$. The quantity ξ is proportional to the ratio between the collision time and the nuclear period and so provides a measure of the adiabaticity of the Coulomb excitation process. The more sudden the impact (i.e. smaller collision time and so smaller ξ value), the greater is the probability for Coulomb excitation in a single collision. Thus as ξ decreases, the Coulomb excitation probability increases. The dimensionless parameter ξ is defined by

$$\xi = \frac{a\Delta E}{\hbar v} = \frac{Z_p Z_T e^2 \Delta E}{\hbar v \quad 2E}$$

where ΔE = excitation energy, E = bombarding energy, a = distance of closest approach in a head-on collision, Z_p and Z_T are atomic numbers of projectile and target, and v is their relative velocity.

Because the multipole moments are spherical tensor operators, the Wigner-Eckart theorem permits each matrix element to be written as the product of two factors; the first, a Clebsch-Gordon coefficient, is a geometrical factor sensitive to the orientation of the nucleus through its dependence on the magnetic quantum numbers M_i and M_f; the second is a factor called the reduced matrix element $\langle I_i||M(\lambda)||I_f\rangle$ which is independent of nuclear orientation and depends only upon the nuclear properties of the states involved. As corollaries of the Wigner-Eckart theorem, one may impose the usual spectroscopic selection rules:

$$|I_i - I_f| \leq \lambda \leq I_i + I_f$$

$$\pi_i\pi_f = \begin{cases} (-1)^{\lambda} & \text{for electric transitions of order } \lambda \\ (-1)^{\lambda+1} & \text{for magnetic transitions of order } \lambda \end{cases}$$

where I_i and I_f are the total angular momentum quantum numbers (commonly referred to as "spins") of the initial and final nuclear states and π is the parity of these states.

It is convenient to introduce a quantity called the "reduced transition probability", $B(E\lambda)$; it is the probability, irrespective of nuclear orientation in the initial and final state, for a <u>radiative</u> transition, from an initial state I_i to a final state I_f, of pure electric multipole order $E\lambda$.

$$B(E\lambda, I_i \rightarrow I_f) = \frac{1}{2I_i+1} |\langle I_i||M(E\lambda)||I_f\rangle|^2.$$

Employing orthogonality relations among the Clebsch-Gordon coefficients, the differential excitation cross-section can be written $d\sigma_E = \sum_{\lambda=1}^{\infty} d\sigma_{E\lambda}$ where each $d\sigma_{E\lambda}$ is proportional to the corresponding $B(E\lambda)$. The total cross-section for excitation of order $E\lambda$ is obtained by integrating the corresponding differential cross-section over all the possible scattering directions for the projectile. It is given by

$$\sigma_{E\lambda} = \left(\frac{Z_p e}{\hbar v}\right)^2 a^{2-2\lambda} B(E\lambda) f_{E\lambda}(\xi) \ .$$

The total cross-section for excitation of order $E\lambda$ is seen to be proportional to $B(E\lambda)$. The function $f_{E\lambda}(\xi)$ is known as the excitation function; it contains all the information about the effect of the Coulomb interaction whereas $B(E\lambda)$ depends only upon the nuclear parameters of the states involved. The corresponding differential excitation function $df_{E\lambda}(\xi,\theta_p)$ depends not only upon ξ but also upon the angle θ_p through which the projectile is scattered. Both of these functions have been evaluated in the classical limit and the values tabulated[Al]; a computer program[Wl] is available which will calculate these functions using the full quantum mechanical theory.

The above analysis has been applied to electric excitations for which $\pi_i \pi_f = (-1)^{\lambda}$. The opposite parity can be produced through interaction with the magnetic field of the projectile. However, a similar analysis using a magnetic vector potential yields an expression for $\sigma_{M\lambda}$ which is smaller

than $\sigma_{E\lambda}$ by a factor $(\frac{v}{c})^2$. For bombarding energies below the Coulomb barrier, $v << c$, so the magnetic excitation cross-sections are usually negligible with respect to electric excitations of corresponding multipole order.

The electromagnetic fields acting on the nucleus in a radiative transition and in a Coulomb excitation event are different. This implies possible differences in the relative contributions of successive multipole components for the two processes. For a given multipole order, in a radiative process the electric and magnetic field strengths are roughly equal in magnitude; in Coulomb excitation, the electric component dominates, as discussed above. In addition, the cross-section for Coulomb excitation does not decrease as rapidly with increasing multipole order as does the intensity of corresponding radiative processes.

Transition probabilities are usually expressed in terms of the probabilities calculated from a single-particle model of the nucleus - the so-called "single-particle unit". Experimentally, the probabilities obtained from measurement of the lifetimes of gamma ray transitions show marked departures from the single-particle unit; electric dipole (E1) transitions have transition probabilities orders of magnitude smaller than the single particle unit, whereas electric quadrupole (E2) transitions are enhanced by factors of 10-100. This enhancement of E2 transitions can be explained provided one assumes

that the ground and excited states have a collective nature - ie. that the nucleons are behaving in a co-operative manner so that a simple wave function with a small number of degrees of freedom may be found which describes the nucleus as a whole. The usual collective excitations consider the (non-spherical) nucleus as a rotor or the (near-spherical) nucleus as a spherical object having surface vibrational waves. The important point is that the collective wavefunction in each case contains a component that is the spherical harmonic $Y_{20}(\theta,\phi)$. This is the same function that describes the spatial distribution of the quadrupole moment operator (whose intensity pattern is that of a classical quadrupole antenna). When the component Y_{20} is present in the initial and final states, the two states are strongly connected by the quadrupole moment operator. This is the basis for the statement that E2 transitions are strongly enhanced between states that are collective in nature. In particular, Coulomb excitation in nuclei whose ground and excited state are collective in nature occurs overwhelmingly by an E2 transition. Because of the enhanced E2 transition probabilities for these collective states, Coulomb excitation is a useful tool for studying these states. It is usual to consider the transition to be pure E2; of course, for a 0+ → 2+ transition, the transition must be pure E2.

In summary, Coulomb excitation provides a useful tool for populating low-lying collective states with picosecond lifetimes that are accessible by E2 transitions. Because the

force law is the simple Coulomb force law, the theory of Coulomb excitation can be worked out in full quantum-mechanical detail; as a result, the effect of Coulomb excitation in various experiments can be calculated with considerable quantitative accuracy. Often a semi-classical calculation is adequate; the parameter η is a measure of the extent to which a collision between a given target and projectile of specified incident energy can be described in a classical way. As η increases, the collision looks more classical. The parameter ξ is a measure of the suddenness of the collision; as ξ decreases the collision becomes more sudden in nature and the Coulomb excitation probability increases, all else being equal.

B. ANGULAR DISTRIBUTIONS OF DE-EXCITATION GAMMA RAYS FOLLOWING COULOMB EXCITATION

The nuclear states populated in Coulomb excitation decay by emission of gamma-radiation or internal conversion electrons. The angular-distribution of this radiation can be obtained from the excitation amplitudes b_{if} discussed above.

If the Coulomb excitation process populated all of the magnetic substates of a given excited state equally, the ensemble of nuclei would have no preferred orientation and the angular distribution of de-excitation gamma rays from that state, with the incident beam direction as quantization axis, would be necessarily isotropic. An anisotropic distribution is observed because the Coulomb excitation process does not populate the substates with equal strength; it does however

populate them symmetrically with respect to sign (i.e. $P(+m) = P(-m)$ but $P(m) \neq P(m')$ for $m \neq m'$). In this case, the ensemble of Coulomb excited nuclei is said to have a preferred orientation. In Coulomb excitation experiments, the direction of the incident particle beam defines a preferred direction in space with respect to which angles are measured and angular momentum projection quantum numbers are expressed. If the incident ion beam is unpolarized the angular distribution has azimuthal symmetry about the beam axis. Considering that the beam axis and the axis of the gamma ray detector intersect at the point where the beam strikes the target, one defines the plane containing these axes as the plane of detection, and the angle between them is angle θ (+'ve z direction defined by direction of travel of ions).

For an angular distribution, the quantity of interest is the probability for emission of a gamma ray at an angle θ, without regard to polarization, for a process involving Coulomb excitation from a state with spin I_i to a state with spin I_f and subsequent de-excitation from state I_f to a final state with spin I_{ff}. The extent to which this probability varies as a function of angle θ depends upon how unevenly the substates of the excited state are populated in the Coulomb excitation process; one expects therefore that the probability will involve a <u>coherent</u> sum over magnetic substates m_f of this state. Since the detection process is sensitive neither to the

polarization of the emitted gamma ray nor to the magnetic substates, m_i and m_{ff}, of initial and final states, one similarly anticipates that the probability will involve incoherent sums over these quantum numbers. The appropriate expression is

$$W(\theta) = \sum_{\sigma,\, m_i\, m_{ff}} \left| \sum_{mf} b_{if} \langle I_{ff} m_{ff} | H_\gamma(\theta,\sigma) | I_f m_f \rangle \right|^2 \qquad (2\text{-}1)$$

where $H_\gamma(\theta,\sigma)$ is the interaction Hamiltonian causing emission of a gamma quantum in the direction θ and with polarization σ.

~~and (θ) is the co-ordinate of the scattered projectile.~~

The simplest case to consider (and most important experimentally) is one in which the excitation is of pure multipole order λ. It is very helpful to consider the angular distribution in terms of an angular correlation function for a hypothetical gamma-gamma cascade. The theory of gamma-gamma angular correlations is well-developed; in such a correlation, the detection of the first gamma-ray selects a non-random distribution of magnetic substates of the intermediate state and the angle of emission of the second gamma ray is measured with respect to the direction of emission of the first gamma-ray. The gamma-ray distribution (2-1) is one which would apply if the gamma-ray were detected in coincidence with the scattered projectile: a gamma-particle angular correlation. The theory of angular correlations demonstrates that expression (2-1) can be written as a sum of even-order Legendre polynomials. Usually, only the first three terms are sufficient to describe the cor-

relation,and the correlation is conventionally normalized to unity.

$$W(\theta_\gamma,\theta_p,\xi) = 1 + a_2^\lambda(\theta_p,\xi)A_2^\lambda P_2(\cos\theta_\gamma) + a_4^\lambda(\theta_p,\xi)A_4^\lambda P_4(\cos\theta_\gamma)$$

where θ_γ and θ_p are the angles at which the gamma ray is emitted and the incident particle scattered respectively relative to the beam axis. The factors A_2^λ and A_4^λ are numbers which depend only upon the spins and parities of the ground and excited states as well as upon the multipolarities associated with the excitation and de-excitation processes. These are the same factors which describe the angular distribution for the equivalent gamma-gamma cascade. The entire influence of the Coulomb excitation process on the angular distribution is contained in the so-called "particle parameters" a_2^λ and a_4^λ. These numerical factors are functions of the angle θ_p at which the incident projectile is scattered as well as of the Coulomb excitation parameter ξ. The behaviour of a_2 and a_4 as a function of θ_p and ξ is illustrated in Fig. 2-1.

From this figure, it can be seen that if only Coulomb excitation events caused by projectiles backscattered at 180° are observed, the value of a_2 is 2, and the value of a_4 is -1.5, so the anisotropy of the angular distribution is greatly enhanced. An experimental arrangement which closely approximates these conditions is one in which the gamma-rays are detected in coincidence with the backscattered projectile; the particle detector is an annular detector concentric with the beam axis and subtending an angular spread typically of 160° to 170°.

Figure 2-1

Comparison of (1) semi-classical and (2) full quantum-mechanical calculations of thin target particle parameters a_2^{E2} and a_4^{E2}. Semi-classical calculations used orbital integrals of reference A1; quantum-mechanical calculations were generated from deBoer-Winther computer code. Results are plotted as a function of projectile scattering angle for two representative values of the ξ parameter.

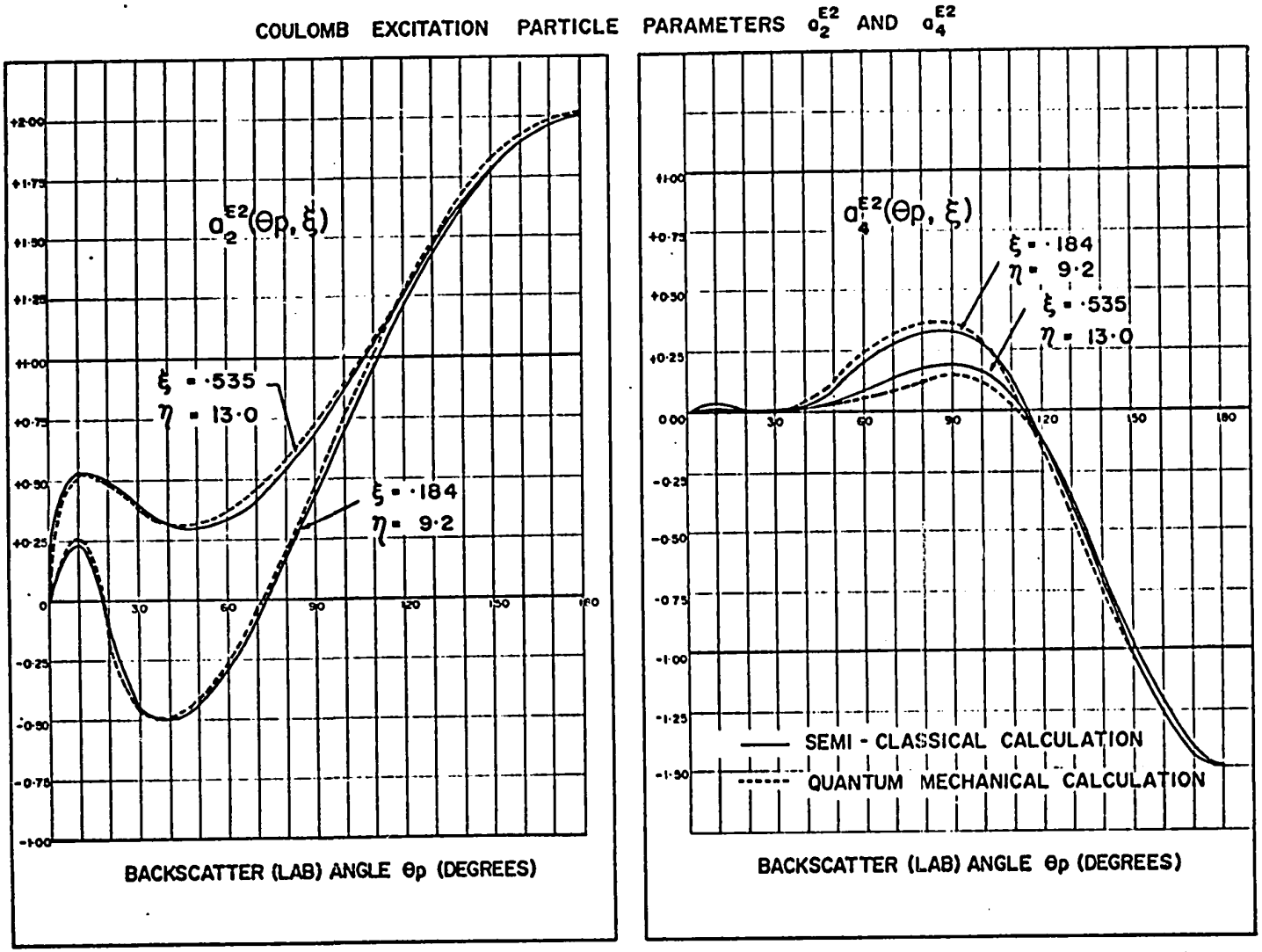
COULOMB EXCITATION PARTICLE PARAMETERS a_2^{E2} AND a_4^{E2}
$a_2^{E2}(\theta p, \xi)$
$\xi = \cdot 535$
$\eta = 13 \cdot 0$
$\xi = \cdot 184$
$\eta = 9 \cdot 2$
BACKSCATTER (LAB) ANGLE θp (DEGREES)
$a_4^{E2}(\theta p, \xi)$
$\xi = \cdot 184$
$\eta = 9 \cdot 2$
$\xi = \cdot 535$
$\eta = 13 \cdot 0$
SEMI - CLASSICAL CALCULATION
QUANTUM MECHANICAL CALCULATION
BACKSCATTER (LAB) ANGLE θp (DEGREES)

Figure 2-1

This geometry will produce values of a_2 and a_4 close to the values appropriate to 180°. However, the advantage of large anisotropy is offset to some extent by the low counting rate associated with coincidence experiments. An alternative approach is to detect the gamma-rays without regard to the angle at which the projectile is backscattered. In this case, what is observed is an angular distribution averaged over backscatter angle i.e.

$$\bar{W}(\theta_\gamma,\xi) = \int_0^\pi W(\theta_\gamma,\theta_p,\xi)P(\theta_p)d\theta_p$$

where $P(\theta_p)$ is the differential Coulomb excitation probability for an event in which the projectile is backscattered at angle θ_p. The effect of this averaging process is to attenuate the particle parameters a_2 and a_4 by as much as a factor of 10 relative to the values appropriate for the coincidence experiment described above. These parameters are then functions only of the variable ξ. Strictly speaking, a_2 and a_4 are also functions of the variable η, but in the calculations described in chapter 3 they are calculated in the classical limit ($\eta = \infty$), so the η-dependence has been omitted.

C. PERTURBED ANGULAR DISTRIBUTIONS FOLLOWING COULOMB EXCITATION

(i) Magnetic Perturbations

If the Coulomb-excited nuclei experience an applied magnetic field while in the excited state, their magnetic moments will execute Larmor precession about the field direction.

Since this alters the nuclear orientation, it changes the relative population of magnetic substates and so modifies the angular distribution of de-excitation gamma rays. Detection of a gamma-ray, which must have an angular momentum component of ±1 in its direction of travel, selects a particular ensemble of Coulomb excited nuclei all of whose members have an angular momentum projection in the direction perpendicular to the plane of detection. If a static magnetic field is applied perpendicular to this plane, the above ensemble precesses about the field direction, but the nuclei do not change their angular momentum projection along the field direction. One would expect in this case that the entire gamma ray angular distribution would simply rotate through an angle ωt where ω is the Larmor precession frequency and t is the time for which the magnetic field acts; a detailed analysis indicates that this is in fact the case. Thus, if

$$W(\theta) = \sum_k a_k A_k P_k(\cos\theta) \quad \text{where } k = 0,2,4$$

then

$$W(H,\theta,t) = \sum_k a_k A_k P_k[\cos(\theta-\omega t)] \ .$$

This series can be written in an equivalent form

$$W(\theta,H,t) = \sum_k b_k \cos[k(\theta-\omega t)]$$

where

$$b_0 = 1 + \frac{1}{4} a_2A_2 + \frac{9}{64} a_4A_4 \quad b_2 = \frac{3}{4} a_2A_2 + \frac{5}{16} a_4A_4 \text{ and } b_4 = \frac{35}{64} a_4A_4.$$

If the gamma rays are not observed in coincidence with the scattered projectile, the distribution is not sensitive to the time t from excitation to de-excitation of the nuclear state. In that case, what is observed is a distribution averaged over all times t, with the distribution weighted by the exponential decay factor of the state. The observed perturbed angular distribution is given by

$$W(\theta,\infty) = \frac{1}{\tau}\int_0^\infty W(\theta,t)\exp(-t/\tau)dt$$

$$= \sum_k \frac{b_k \cos[k(\theta-\Delta\theta)]}{((1+(k\omega\tau)^2)^{1/2}} \qquad \text{where } k = 0,2,4$$

and $k\Delta\theta = \arctan(k\omega\tau)$, τ being the mean life of the state. For small $\omega\tau$, $\Delta\theta \approx \omega\tau$.

It is to be noted that, in addition to the so-called "integral rotation" $\Delta\theta$, the averaging process has introduced an attenuation factor $1/((1+(k\omega\tau)^2)^{1/2}$. For short mean lives, this factor is effectively unity; for longer mean lives, and large perturbing fields, the attenuation can be significant, especially if the angular distribution coefficients b_2 and b_4 are small. The largest rotation angle dealt with in this thesis is $\sim$ .12 rad; for which $(2\omega\tau)^2 = .058$ and $(4\omega\tau)^2 = .23$. If the attenuation factors are ignored, they can introduce errors of up to 5.8 and 23% into the b_2 and b_4 terms respectively. In most cases, however, the error incurred by ignoring these factors is negligible (i.e. $\lesssim$ 1%).

The Larmor precession frequency is given by

$\omega = -\frac{g\mu_N H}{\hbar}$ where μ_N is the nuclear magneton, H is the magnitude of the perturbing magnetic field, and g is the nuclear g factor. If the integral rotation angle $\Delta\theta$ is equal to $\omega\tau$, measurement of $\omega\tau$ by observing the rotation of the angular distribution pattern caused by the magnetic perturbation H permits determination of the product $gH\tau$. If any two of these quantities have been measured in independent experiments, the third can be determined from an integral rotation measurement. A popular use of the integral rotation method is for the measurement of g factors on a nuclear state whose mean-life is known in an environment where the value of H is known.

(ii) Electric Perturbations

Thus far, the discussion has dealt only with the effect of a static magnetic perturbation. However, an asymmetric charge distribution about a lattice site can produce an electric field gradient at that site. If the nucleus possesses an electric quadrupole moment, it can interact with the electric field gradient. For an axially symmetric electric field gradient $(\frac{\partial E}{\partial Z})$, the electric quadrupole interaction energy is given by

$$\Delta E = \frac{3m^2 - I(I+1)}{4I(2I-1)} \; eQ(\frac{\partial E}{\partial Z})$$

where I is the nuclear level spin, m is the substate's magnetic quantum number, and Z is the direction of the electric field's symmetry axis.

The degeneracy of the interaction energy in +m and -m implies that the interaction cannot distinguish "up" from "down".

This fact, coupled with the fact that substates with magnetic quantum number +m and -m are equally populated, means that the electric quadrupole perturbation produces no net rotation of the angular distribution pattern. The perturbation does, however, produce an attenuation of the angular distribution coefficients. The perturbed distribution can be written as

$$1 + G_2(t)A_2P_2(\cos\theta) + G_4(t)A_4P_4(\cos\theta)$$

where the factors $G_2(t)$ and $G_4(t)$ are < 1 and account for the quadrupole attenuation.

It is convenient to introduce the quadrupole frequency

$$\omega_Q \equiv \frac{-eQ}{4I(2I-1)\hbar}\frac{\partial E_Z}{\partial Z} \quad . \tag{2-2}$$

The quadrupole attenuation coefficients can be expressed in terms of the frequency ω_o, which is the smallest non-vanishing energy difference between substates and is given by

$$\omega_o = 3\omega_Q \text{ for } 2I \text{ even.}$$
$$= 6\omega_Q \text{ for } 2I \text{ odd.}$$

The time integral attenuation coefficients for a quadrupole interaction involving a 2+ state (I=2) are:

$$G_2 = 0.3714 + \frac{0.0572}{1+(\omega_o\tau)^2} + \frac{0.3428}{1+(3\omega_o\tau)^2} + \frac{0.2285}{1+(4\omega_o\tau)^2}$$

$$G_4 = 0.4603 + \frac{0.1905}{1+(\omega_o\tau)^2} + \frac{.254}{1+(3\omega_o\tau)^2} + \frac{0.0952}{1+(4\omega_o\tau)^2}$$

where τ is the meanlife of the 2+ state.

The size of the quadrupole frequency for a 2+ state

can be estimated from eq. (2-2). If one assumes an electric field gradient of $10^{18} V/cm^2$ (abnormally large), a quadrupole moment Q of 1 barn, and a mean life τ of 100 psec, one obtains $\omega_o \tau \approx .019$ rad. Since $(4\omega_o \tau)^2 = .058$, only a few percent error at most will be incurred by assuming the quadrupole attenuation factors to equal 1. For the experiments in this thesis, any quadrupole field gradients present are almost certainly less than the value used in this example, and all of the mean lives are < 100 psec, so the quadrupole attenuation can be safely ignored.

For an ion recoiling in a metal, there can be another source of electric field gradient. As indicated in the theory of the transient field (Sec. 2-D) by virtue of its motion a recoiling ion's nucleus will see an enhancement of the conduction electron spin density at the site of the nucleus. The fact that the electron density is not uniform means that there can also be an electric field gradient at the nuclear site with symmetry axis in the direction of the ion's motion.

Lindhard and Winther calculate the electric quadrupole interaction due to the ion's motion, and find that the interaction energy with the ion nucleus is, apart from an additive constant,

$$\Delta H = \frac{1}{4} \bar{Y} eQ P_2(\cos\theta) \qquad (2\text{-}3)$$

where Q is the nuclear quadrupole moment and θ is the angle between the nuclear spin and direction of motion.

The function $\bar{Y}$ is given by

$$\bar{Y} = -e \frac{8\pi^2 V_o}{3v} Z_p Z_T N F(v, Z_T)$$

where N is the atom density of the target material,

$V_o = \frac{c}{137}$

and the function $F \sim Z_T^{-2/3} (\frac{V}{V_o})$ for moderate velocities $V > V_o$.

It is noted that, in the moderate velocity region, the quadrupole frequency $\frac{\Delta H}{\hbar}$ is roughly independent of velocity

$$\omega = \frac{1}{4} \frac{8\pi^2}{3} \frac{e^2 Q Z_p Z_T^{1/3} N P_2(\cos\theta)}{\hbar}$$

Evaluation of this frequency for Rh recoiling in Fe gives

$$\omega = 1.62 \times 10^{10} \text{ radians/sec} \qquad (2\text{-}4)$$

where $P_2(\cos\theta)$ is assumed = 1. Lindhard and Winther's theory also indicates that the quadrupole interaction should turn off for $V < V_o = \frac{c}{137}$.

For a backscatter coincidence experiment, the direction of motion of the recoiling ion is almost along the quantization axis (beam direction), so the axis of the electric field gradient is effectively parallel to the quantization axis; for this case, there will be no quadrupolar attenuation of the angular distribution coefficients[S1]. For a singles experiment, the recoiling ions make a range of angles with the quantization axis, varying from 0° up to the angle which corresponds to recoil velocity V_o, at which the transient quadrupole interaction is supposed to turn off. The problem of treating the effect of a randomly oriented or single crystal quadrupole interaction in the presence of a simultaneous magnetic perturbation has been treated by Alder et al.[A2] The attenuation factors for a singles experi-

ment can be expected to lie somewhere between 1 (180° backscatter only) and the values appropriate to a constant, but randomly-oriented, quadrupole interaction. The attenuation factors for the particular cases considered in this thesis would have to be calculated by lengthy numerical methods.

However, the general expression for the attenuation coefficients[S1] can be written in the form

$$G_{kk}^{N_1 N_2}(t) = \sum_{n,n'} C_{nn'} e^{-\frac{i}{\hbar}(E_n - E_{n'})t}$$

where n and n' run over the number of substates of the excited state and where the constants $C_{nn'}$ are independent of time. When the attenuation coefficients are averaged over all times from $0 \to \infty$, noting that the quadrupole effect turns off after time t_o, one finds that the time-dependent exponential terms look like $1-C(\omega t_o)^2$ to second order in ωt_o where the constant $C \sim \frac{t_o}{\tau}$. For a 2+ state, the largest possible frequency is twice the frequency (2-4) i.e. $\omega = 3.24 \times 10^{10}$. Assuming $t_o = 1$ psec, one finds $(\omega t_o)^2 \sim 10^{-3}$, so the attenuation from the transient quadrupole interaction is negligible.

D. TRANSIENT FIELDS

By transient field is meant the amplification of the magnetic field which acts on an ion moving through an aligned ferromagnetic material. The theory of this effect, developed by Lindhard and Winther[L1], is based upon the general theory of stopping of heavy ions in solids. Except at very low velocities, the predominent mechanism is electronic stopping in which elec-

trons are excited or ejected from atoms along the path of the particle. These electronic collisions produce a continuous and slow decrease in the ion's velocity; at low energies the stopping power is proportional to the velocity of the ion.

To describe the stopping, one uses the picture of a charge moving in a degenerate electron gas. With co-ordinate system attached to the moving ion, the picture is one of an almost stationary flow of electrons scattered in the field surrounding the ion; each electron sees the field produced partly by the nuclear charge and partly by the other electrons which are scattered or held in strongly-bound states. (For low velocities, this self-consistent field is close to a Hartree-Fock field).

It is well-known that, in scattering at low velocities in a Coulomb field of charge $Z_p e$, the density of electrons at the centre is enhanced by a factor $\chi = \frac{2\pi Z_p e^2}{\hbar V_r}$ over the density at infinite distance, where the velocity of the electrons is assumed to be V_r. It is an important assumption of the theory that the spin density at the nucleus suffers the same enhancement.

One now considers a ferromagnetic material with N atoms/cm^3 and assumes that ζ electrons per atom are polarized in the direction of magnetization $\underline{\mu}$. The magnetic moment of the ion's nucleus will precess in a magnetic field which, in the rest system of the ion, is given by $\underline{B} = \frac{8\pi}{3} \rho \underline{\mu}(1+\xi)$ where ρ is the polarized electron density at the nucleus and $|\underline{\mu}|$ is the Bohr magneton. The factor $(1+\underline{\xi})$ takes into account the fact that $\underline{B}$

is in the direction of magnetization only if the density distribution is spherically symmetric ($\xi = 0$) in the ion's rest frame. For finite electron velocity V_r there is an asymmetry due to the preferred direction of the ion's motion through the solid; this gives rise to an additional term of the form

$$\underline{\xi} = \frac{1}{4} \frac{3(\underline{V}_r \cdot \underline{\mu})\underline{V}_r - V_r^2 \underline{\mu}}{V_r^2} .$$

V_r is the relative velocity of ion and electron (i.e. $\underline{V}_r = \underline{V}_i - \underline{V}$) where $\underline{V}_i$ is the velocity of the polarized electron. If the binding of these electrons is neglected, the average density of polarized electrons at the ion nucleus is given by $\rho = \langle\chi\rangle N\zeta$ where

$$\langle\chi\rangle = \frac{\langle 2\pi Z_p e^2 \rangle}{\hbar |\underline{V}_i - \underline{V}|} \approx \begin{cases} 2\pi Z_p \dfrac{V_o}{V} & \text{for } V > V_p \\ 2\pi Z_p \dfrac{V_o}{V_p} & \text{for } V < V_p \end{cases}$$

The average velocity of polarized electrons V_p is defined by $\left\langle \frac{1}{V_i} \right\rangle \equiv \frac{1}{V_p}$. It is expected that V_p is of the order of magnitude of $V_o = \frac{c}{137}$. The expression for ρ should be multiplied by the probability that the ion meets a polarized electron. This probability must vanish[L1] when the ion's velocity becomes so small that it cannot come sufficiently close to the atoms (very low energies - 10 t 20 keV). At higher energies, the ion can move freely through the lattice and $P(V) \approx 1$.

Neglecting the asymmetry correction, which vanishes if $V < V_p$, the nuclear spin will precess around the direction of magnetization. The differential precession, $d\phi$, is given by

$$d\phi = \frac{g\mu_N B}{\hbar} \, dt$$

where $g\mu_N$ is the nuclear magnetic moment, g the nuclear g-factor.

To change from a time-variable to a velocity variable, one employs the stopping cross-section S defined by $\frac{dE}{dR} = NS(v)$ where N is the number of atoms/unit volume. Since $\frac{dE}{dR} = \frac{dE}{dt}\left(\frac{dt}{dR}\right)$ and $\frac{dR}{dt} = v$, substitution gives $dt = \frac{dE}{[vNS(v)]}$. Since $dE = Mvdv$

$$d\phi(v) = \frac{8\pi}{3} \frac{g\mu_B\mu_N}{\hbar} \zeta M \frac{\langle\chi\rangle}{S(v)} \, dv \, .$$

The total precession for an ion which starts with initial velocity v' is given by

$$\phi(v') = \frac{8\pi}{3} \frac{g\mu_B\mu_N}{\hbar} \zeta M \int_{v_c}^{v'} \frac{\langle\chi\rangle dv}{S(v)}$$

where M is the mass of the ion and V_c is a lower cutoff velocity for the transient field.

Several features of this equation are worthy of note. The precession angle is independent of N, the density of the material; it is proportional to Z_p, the charge number of the ion and also proportional to ζ, the number of polarized electrons per atom.

It is important to consider the validity of the various approximations which have been made in this development. It has been found that relativistic effects are of importance for heavy ions, and that these effects may be included approximately by multiplying the effective magnetic field B and the precession angle ϕ by the factor $C_{rel} \approx 1 + \left(\frac{Z_p}{84}\right)^{5/2}$.

The effect of the binding of the polarized electrons is expected to be small if the velocity of the ion is larger than

the electron velocities V_i. At lower velocities, the effect of binding is difficult to estimate; since the contribution to the transient effect is important at low velocities, this is a serious drawback. To try to account for this effect, one approach is to treat V_p as an empirical parameter to be determined from experiment. One of the objectives of the present work is to determine a value for V_p by examining the behaviour of the transient field at low velocities $V \lesssim \frac{V_o}{2}$.

Finally, Lindhard and Winther point out that there is an uncertainty in the theory due firstly to the existence of possible resonance effects in the ion potential and secondly to the effect of the partially filled bound states on the ion. They incorporate this uncertainty as a multiplying constant C_{ion} for the enhancement factor χ. The resonance effects in the factor χ could be as large as 50%, but are probably much smaller due to the effect of the ion's bound electrons[W1].

E. SLOWING DOWN TIMES

The collision between a target atom and a projectile (e.g. proton, alpha particle, or ^{16}O ion) of several Mev energy produces a recoiling target ion with energy in the Mev region. The maximum possible recoil energy for an incident projectile energy E_i is given by

$$E_r = \frac{4A_T A_P}{(A_T+A_P)^2} E_i$$

where A_P and A_T are the mass numbers of projectile and target

respectively. The largest recoil energies encountered in the present work occurred with oxygen ions (E_i = 35 Mev, A_p = 16). For Rh target atoms (A_T = 103), the largest recoil energy was 16.3 Mev. To find the stopping time, one uses the fact that $\frac{mdv}{dt} = -\frac{dE}{dR}$, where $-\frac{dE}{dR}$ is the energy loss per unit path length; one finds that

$$\text{stopping time } t = \sqrt{\frac{m}{2}} \int_0^{E_r} \frac{dE}{E^{\frac{1}{2}}\left(\frac{dE}{dR}\right)} \quad .$$

Lindhard et al.[L2] have developed a theory of stopping power for heavy ions of moderate velocity; the theory uses a Thomas-Fermi electron distribution for electronic stopping and a power law for nuclear scattering at low velocities. Ranges calculated using the Lindhard theory are generally in good agreement with experimentally-measured ranges. Calculated slowing down times are usually less than 1 picosecond.

For 35 Mev ^{16}O ions and 10 Mev alpha particles incident on ^{103}Rh, the maximum recoil energies are 16.3 Mev and 1.44 Mev respectively. The stopping times in $Fe_{80}Rh_{20}$ alloy were calculated to be .89 psec and .34 psec respectively. The corresponding stopping times for Pt recoils in $Fe_{85}Pt_{15}$ were calculated to be .64 psec and .29 psec respectively.

F. RADIATION DAMAGE IN METALS BY ENERGETIC HEAVY IONS

This subject is important because it can be the determining factor in deciding not only the final position of the recoiling ion but also the environment that the ion sees after it has come

to rest. A survey of the voluminous literature on the subject of radiation damage makes it apparent that it is difficult to devise a theory that can make quantitative contact with experiment except in very special cases. The theory is however, useful in providing order of magnitude estimates and at least a qualitative understanding of the damage problem.

Several general observations can be made. If bombardment occurs at a low enough temperature that both of the simple point defects, vacancies and interstitials, can be considered immobile (e.g. 4°K), then the damage will consist almost entirely of point defects, whose density increases linearly with radiation dose because the recombination probability is small. At a higher temperature, (say > 100°K) where one or both of the point defect types are mobile, two new effects modify this simple picture. If two defects of opposite type encounter each other, they will recombine and mutually annihilate. If two defects of the same type come together, they can find it energetically favourable to remain together at that position; this immobile divacancy or di-interstitial then acts as a nucleation point to which further defects of like type will attach themselves if they happen along (homogeneous nucleation). The rate of recombination and the rate of growth of defect clusters are functions of dose rate and temperature. Recombination reduces damage but the growth of defect clusters inhibits recombination by restricting defect mobility. It should be noted that any defect in the crystal structure (impurity or dislocations) can also serve as a nuclea-

tion point for the growth of vacancy or interstitial clusters ('trap' nucleation). In the case of a polycrystal, a grain boundary is an array of dislocations; one would expect that the growth of damage would not be homogeneous in polycrystals because the growth of defect clusters would be enhanced at the grain boundaries. A third type of cluster nucleation ("spike" nucleation) is associated with the collision cascade phenomenon that occurs near the end of an ion's path.

To appreciate the importance of the collision cascade phenomenon, one should examine the processes of energy loss of the ion as it moves through the material. At high energy (e.g. 1 Mev), the predominant mechanism of energy loss is electronic excitation which raises the local temperature of the lattice but does not result in permanent displacement of lattice atoms. At these energies, a minor source of energy loss is elastic Rutherford collisions between the nuclei of projectile and target atoms. A fraction of these collisions are inelastic and correspond to the Coulomb excitation events in which we are interested. Elastic Rutherford collisions are responsible for the primary damage events that occur over most of the ion's range. However, as will be shown, the most serious damage is produced by the heavy target atoms recoiling following these Rutherford collisions. As the ion's energy degrades, the effective charge on the ion increases and, as a result, electronic energy loss decreases; the Rutherford cross-section increases with decreasing

energy, so eventually the nuclear energy loss dominates the electronic energy loss. Finally, the recoiling ion becomes neutral, and below this energy the electronic screening of the nuclear charges is so complete that the collisions are now of the hard-sphere or billiard ball type in which the impenetrable electron clouds play a dominant role. An estimate of the recoil energy at which the ion becomes neutral and a separate estimate of the energy at which electronic energy loss becomes negligible compared to the hard-sphere collision contribution show that the two energies coincide approximately and are given by

$$E_{hs} \sim A \text{ keV}$$

where A is the atomic mass number of the recoiling ion. Below this energy, the ion loses energy rapidly via a succession of hard-spherecollisions with the target atoms. Most of these target atoms have sufficient energy to initiate hard-sphere collisions with other target atoms, and so on. This collision cascade near the end of an ion's path produces a large number of displacements over a relatively small region. For heavy ions, an order of magnitude estimate of the number of displaced atoms N_d in the cascade, can be obtained from the expression $N_d = \frac{E_{hs}}{2E_d}$ where E_d is the minimum energy necessary to produce one displacement. E_d is generally quoted as 25 ev., independent of target material.

So $$N_d \approx 20 \times A \quad .$$

N_d varies from 1000 to 4000 in passing from iron (A=56) to plati-

num (A = 195). For 10 Mev alpha particles stopping in iron, one obtains using a more detailed expression appropriate to light ions provided by Kinchin and Pease[K1], $N_d \approx 100$. In alloy systems, where two species of different mass are involved, the analysis of Baroody[B2] indicates that the energy provided by a primary knock-on is distributed quite evenly between the two components over a wide range of primary energy provided that the atomic mass numbers are not different by more than a factor of 10. This condition is well satisfied for Rh (A = 103) in Fe (A = 56) and for Pt (A = 195) in Fe. So the magnitude of cascade damage in our binary systems should not be greatly different from that in a pure metal.

In the present experiments, we are interested in the environment of Coulomb excited atoms. It is instructive to compare the profile of damage in the target with the profile of the Coulomb excitation cross-section as a function of projectile penetration depth (Fig. 2-2). Since the heavy Coulomb-excited target atoms have a very short range, the profile of the Coulomb excitation cross-section essentially defines the distribution of interesting Coulomb excitation events as a function of penetration depth. Radiation damage that occurs beyond the region where the Coulomb excitation probability is appreciable lies outside the region of interest and should not influence the environment of Coulomb-excited atoms. It is important to realize that the range of the incident projectiles is such that they always come to rest far beyond the region where the overwhelming number of Coulomb excita-

Figure 2-2

Radiation damage profiles for oxygen and alpha particle projectiles in ^{103}Rh. The total Coulomb excitation and Rutherford scattering cross-sections are plotted on the same graph as a function of penetration depth into the target to indicate how the distribution of Coulomb-excited atoms in the target is likely to be related to the distribution of accumulated radiation damage. The final diagram plots (ratio of Rutherford to Coulomb excitation cross-sections) vs (penetration depth) as a measure of the damage created per Coulomb excitation event for various projectile energies.

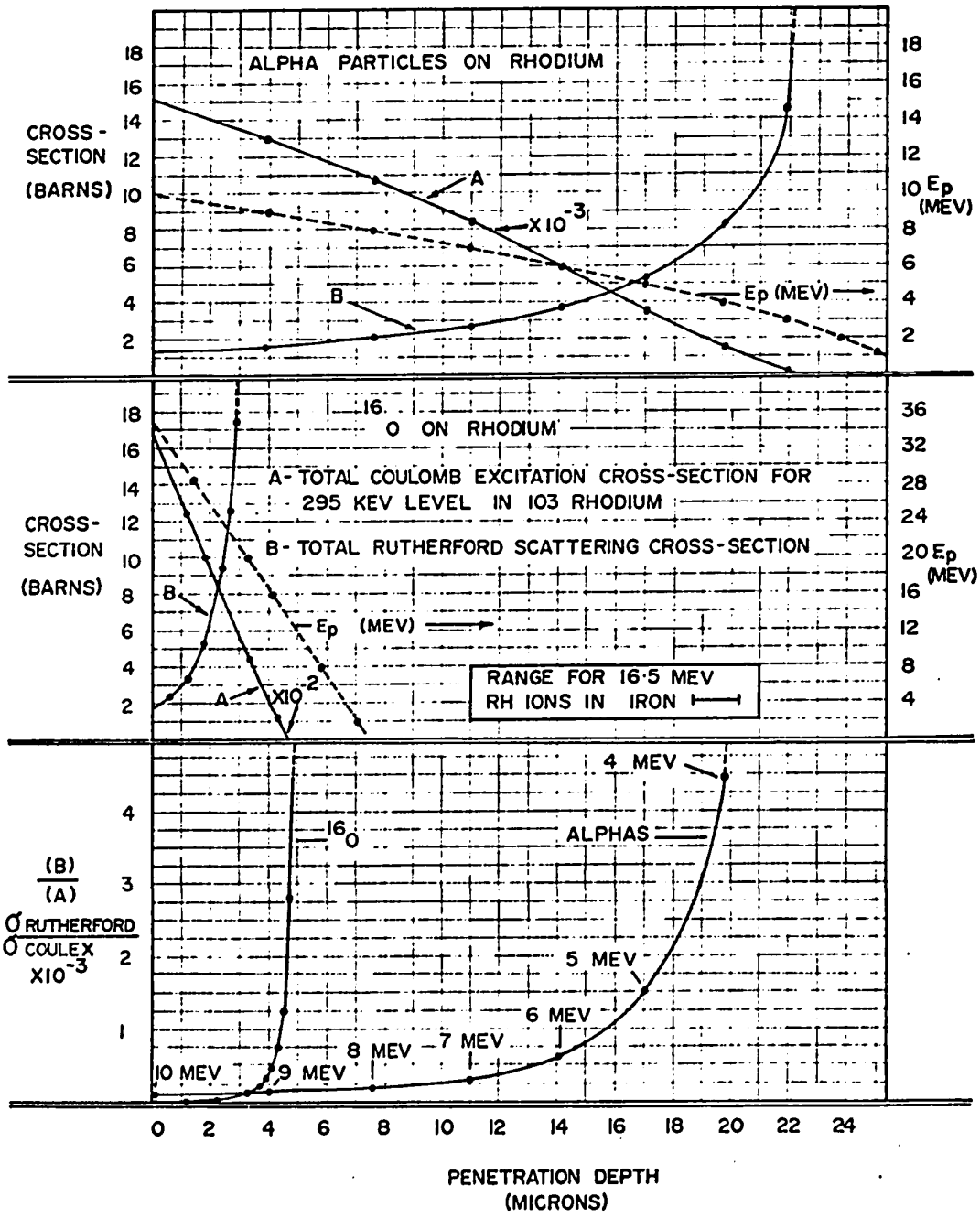

RADIATION DAMAGE PROFILES

Fig. 2-2

tion events occur; the damage caused at the end of the projectile's path should not, therefore, influence the environment of Coulomb excited atoms.

The important damage in the region of appreciable Coulomb excitation cross-section is caused by recoiling heavy target atoms which have undergone nuclear Rutherford collisions with the projectile. These atoms can have initial recoil energies as large as 16.9 Mev in our experiments. As discussed above, heavy ions may displace a hundred or so lattice atoms in slowing down to A keV, but the overwhelming majority of the displacements (numbering in the thousands) occur in the hard sphere collision region below A keV. As a first approximation, then, the number of collisions produced by such a heavy recoil can be considered independent of the initial recoil energy as long as that energy is greater than A keV.

(i) Accumulated damage

A simple estimate of the buildup of damage with time can be made by assuming that:

(1) there is no recombination of defects,

(2) the number of primary collisions at a given projectile energy is determined by the total Rutherford cross-section σ_R and the incident beam flux,

(3) each primary recoil produces the same number ν of displaced atoms, independent of initial recoil energy.

(2) and (3) taken together imply that the damage rate depends upon the projectile energy only through the inverse square energy dependence of the Rutherford cross-section. If one further

assumes that all projectiles at a certain depth in the target have the same energy (no straggling), then the damage rate will be a unique function of the penetration depth into the target.

For example, consider bombardment of pure iron by alpha particles with energy E. Assuming a beam current of .5 μA of $^4He^{++}$ and a beam spot of 3 mm. diameter, one obtains a flux = 2.21×10^{13} ions/cm^2/sec. The Rutherford crossection is $\sigma_R = (4.40\times10^{-23})/E^2_{Mev}$ cm^2.

Using a value for ν of 1000 for iron atoms recoiling in iron, one finds that

No. damage events/scattering centre/day = $8.4\times10^{-2}/E^2_{Mev}$.

The lowest energy for which the Coulomb excitation probability is appreciable is 3 Mev. At this energy, the damage density is 9.3×10^{-3} events/sc. centre/day. The density decreases quickly for higher projectile energy. The worst damage density, taking into account alloy concentration, beam flux, Rutherford cross-section and multiplicity ν was predicted for our experiment using 400 nA of 7 Mev alpha particles on $Fe_{85}Pt_{15}$ alloy for which the damage density at 3 Mev alpha energy was calculated to be 5.0×10^{-2} events/sc. centre/day.

If the estimates of the multiplicity factors ν are reasonably accurate, then the calculated damage densities are probably overestimates because no allowance has been made for recombination of defects. The assumption that, after one day of continuous bombardment the damage density is less than the 1%

level, in the target layer of interest would seem to be a reasonable one. The numbers indicate that the experiments in which the cumulated damage would be greatest are those using high current (.4-.6 μA) low energy alpha projectiles (7,6,5 Mev).

From the point of view of radiation damage, a useful comparison between the experiments employing different projectiles can be made by calculating the number of damage events per Coulomb excitation event in each case. Irrespective of the beam flux, this number is given by $\frac{N_D}{N_{CE}} = \frac{\sigma_R \nu}{\sigma_{CE}}$. The ratio $\frac{\sigma_R}{\sigma_{CE}}$ will be a function of the incident energy E. It has been plotted in Fig. 2-2 for the case of alpha particles on pure rhodium and ^{16}O ions on pure rhodium for direct excitation of the 295 keV state. While the absolute values of the numbers can have considerable uncertainty associated with them, the relative values are significant. They clearly indicate that the use of more energetic projectiles is an advantage from the point of view of reducing the amount of cumulated radiation damage in such experiments. However, there are certain advantages to the use of low energy, light projectiles, namely low background and minimization of transient field effects. To decide whether the higher damage level associated with these low energy experiments is significant, one must first decide whether a 1% level of damage density is likely to affect the value of the hyperfine field seen by a Coulomb-excited atom after it has come to rest. A 1% level of damage density means

that, on average, one in every hundred atoms in the lattice has been displaced. If the damage distribution is assumed uniform and isotropic, then this implies that a Coulomb-excited atom will have,on average, a fourth or fifth nearest neighbour that has been displaced. Since the magnetic dipole interaction is almost entirely a nearest neighbour interaction, it is unlikely that such a displacement would affect the hyperfine field at the site of the Coulomb excited nucleus. These simple arguments have assumed that the damage distribution is homogenous over microscopic portions of the target; the growth of defect clusters, particularly at grain boundaries clearly calls this assumption into question. However, the effect of such inhomogeneous aggregations of defects is very difficult to estimate, and no attempt has been made to do so.

ii) Self-damage

The above analysis has concerned itself with the damage density seen by a recoiling Coulomb-excited target atom due to all of the damage events that have occurred since the beginning of the experiment. However, while a particular Coulomb-excited atom is slowing down, it initiates its own collision cascade near the end of its range, and this damage in the immediate vicinity of the stopped atom could be of high density during the short time ($< 10^{-10}$ sec) that the excited state takes to decay. Calculations by Liebfried[L3] of the interstitial density at the centre of a collision cascade as a function of primary energy

indicate that this density peaks at 5% when the recoil energy is about 1 kev and that the density has dropped to near 1% when the primary's energy has dropped to 30 eV. These results are complemented by the work of Bernas et al.[B1] who used stereoscopic electron microscopy to measure the density of vacancy loops following implantation of 130 keV Yb into Au, Nb and Fe. They estimate that half of the vacancies produced may be in loops.

Due to energy straggling, there will be a distribution of stopping distances; these were calculated using the stopping theory of Lindhard et al.[L2]. Their results may be summarized by saying that the ion distribution tended to outdistance the vacancy distribution. The peak in the ion distribution occurred where the vacancy density was $\sim$ 1%; this is in agreement with Liebfried's calculations, but the comparison between the two results must be treated with care because Liebfried's calculations concern the stopping of an individual ion whereas the ion implantation experiments involve doses of 10^{11} - 10^{14} atoms/cm^2 over some period of time and so examine the integrated damage in the target.

Sigmund et al.[S3] have investigated the primary distribution of defect cascades for two different scattering cross sections, the first independent of projectile energy (hard-sphere scattering), and the second varying as E_p^{-m} where $0 \leq m \leq 1$. They integrated the relevant integral equations to obtain spatial averages over the defect distribution. Their results indicate that for $M_P >> M_T$ (where the subscripts refer to projectile and target respectively), there is uniform heavy damage throughout the cascade

region and there is significant separation of interstitials and vacancies (with vacancies concentrated along the ion trajectory) in the intermediate and lower kev region, even without considering the action of replacement sequences. In this case, one could expect the primary ion to stop in a vacancy-rich region. For $M_P \approx M_T$, there is evidence for a slight clustering effect. In this case, fluctuations in the trajectory would tend to overshadow the effect, so the fact that they see any tendency at all toward vacancy clustering along the trajectory, without considering replacement sequences, suggests support for the theory advanced by Brinkman that, when the ion comes to rest, it finds itself in a vacancy-rich region. For Rh in Fe, $\frac{M_P}{M_T} \approx 2$ and for Pt in Fe, $\frac{M_P}{M_T} \approx 3.5$, so the mass ratios lie somewhere between the cases $M_P \approx M_T$ and $M_P >> M_T$. If Brinkman's concept is correct, then one would expect the ion to stop substutionally with high probability.

(iii) Effect of damage on ordering in alloy

Radiation damage by heavy recoil ions can also affect the degree of spatial and magnetic ordering in an alloy. In this regard, replacement collisions, which typically outnumber displacements by factors of 4 or 5, can play a significant role. If the alloy is initially homogeneous and in a stable, highly-ordered phase, then radiation damage, particularly in the collision cascade, will most certainly reduce the degree of order. On the other hand, if the alloy is initially in a metastable disordered

state, and the thermodynamical equilibrium state involves some degree of order, then the production of isolated vacancies can enhance the approach to the ordered state by enhancing the diffusion rate; in a collision cascade, the diffusion rate can be greatly enhanced due to the large number of vacancies created and this fact, plus the need to relax large lattice strains, can precipitate microscopic phase changes in the vicinity of the cascade. The latter process is particularly likely at the very end of the ion's range, where the mean free path between collisions becomes comparable to or greater than the interatomic spacing and the ion must be considered to interact with many lattice atoms simultaneously; in this case it succeeds in displacing every atom along its path and produces a displacement "spike". When its energy has further degraded to below 25 eV, it does not have sufficient energy to displace a lattice atom, so the remaining energy is imparted to its neighbouring atoms as lattice vibrations and can effectively raise the local temperature to several thousand degrees K for a brief time. This so-called "thermal spike" which effectively melts a small volume of the lattice for a short time, and the "displacement spike" mentioned above can both help to precipitate local phase changes if such changes are thermodynamically favoured.

The effect of radiation damage on the alloys used in the present work depends upon the initial structure and degree of ordering in each alloy. Comments on these specific cases will be made in Chapter 6 in a discussion concerning the measured static

hyperfine fields.

G. FINAL POSITION OF RECOILING TARGET ATOMS

Some useful experimental and theoretical work has been done to investigate the question of the final position of heavy ions recoiling in a solid. The term "final" site refers strictly to the actual site that a recoiling atom occupies at the moment when it comes to rest in the lattice. However, if, for example, the atom stops initially in an interstitial position, it can continue to migrate through the lattice until it encounters a vacancy, thereby becoming substitutional. So the final site distribution of implanted atoms that is seen in an experiment will depend upon the length of time that has elapsed between the time that the ion first stopped in the lattice and the time at which the experimental probe examines the final site distribution. The time scale for room-temperature migration of a defect to a sink is on the order of tens of nanoseconds, so a probe which examines the final site distribution within a few nanoseconds after the ion has come to rest probably reflects a final site distribution that has not been appreciably altered by defect migrations. On-line experiments such as Mössbauer effect following Coulomb excitation and perturbed angular correlations following either Coulomb excitation or nuclear reactions are experiments which fall into this category because the excited nuclear probes decay with mean-lives usually less than or of the order of a few nanoseconds. On the other hand, almost all ion implantation experiments, in which the hyperfine field distribution for implanted ions is

examined by Mössbauer effect, nuclear orientation, or channelling, are affected by defect migration because the experiments are performed minutes or hours after the implantation. Exceptions may occur when the dose is so low that the defect recombination rate is very low and/or when the implant and subsequent experiment are both carried out at very low temperature (liquid helium temperature) so that the defect mobility is greatly reduced.

For the experiments in this thesis, most of the Coulomb-excited atoms decay in times $\lesssim$ .1 nsec., so their distribution of final sites should not be appreciably affected by defect migration. One should look to on-line experiments with nanosecond or subnanosecond probes for information on final sites that would be directly applicable to our experiments. The time-integral perturbed angular distribution technique which must be employed on such short-lived states measures only an internal field averaged over all final sites, so the technique does not permit one to detect the existence of different internal fields corresponding to different final sites. Borchers[B3] has shown that the observed effect in such an experiment is quite insensitive to a distribution in fields.

Even when the technique used does permit one to distinguish more than one hyperfine field, there remains the more difficult task of correlating the distribution of internal fields to the distribution of final sites. This problem is complicated by the fact that it has not been satisfactorily established that the high-field site is a substitutional or "normal" site. At present, it would seem that one can say only that detection of more than one

internal field implies more than one kind of final site; the actual nature and distribution of final sites on a nanosecond time-scale, however, are questions that remain unresolved.

Marmor et al.[M1] measured the hyperfine field of ^{42}Ca in Fe; they excited the 3.19 Mev 6^+ state in ^{42}Ca via the $^{39}K(\alpha,p)^{42}Ca$ reaction with a 10.03 Mev α beam and measured the time-differential perturbed angular correlation of de-excitation gamma rays from this state. Only one hyperfine field of statistical significance was observed. They employed the IMPAC technique, so the ^{42}Ca was a dilute impurity in the Fe matrix.

Various experiments employing Mössbauer effect following Coulomb excitation have been performed. Kalvius et al.[K3] recoiled excited ^{57}Fe atoms through vacuum into various media, including iron. Where comparison data on diffused sources are available (for Cu, Au, Al, and Fe), the results at room temperature indicate that within the nuclear lifetime of 10^{-7} sec, the recoils find a "normal" lattice site.

The incomplete body of data on final sites following ion implantation provides some useful information on the question of the uniqueness of internal fields. The data may be summarized by saying that, in general, at least two and sometimes three different hyperfine fields are detected following implantation. The high-field site is not necessarily substitutional. In all cases studied to date, the impurity was insoluble in the host matrix.

In an alloy, one can anticipate some interstitial and some substitutional recoils; however, due to the variety of

possible environments that a stopped atom can see in a partially-ordered alloy, one would expect a broader distribution of internal fields than the one- and two-field cases observed for dilute impurity implants in pure metals.

H. HYPERFINE FIELDS

The phrase "hyperfine magnetic field" refers to the magnetic field that exists at the site of a nucleus due to the surrounding electrons. The subject of hyperfine fields is extensive and well-documented[H1], so only a brief outline of the origin of these fields for the specific case of ferromagnetic metals will be presented here.

Most metals have large electric fields acting on the atoms in the lattice. This introduces a non-central force into the electron-nucleus interaction; as a result, the direction of the total angular momentum $\underline{L}$ is not constant in space, but changes continuously such that the time-average of the magnitude of $\underline{L}$ is zero. This so-called "quenching" of the orbital angular momentum decouples the total orbital and spin angular momenta and causes the major contribution to the hyperfine field to come from the electron spins. Unquenched orbital angular momentum is important for rare-earth metals, but not for 3d metals like iron.

Except for the case of the rare earths, the most important hyperfine contribution in ferromagnetic metals and alloys with cubic symmetry is that arising from the Fermi contact interaction.

This interaction, which is non-zero only for s-state electrons, occurs because s electrons have a non-vanishing spin density at the nucleus. For cubic symmetry, one might expect contact interaction for spin up and down to cancel. The field in this case is generated through the mechanism of core polarization (CP).

The field produced by CP arises from the Fermi contact term for paired electrons whose spatial behaviour at the nucleus is slightly different from one another. This difference in spatial behaviour occurs because electrons in the 1s and 2s shells that lie inside the 3d shell and with spin parallel to the 3d electron's spin have their spatial dependence changed by the s-d exchange interaction in such a way that they appear to be attracted outward; this results in a net negative spin density at the nucleus. The 3s electrons lie partly inside and partly outside of the 3d shell, so competing contributions to CP make the overall 3s contribution small but positive.

The analysis of hyperfine fields in metals is more complicated than in ionic crystals because the energy levels are broadened into bands, and an electron in a conduction band s cannot, in general, be considered to be localized on a particular atom. When a non-magnetic impurity is dissolved in a transition metal, especially in a ferromagnetic metal of the iron group, it is useful to distinguish between two kinds of valence electrons: those of the conduction band (comprised mainly of the 4s electrons), and those of the 3d band, responsible for ferromagnetism in Fe, Co and Ni. The 4s conduction band is very broad and has a very low

density of states per unit of energy, while, due to the weaker overlap of atomic d-orbitals, the 3d band is comparatively narrow, with a correspondingly high density of states. In the ferromagnetic state, the d-d exchange interaction lifts the degeneracy in energy between spin up and spin down electrons in the 3d band. This causes the density of states at the Fermi level to be slightly different for spin up and spin down 3d electrons, and produces the ferromagnetic state.

An important source of hyperfine field for a non-magnetic impurity dissolved in a ferromagnetic metal of the iron group is conduction electron polarization (CEP). The 4s-3d exchange interaction lifts the energy degeneracy for spin up and spin down 4s electrons; then, just as for core polarization, this alters the spatial behaviour of spin up and spin down s electrons at the impurity nucleus so that the spin up and spin down contributions to the Fermi contact interaction no longer cancel.

CHAPTER III

THEORY OF EXPERIMENT

A reasonably detailed development of the relevant physics has been given in Chapter 2; only useful results from that discussion will be quoted in this chapter.

First will be presented an explanation of how the existence of the transient field was demonstrated and some of its properties deduced; then will follow a development of the expected velocity dependence of the transient field based upon the theory of Lindhard and Winther. Finally, the transient field effect is incorporated into the theory of perturbed angular distributions following Coulomb excitation. The technique for testing the expected low velocity behaviour of the transient field using singles experiments is developed.

A. COMPARISON OF BETA-DECAY AND HEAVY ION EXPERIMENTS

As has been discussed, measurement of the rotation angle $\omega\tau$ permits the product $gH\tau$ to be determined for short-lived states. If any two of these three quantities have been measured in independent experiments, the third can be determined from a measurement of $\omega\tau$.

Measurement of the rotation angle $\omega\tau$ by a perturbed angular correlation is a commonly-used technique for measuring

g-factors of nuclear excited states. Different techniques are available for populating the excited state so as to produce an anisotropic angular distribution of de-excitation gamma-rays. Among the techniques are beta-decay from a neighbouring nucleus, Coulomb excitation, nuclear reactions, and resonance absorption.

There are significant differences between these processes which are worthy of note. In most cases of practical interest, the beta-decay feeds a nuclear level higher in energy than the one of interest; this level then gamma-decays to the level of interest, which in turn gamma-decays to the ground state, and the gamma-gamma angular correlation for this cascade is observed using coincidence circuitry. Coulomb excitation can populate the state of interest directly; as has been discussed, the gamma ray angular distribution may be anisotropic whether or not the gamma ray is detected in coincidence with the backscattered projectile.

Nuclear reactions can populate the level of interest either directly or indirectly; if the reaction energy is chosen to be just above threshold, then the limitation on the angular momentum of the outgoing particle will ensure an anisotropic distribution of de-excitation gamma rays from the residual nucleus even if the outgoing particle is not detected.

Resonance fluorescence populates the state directly. A gamma ray from the source atom is used to excite the same energy level in a target atom of the same species. The process of

resonant gamma-ray absorption can produce a very anisotropic distribution of de-excitation gamma rays; the resonance fluorescence technique consists of detecting these de-excitation gamma-rays and observing the perturbation of their angular distribution when an external magnetic field is applied. Metzger[M1] used ^{56}Fe as source and absorber, and, taking advantage of the large internal field in iron, measured an observable rotation angle for the 847 keV level in ^{56}Fe which has a mean-life of 11 psec. Mossbauer effect, or recoilless resonance absorption is not very useful for such shortlived states because (1) $\Delta E\tau \sim \hbar$ implies that the width ΔE of the resonance can become wider than the hyperfine splitting for mean lives shorter than a fraction of a nanosecond, (2) the transition energy E_t for vibrational states with short mean-lives is large, and this makes the recoil energy ($E_r \sim (E_T)^2$) so large that the recoilless fraction becomes too small to be useful.

For a given mass number, as one moves away from the centre of the valley of beta-decay stability, the beta-decay half-life decreases; as well, some radioactive parent isotopes are difficult to produce by neutron bombardment due to low abundance or low formation cross-section. Primarily for these reasons, not all low-lying nuclear levels can be populated by beta - decay in a way that is experimentally useful. Many first 2+ states in even-even nuclei have short mean-lives - typically 10 to 100 psec. Perturbed angular distributions following Coulomb excitation provides a useful tool for studying these states

(pure E2 transition, B(E2) proportional to τ^{-1} , and magnetic perturbation large enough to produce an observable rotation angle), particularly when the states are not easily accessible by beta-decay. Several of these states can be studied by both methods. Comparison of the results obtained for these states using beta-decay and Coulomb excitation provided the first evidence for the transient magnetic field phenomenon whose behaviour is the subject of the experiments reported in this work.

If the element of interest has more than one isotope, each isotope has the same electronic configuration, and so will experience the same average internal magnetic field H. Of course, excited states in each isotope can have different g-factors and mean lives. It is usually possible to measure simultaneously the rotation angle $\omega\tau$ for several states in different isotopes of the same element. If each of these states is a first 2+ state in an even-even isotope, almost all of the measured g-factors for such states as well as theoretical calculations support the fact that their g-factors should be approximately the same: positive and $\sim \frac{Z}{A}$ in value. However, when the same g-factors were measured using Coulomb excitation with heavy ions, those belonging to states having the shortest mean lives were found to depart considerably from the $\frac{Z}{A}$ rule, and in some cases to be negative.

A clue to the cause of the discrepancy for the very short-lived states between the g-factors measured by beta decay

and by Coulomb excitation with heavy ions can be obtained by plotting the rotation angles $\omega\tau$ measured by Coulomb excitation as a function of mean-life τ. If each of the rotation angles is proportional to mean-life τ, then together they should define a straight line with zero intercept, and slope ω (assuming that their g-factors are the same). This is indeed the case within experimental error for the rotation angles measured using beta-decay. However, the corresponding rotation angles measured using Coulomb excitation with heavy ions define a straight line with approximately the same slope but with an intercept that is definitely non-zero. Furthermore, in almost all cases studied the sign of the intercept is opposite to the sign of the external magnetizing field. This difference is illustrated by the data in Figure 3-1 collected using the IMPAC technique.

Taken together, the data seem to indicate that Coulomb excitation with heavy ions has associated with it an additional rotation of magnitude comparable to the rotation angles observed in beta-decay but (for negative internal fields) usually of the opposite sign. Moreover, this rotation angle seems to be equal (within experimental error) for all of the first 2+ levels belonging to isotopes of the same element even for a state whose mean life is $\sim$ 2 psec[Hl]; the latter facts seem to indicate that the mechanism causing this additional rotation

Figure 3-1

Comparison of observed rotation angles for (1) IMPACT experiments and (2) radioactivity measurements in diffused sources, for the even-even isotopes of platinum. IMPACT results have been taken from the work of the Wisconsin group[K7]; radioactivity results are the accepted averages of several measurements, as summarized in reference B7. The data are plotted using the most recent (and most accurate) mean lives available at time of writing[B7].

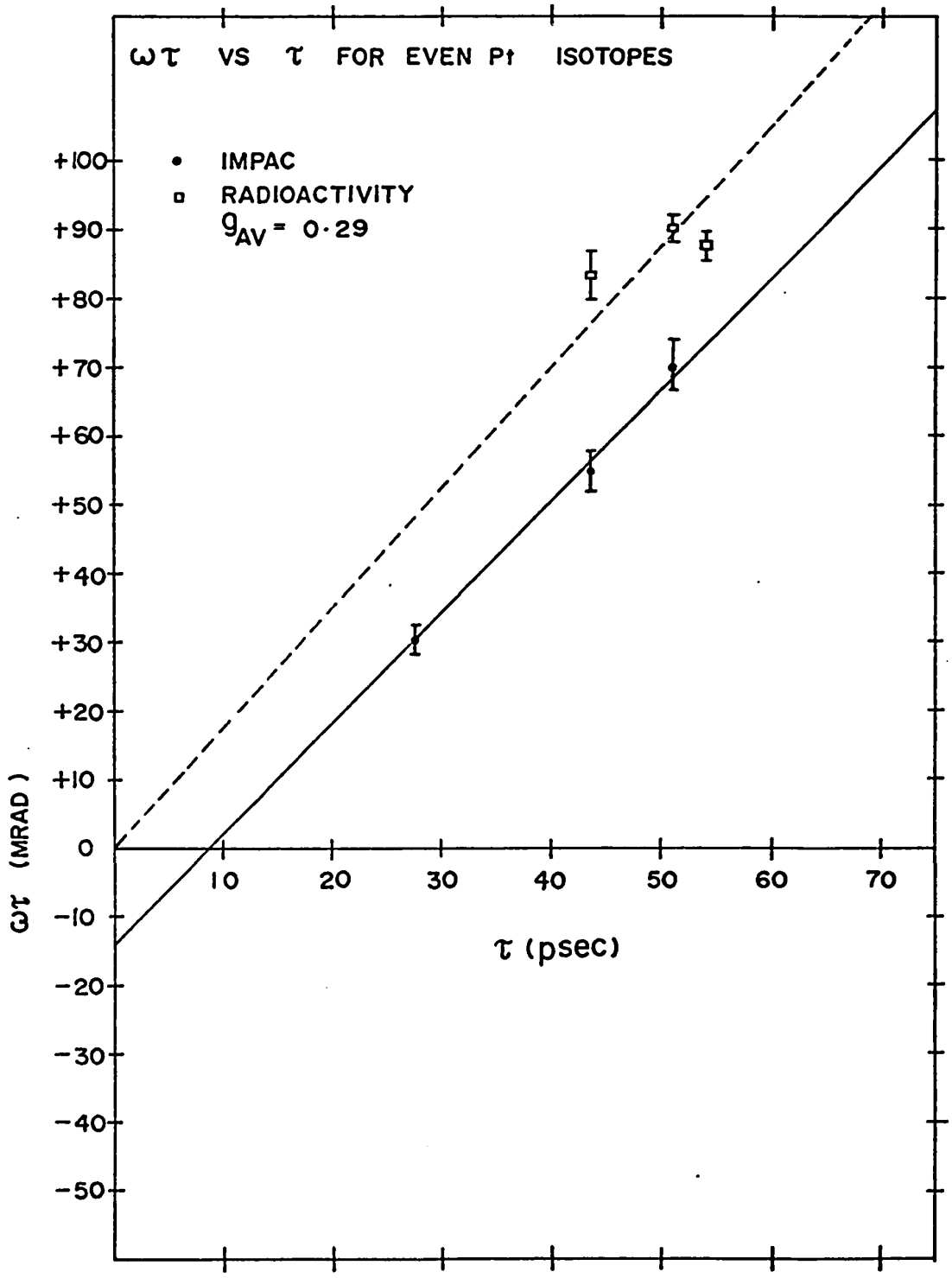
ωτ VS τ FOR EVEN Pt ISOTOPES
IMPAC
RADIOACTIVITY
g_{AV} = 0·29
+100
+90
+80
+70
+60
+50
+40
+30
+20
+10
0
-10
-20
-30
-40
-50
ωτ (MRAD)
10
20
30
40
50
60
70
τ (psec)

Fig. 3-1

imparts its full effect in a time small compared to 1 psec, and is independent of mean life. The wide variation in g-factors for short-lived states measured by Coulomb excitation is caused by the fact that for these states, the static and transient contributions are comparable in magnitude; the net observed rotation angle is the sum of the two contributions (i.e. $\Delta\theta = \omega\tau + \phi_T$).

The data are consistent with the existence of a large magnetic perturbation having the same sign as the external magnetizing field. Since a typical slowing-down time for heavy ions in iron or nickel is $\lesssim$ 1 psec., it is further reasonable to conclude that this perturbation imparts all or almost all of its effect during the time that the ion is slowing down in the ferromagnetic backing.

Since this perturbation seems to be associated primarily with the very brief slowing-down time of the ion in the ferromagnetic backing material it is referred to as a "transient field".

To explain why the transient field would exist for ions recoiling following Coulomb excitation with heavy ions but not for ions recoiling following beta-decay, one must examine the differences in the recoil processes for two cases. In beta-decay, momentum conservation requires that the nucleus recoil when the beta particle is emitted. A typical recoil energy for the nucleus is 1 kev. This corresponds for A = 100 to a maximum initial recoil velocity of 4.4×10^6 cm/sec ($\frac{V}{C} = .00015$).

However, for a 35 MeV O ion in head-on collision with a nucleus of mass 100, the recoiling nucleus has an initial energy of 16.6 MeV, corresponding to $\frac{v}{c} = .019$. This large difference in recoil velocity is the most notable difference between the recoil processes for the two cases. Lindhard and Winther[L1] have developed a theory which accounts for the transient field as a function of recoil velocity v (Sec.2-d).

B. THEORETICAL VELOCITY - DEPENDENCE OF TRANSIENT FIELD

From Chapter II, the reader will recall that Lindhard and Winther[L1] attribute the transient field to the scattering of unbound polarized electrons by an ion as it recoils in a magnetized ferromagnetic material. The scattering in the ion nucleus' Coulomb field produces an enhancement χ of the electron spin density at the ion nucleus. The magnetic moment of the nucleus sees this enhanced electron spin density as a magnetic field B, in the direction of magnetization, and of magnitude $\underline{B} = \frac{8\pi}{3} \rho(1+\xi)\underline{\mu}_B$ where $|\underline{\mu}_B|$ is the Bohr magneton. ξ is an asymmetry correction necessitated by the fact that the direction of the ion's motion is not coincident with the direction of magnetization. This correction is usually quite small. ρ is the density of polarized electrons at the ion nucleus, and neglecting the binding of the electrons, it can be shown that $\rho = \langle\chi\rangle N\zeta$ where N is the number of atoms/cm^3 and ζ is the number of electrons per atom polarized in the direction of magnetization. $\langle\chi\rangle$ is given by

$$\langle\chi\rangle = \left\langle \frac{2\pi Z_{pe}^{\ 2}}{\hbar|\underline{v}_i - \underline{v}|} \right\rangle \approx \begin{cases} 2\pi Z_p \dfrac{v_o}{v} & \text{for } v > v_p \\ 2\pi Z_p \dfrac{v_o}{v_p} & \text{for } v < v_p \end{cases} \qquad (3\text{-}1)$$

v_i is the electron velocity and v is the ion velocity; v_p is an average electron velocity defined by $\frac{1}{v_p} \equiv \langle\frac{1}{v_i}\rangle$, $\langle\ \rangle$ denoting an average over all possible directions of the electron velocity.

The expression for $\underline{B}$ in the direction of magnetization becomes

$$B = \frac{16\pi^3}{3} \mu_B N (1+\xi) Z_p \zeta \begin{cases} \dfrac{v_o}{v} & \text{for } v > v_p \\ \dfrac{v_o}{v_p} & \text{for } v < v_p \end{cases} \qquad (3\text{-}2)$$

It is seen that B varies as $\frac{1}{v}$ down to some velocity v_p and is expected to be constant and non-zero below v_p (Fig. 3-2).

The reader will recall that if the ion nucleus has magnetic moment $g\mu_N$ then in time dt it precesses about the field B with a differential precession angle $d\phi = \frac{g\mu_N B}{\hbar}\, dt$. When the time variable is converted to a velocity variable, the expression is

$$d\phi = \frac{8\pi}{3} \frac{g\mu_B\mu_N}{\hbar} \zeta\, M \frac{\langle\chi\rangle}{S(v)}\, dv \qquad (3\text{-}3)$$

where M is the mass of the ion and S(v) is the total stopping cross-section.

At high velocities, B is proportional to $\frac{1}{v}$ and S(v) is proportional to v, so $d\phi$ is proportional to $\frac{1}{v^2}\, dv$.

At low velocities, B is constant, and S(v) is approximately constant, except at very low velocities, so in part of the low

velocity region $d\phi \sim dv$.

For an ion that slows down from initial velocity v' to rest, the total precession is given by

$$\phi(v') = \int_{v'}^{v_{cutoff}} d\phi$$

where v_{cutoff} is the velocity below which the transient field turns off.

C. EFFECT OF TRANSIENT FIELD ON PERTURBED ANGULAR DISTRIBUTION

The incorporation of the theory of the transient field into the expression for the perturbed angular distribution must be handled differently for a singles experiment than for a coincidence experiment. This is necessitated by the fact that the recoil velocity of the Coulomb excited nucleus is related to the scattering angle for the incident ion. In a singles experiment, what is observed is an effect averaged over the scattering angle of the incident ion, and, consequently, averaged over a wide range of recoil velocities. In a coincidence experiment the backscatter ions detected by a particle detector in a narrow angular band near 180° ensure that the corresponding recoiling ions will move in a narrow forward cone; there will be only a small spread in velocities, and all of these velocities will be slightly less than the value corresponding to a head-on collision.

In a collision between projectile ion of mass number A_p and target atom of mass number A_T, the non-relativistic expression relating the recoil energy E_r of the target atom to the scattering angle θ_p of the projectile in laboratory coordinates is

$$\Delta E = E_r\left(1 + \frac{A_p}{A_T}\right) - E_i\left(1 - \frac{A_p}{A_T}\right) - \frac{2A_p}{A_T}\sqrt{E_i E_r}\cos\theta_p \quad (3\text{-}4)$$

where ΔE is the excitation energy and E_i is the incident projectile energy. If terms in $\left(\frac{A_p}{A_T}\right)^2$ are neglected in the solution for E_r then one obtains the simple expression (valid to $\leq 1\%$ for all values of θ_p for the values of A_p and A_T considered in the thesis)

$$E_r = \frac{2A_pA_T}{(A_p+A_T)^2} E_i(1-\cos\theta) - \Delta E\left(\frac{2A_p}{A_p+A_T}\right) \quad (3\text{-}5)$$

Now consider the angular distribution appropriate to an ion Coulomb excited in a collision with a projectile that is is scattered at angle θ_p (see Section 2-B)

$$W(\theta_\gamma) = b_0 + b_2(\theta_p,\xi)\cos(2\theta_\gamma) + b_4(\theta_p,\xi)\cos(4\theta_\gamma) \ . \quad (3\text{-}6)$$

If, in a time t, a magnetic perturbation H acts to produce a rotation of the angular distribution through angle $\Delta\theta$, then

$$W(\Theta_\gamma,H,t) = b_0 + b_2\cos\left[2(\Theta_\gamma-\Delta\theta)\right] + b_4\cos\left[4(\Theta_\gamma-\Delta\theta)\right] \quad (3\text{-}7)$$

where $\Delta\theta$ is a function of H and t.

To decide upon the form of $\Delta\theta$, it is useful to divide the time domain into two segments, $t < t_s$ and $t > t_s$, where t_s is the stopping time of the ion. If the transient rotation acts only during the slowing down time of the ion and if the static field is constant and acts only after the ion has come to rest, then

$$\Delta\theta = \phi(t) \text{ for } t < t_s \text{ where } \phi(t) = \int_0^t \omega_T dt'$$

$$= \omega \cdot (t-t_s) + \phi(t_s) \text{ for } t > t_s \ . \qquad (3\text{-}8)$$

The angular distribution, when averaged over time, must be weighted by the exponential decay factor $e^{-t/\tau}$ for the nuclear state:

$$\frac{1}{\tau}\int_0^\infty W(\theta_\gamma - \Delta\theta)e^{-t/\tau}dt = \frac{1}{\tau}\int_0^{t_s} W(\theta_\gamma - \Delta\theta)e^{-t/\tau}dt +$$

$$+ \frac{1}{\tau}\int_{t_s}^\infty W(\theta_\gamma - \Delta\theta)e^{-t/\tau}\,dt \ . \qquad (3\text{-}9)$$

Using the small angle approximation $\sin k\Delta\theta \approx k\Delta\theta$ and $\cos k\Delta\theta \approx 1$ the second integral gives

$$(2) = e^{-t_s/\tau}\sum_k \frac{b_k}{[1+(k\omega\tau)^2]}\left[\cos k\theta + k(\omega\tau+\phi(t_s))(\sin k\theta)\right] \qquad (3\text{-}10)$$

The first integral, using the same small-angle approximations, gives

$$(1)\sum_k b_k\left[\cos k\theta\,(1-e^{-t_s/\tau}) + (k\sin k\theta_\gamma)\int_0^{t_s}\phi(t)e^{-t/\tau}\,\frac{dt}{\tau}\right] \qquad (3\text{-}11)$$

Now for the rotation angles in this thesis, the attenuation factors $1 + (k\omega\tau)^2$ are ≈ 1.

Combining (1) and (2) yields

$$W(\theta_\gamma,H,\infty)=\Sigma_k b_k\{\cos k\theta_\gamma+k\sin k\theta_\gamma[\int_o^{t_s}\phi(t)e^{-t/\tau}\frac{dt}{\tau}+e^{-t_s/\tau}(\phi(t_s)+\omega\tau)]\} \quad (3\text{-}12)$$

If the angle $\theta_\gamma = 135°$ used in the experiments is inserted, one finds that

$$W(135°,H,\infty) = 1-b_4-2b_2[\omega\tau e^{-t_s/\tau}+\int_o^{t_s}\omega_T e^{-t/\tau}\,dt \quad (3\text{-}13)$$

The weighted transient rotation is defined by

$$\phi_w(t_s) = \int_o^{t_s}\omega_T e^{-t/\tau}\,dt \quad (3\text{-}14)$$

where the subscript "T" stands for "transient".

Equation (3-13) is the perturbed angular distribution appropriate to events in which the projectile is scattered at angle θ_p and the recoil nucleus has a corresponding initial recoil velocity v_r^i, specified by equation (3-5).

Because the experiment in which the gamma ray is detected in coincidence with the scattered projectile restricts θ_p to a narrow band of angles near 180°, and restricts v_r to a narrow band of velocities just below the head-on collision velocity, the variation in θ_p and v_r can be safely ignored; expression (3-13) correctly describes the perturbed angular distribution for this type of experiment.

However, for the singles experiments described in this thesis events are accepted irrespective of the projectile's back-

scatter angle; this implies that the observed result must correspond to a distribution averaged over all possible backscatter angles (and consequently over all possible target atom recoil velocities).

(i) Average over scattering angle

The analysis is complicated by the fact that the angular distribution coefficients b_2 and b_4 as well as the weighted transient rotation $\phi_w(t_s)$ and the stopping time t_s vary as function of backscatter angle θ_p; the latter two quantities depend indirectly upon θ_p through their dependence upon recoil velocity. The dependence of b_2 and b_4 upon θ_p can be calculated using the Coulomb excitation theory outlined in Chapter 2; the variations of $\phi_w(t_s)$ and t_s with θ_p depend upon the models that are assumed for the transient field and for the stopping cross-section.

The only quantitative model for the transient field to date has been provided by Lindhard and Winther[L1]. The same authors have also provided a universal theory of stopping power that accounts for both nuclear and electronic stopping[L2].

As discussed in Chapter II, the differential Coulomb excitation probability is a function of backscatter angle θ_p. The required average over θ_p is given by $\bar{W} = \int_0^\pi W(\theta_p)P(\theta_p)d\theta_p$ where the normalized Coulomb excitation probability is given by

$$P(\theta_p) = \frac{df}{d\Omega}(\theta_p,\xi)\sin\theta_p \Big/ \int_0^\pi \frac{df}{d\Omega}(\theta_p,\xi)\sin\theta_p d\theta_p \quad . \qquad (3\text{-}15)$$

As noted in Chapter II, tables of values of $\frac{df}{d\Omega}$, calculated semi-classically, are available[Al]. These tables were used for the calculation of $P(\theta_p)$. The parameter ξ is constant for definite values of incident projectile energy, excitation energy, and a given choice of target and projectile. The values of the angular distribution coefficients $b_2(\theta_p,\xi)$ and $b_4(\theta_p,\xi)$ were also calculated semi-classically. Letting $\bar{b}_2(\xi)$ represent b_2 averaged over θ_p, etc. and using expression (3-13) for W, one finds that

$$\bar{W}(135°,H,\infty) = \bar{b}_0-\bar{b}_4-2[\overline{b_2 e^{-t_s/\tau}\,\omega\tau} + \overline{b_2\dot{\phi}_w}] \qquad (3\text{-}16)$$

$$= \bar{b}_0-\bar{b}_4-2\bar{b}_2[\omega\tau + \frac{\overline{b_2\dot{\phi}_w}}{\bar{b}_2}] \text{ assuming } e^{-t_s/\tau} \approx 1 .$$

It is usual to express the angular distribution with the first term normalized to 1. This can be accomplished by dividing all terms by $\bar{b}_0$.

Because the stopping time t_s is related to a unique initial recoil velocity, and the initial recoil velocity is related to a unique backscatter angle θ_p, ϕ_w can also be considered to be a function of θ_p. So

$$\bar{\dot{\phi}}_w \equiv \frac{\overline{b_2\dot{\phi}_w}}{\bar{b}_2} = \int_0^\pi b_2(\theta_p)\dot{\phi}_w(\theta_p)P(\theta_p)d\theta_p \Big/ \int_0^\pi b_2(\theta_p)P(\theta_p)d\theta_p \qquad (3\text{-}17)$$

The above expression has been integrated numerically. The results for a representative case are shown in Fig. 3-2; the

effect of averaging over θ_p, and convolution with the function $b_2(\theta_p)$ can be seen by comparing with the values of ϕ_w also plotted in this figure.

(ii) Thick-target average

There is a further modification to the theory that is required. In a coincidence experiment, all of the Coulomb excitation of the target atoms occurs in a thin ($\sim$ 100 μgm/cm^2) layer of target material coated on the front surface of a ferromagnetic foil. Energetic heavy ions passing through this layer lose only a small fraction of their initial energy, so Coulomb excitation of the interesting target atoms takes place at what is effectively a single projectile energy. In a singles experiment, the target atoms are distribted uniformly throughout a ferromagnetic lattice; not all of the interesting Coulomb excitation events occur at the surface of the target. As the projectile moves into the target it loses energy and the total Coulomb excitation cross-section (i.e. cross-section irrespective of backscatter angle) decreases. The variation of incident projectile energies at which Coulomb excitation occurs implies a corresponding variation in the ξ parameter. It is therefore necessary to average the angular distribution again to account for the effect of a thick target. The weighting function in this case is the total Coulomb excitation probability which is independent of backscatter angle and dependent only upon the parameter ξ.

The total Coulomb excitation probability is proportional to the function $f_{E2}(\xi)$ which is simply the differential function

$$\frac{df_{E2}(\theta_p,\xi)}{d\Omega}$$

integrated over backscatter angle θ_p. Tables of values of the function $f_{E2}(\xi)$, calculated using the full quantum mechanical treatment, are available[Al]. Alder et al. have taken into account the energy loss of the ion and have developed the weighting function necessary to perform the thick target averaging. It is defined by

$$U_2(\nu,\zeta) = \frac{(1-\zeta)}{\zeta^{2.55}} f_{E2}(\nu,\zeta)$$

where the parameters ν and ζ are defined by

$$\zeta = \frac{\Delta E(1 + \frac{A_p}{A_T})}{E_i}$$

and

$$\nu = \frac{4}{Z_p Z_T}\left[\frac{10.008(1 + (\frac{A_p}{A_T})\Delta E}{A_p}\right]^{1/2} .$$

They are related to η_i and ξ by

$$\eta_i = \frac{2\zeta^{1/2}}{\nu} \quad \text{and} \quad \xi = \frac{2}{\nu}\zeta^{1/2}\left[\frac{1}{(1-\zeta)^{1/2}} - 1\right] .$$

Figure 3-2

Transient field and integrated transient rotation ϕ_w plotted as a function of ion recoil velocity for the cases of Rh ions recoiling in $Fe_{80}Rh_{20}$ alloy and Pt ions recoiling in $Fe_{85}Pt_{15}$. The actual curve of ϕ_w is the negative of the one shown in the diagram. The integrated transient rotation ϕ_w, for a given velocity, essentially represents the integral of the transient field curve from that velocity down to zero velocity. The transient field has been calculated from the Lindhard and Winther[L1] theory assuming $C_{ion} = 1$. Also shown is the quantity $\bar{\bar{\phi}}_w$, evaluated for the particular choices of projectile type and energy used in this thesis. $\bar{\bar{\phi}}_w$ is ϕ_w averaged over projectile scattering angle and energy. For interpreting this quantity, the velocity coordinate should be thought of as the maximum initial recoil velocity of a Coulomb-excited ion.

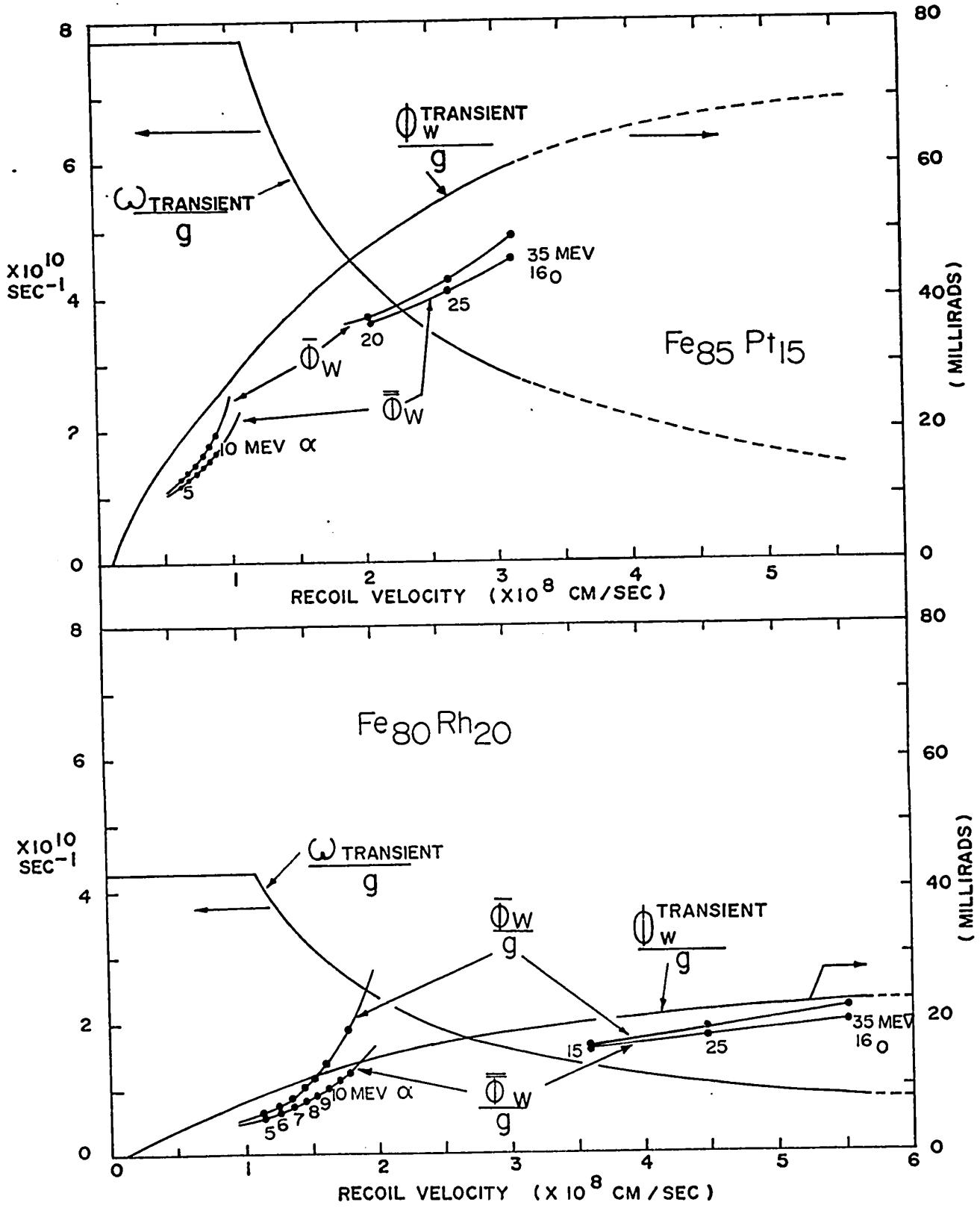
Fe85 Pt15
Fe80 Rh20
X10^10 SEC^-1
(MILLIRADS)
RECOIL VELOCITY (X10^8 CM/SEC)
ω TRANSIENT / g
Φ TRANSIENT W / g
Φ̄W
Φ̿W
35 MEV 16O
10 MEV α

Figure 3-2

The appropriate thick-target average is given by

$$\bar{\bar{W}}(135°,H,\infty) = \int_{\zeta_o}^{1} \bar{\bar{W}}(\nu,\zeta)U_2(\nu,\zeta)\frac{d\zeta}{\zeta} \Big/ \int_{\zeta_o}^{1} U_2(\nu,\zeta)\frac{d\zeta}{\zeta}$$

$$= 1 - \bar{\bar{b}}_4 - 2\bar{\bar{b}}_2[\omega\tau + \frac{\overline{\overline{b_2\phi_w}}}{\bar{\bar{b}}_2}]$$

where ζ_o corresponds to initial projectile energy E_o, and $\bar{\bar{\phi}}_w \equiv \overline{\overline{b_2\phi_w}}/\bar{\bar{b}}_2$ is the thick-target transient rotation averaged over backscatter angle and ξ. The results have been calculated numerically and are plotted in Fig. 3-2 as a function of maximum initial recoil velocity v_r^i. The coefficients $\bar{\bar{b}}_2$ and $\bar{\bar{b}}_4$ are the angular distribution coefficients that would be measured for a thick-target singles experiment. These calculated coefficients are listed in Table 3-1.

(iii) Solid angle attenuation factors

The a_2 and a_4 coefficients are calculated on the basis of the assumption that the detectors are point detectors. The effect of averaging over finite detector size is to attenuate the angular distribution coefficients; calculations of the attenuation factors for a_2 and a_4 coefficients for Ge(Li) detectors have been published by Camp and van Lehn[C2]; the attenuation factors used in calculation of the b_2 coefficients were taken from these tables and the uncertainty in their value was believed to be less than .5 per cent.

TABLE 3-1 SUMMARY OF CALCULATED ANGULAR DISTRIBUTION COEFFICIENTS

Isotope	Level Energy (kev)	Spin Sequence	Projec- Tile	+ Energy (mev)	ξ	η	Q_2 c)	A_2	Thick target a_2	Q_4 c)	A_4	Thick target a_4	Thick Target b_2/b_0	Thick Target b_4/b_0
^{103}Rh a	357	$\frac{1}{2}-\frac{5}{2}-\frac{1}{2}$	^4He	5	.5000	12.7	.93	.2857	.821	.78	.3810	-.044	.151	-.008
				6	.3766	11.6	.93	.2857	.738	.78	.3810	-.023	.137	-.009
				7	.2968	10.8	.93	.2857	.636	.78	.3810	-.009	.125	-.001
				8	.2416	10.1	.93	.2857	.593	.78	.3810	+.0006	.114	+.0008
				9	.2017	9.5	.93	.2857	.534	.78	.3810	+.007	.103	+.002
			^{16}O	35	.2288	38.5	.93	.2857	.536	.78	.3810	+.003	.104	+.0006
^{104}Pd	555.5	0-2-0	^4He	6	.6156	11.9	.93	.3571	.883	.78	1.143	-.057	.204	-.033
				7	.4831	11.0	.93	.3571	.817	.78	1.143	-.039	.191	-.023
				8	.3921	10.3	.93	.3571	.755	.78	1.143	-.025	.187	-.014
^{108}Pd	433.9	0-2-0	^4He	6	.4720	11.9	.93	.3571	.803	.78	1.143	-.037	.188	-.022
				7	.3714	11.0	.93	.3571	.761	.78	1.143	-.021	.178	-.013
				8	.3020	10.3	.93	.3571	.667	.78	1.143	-.009	.158	-.006
^{110}Pd	373.8	0-2-0	^4He	6	.4030	11.9	.93	.3571	.754	.78	1.143	-.027	.178	-.016
				7	.3175	11.0	.93	.3571	.681	.78	1.143	-.013	.161	-.008
				8	.2584	10.3	.93	.3571	.614	.78	1.143	-.002	.145	-.001
^{194}Pt	328.5	0-2-0	^4He	7	.4632	18.6	.95	.3571	.790	.825	1.143	-.047	.173	-.021
			^{16}O	35	.3415	66.7	.93	.3571	.664	.78	1.143	-.017	.152	-.009
^{195}Pt b			^{12}C	20	.5064	57.3	.93	.3571	.779	.78	1.143	.000	.182	.000
	238.9		^4He	7	.3334	18.6	.95	.2857	.678	.825	.3810	.020	.128	- 003
			^{16}O	35	.2477	66.7	.93	.2857	.560	.78	.3810	-.001	.108	.000
^{196}Pt	355.5		^4He	7	.5027	18.6	.95	.3571	.808	.825	1.143	-.049	.176	-.024
			^{16}O	35	.3695	66.7	.93	.3571	.689	.78	1.143	-.021	.159	.012
^{198}Pt	408		^4He	7	.5803	18.6	.95	.3571	.853	.825	1.143	-.051	.186	-.031
			^{16}O	35	.4242	66.7	.93	.3571	.730	.78	1.143	-.029	.165	-.017

a,b) For calculation of b_2 coefficients for 295 kev level in ^{103}Rh and 211 kev level in ^{195}Pt refer to Table 5-2 .

c) Q_2 and Q_4 are finite solid-angle attenuation factors.

(iv) Multiple scattering

As the projectile slows down in the target material, it can suffer a small number of large-angle deflections which effectively change its direction of motion. The distribution of projectile directions due to multiple scattering has been worked out by several authors. The distribution is effectively Gaussian, and has the effect of attenuating the observed angular distribution. McGowan and Stelson[M3] have calculated the attenuation coefficients for protons on various targets and have demonstrated that the attenuation factor can be as large as 5% for protons; however, for heavier projectiles, like alpha particles, the angular spread is only 2 or 3 degrees, and the attenuation is negligible.

(v) Uncertainties in calculated quantities

The f_{E2} values tabulated in Alder et al.[Al] are the result of a full quantum mechanical calculation and are therefore probably accurate to better than one percent. The main error in the U_2 function arises from uncertainties in the value of m for the E^{-m} energy dependence of the stopping power; however, Alder indicates that the results for thick-target yields which are presented in the paper are rather insensitive to the assumed power law, and are likely accurate to 2%. It is assumed, therefore, that the uncertainties in the calculated b_2 coefficients due to thick target averaging are 2%.

Figure 2-1 presents the results of a comparison between the semi-classical and quantum-mechanical calculations of the

a_2^{E2} and a_4^{E2} parameters as a function of scattering angle θ_p. It is seen that, for a_2^{E2}, the two calculations agree to within 1-2% where the a_2^{E2} value is appreciable over most of the range of θ_p. Somewhat large discrepancies for the a_4^{E2} parameter are not serious because the value of the angle-averaged a_4^{E2} parameter is so much smaller than the a_2^{E2} parameter value. It is believed that the uncertainty in the angle-averaged value of a_2^{E2} due to the semi-classical, rather than full quantum-mechanical calculation of $a_2^{E2}(\theta_p)$, is less than 1%.

The largest uncertainty in the average over scattering angle arises from the semi-classical calculation of the differential f_{E2} function. Alder et al. do not provide an estimate of this error, except to say that it is likely to be larger than the error in the total f_{E2} function. A comparison with the full quantum mechanical calculation was carried out for two representative values of ξ; the discrepancy varied from approximately 6% at back angles to as much as 10% at some forward angles. However, the semi-classical values overestimate the true values at some angles and underestimate them at other angles, so the error in the average over scattering angles is probably much less than these values quoted for particular angles. The uncertainty in the b_2 coefficients due to this source is assumed to be 3%.

The overall uncertainty in the calculated b_2 coefficients was set equal to 5%.

CHAPTER IV

EXPERIMENTAL ARRANGEMENT

The basic components of the experiments were: (a) a beam of ions of MeV energy (b) a ferromagnetic alloy target, in the form of a thick (.2 mm) foil (c) an electromagnet producing a magnetic field of a few kilogauss for the purpose of aligning the domains in the ferromagnetic target (d) two Lithium-drifted Germanium detectors mounted at particular angles with respect to the incident beam direction to monitor the gamma-ray count rate at those angles (e) a switching circuit to reverse the magnetic field direction at regular time intervals in an attempt to minimize the effect of systematic drifts in the electronics (f) a data-handling system to record a singles gamma-ray spectrum for each detector for both field "up" and field "down" - four spectra in all.

A. ION BEAM

The beam of ions required for the experiments was produced by a model FN Tandem Van de Graaff Accelerator at McMaster University. This machine can attain a terminal voltage of 9 MV; the highest terminal voltage required for the various experiments is presented in Table 4-1.

The beam was steered and focussed onto the target

TABLE 4-1 SUMMARY OF RELEVANT ACCELERATOR BEAM PARAMETERS

Alloy	Projectile	Charge State	Terminal Voltage (MV)	Energy (mev)	Target Current (nA)	Duration of Run (Hours)	Indication of Data Rate (Detector: S.A. = .55, Eff. ∿ 7%, volume = 50 cc)
$Fe_{80}Rh_{20}$	$\alpha(^4He)$	2+	1.67	5	600	5.3	4×10^5 counts in 357 kev peak
	$\alpha(^4He)$	2+	2.00	6	150	5.75	4×10^5 counts in 357 kev peak
	$\alpha(^4He)$	2+	2.33	7	50	6.5	4×10^5 counts in 357 kev peak
	$\alpha(^4He)$	2+	2.67	8	70	4.0	4×10^5 counts in 357 kev peak
	$\alpha(^4He)$	2+	3.00	9	40	4.5	4×10^5 counts in 357 kev peak
	^{16}O	4+	7.00	35	75	11	1.8×10^5 counts/hour in 357 kev peak
$Fe_{70}Pd_{30}$	α	2+	2.00	6	550	13	3.1×10^4 counts/hour in 374 kev peak
(Enriched	α	2+	2.33	7	300	-	3.2×10^4 counts/hour in 556 kev peak
in ^{104}Pd)	α	2+	2.67	8	150	12	2.9×10^4 counts/hour in 374 kev peak
$Fe_{85}Pt_{15}$	α	2+	2.33	7	400	27.5[a]	2.4×10^4 counts/hour in 239 kev peak
	^{16}O	5+	5.83	35	40	19.3	2.5×10^4 counts/hour in 211 kev peak
	^{12}C	3+	5.00	20	100	-	1.8×10^4 counts/hour in 356 kev peak

a) Abnormally long run because $\frac{Q-1}{Q+1}$ was being monitored throughout run to check for radiation damage effects.

through two apertures, the first made of tantalum, the second of lead. Their diameters were 4.5 mm and 3 mm respectively, and their positions are indicated in Fig. 4-1.

B. TARGETS

The targets were alloys consisting of rhodium , palladium , platinum, dissolved in iron in concentrations of up to 50 atom per cent. Iron was used as the ferromagnetic solvent material because of its high internal magnetic field and because the metals of interest were soluble in iron over a wide range of concentrations.

Various methods were employed to produce the alloys. The $Fe_{80}Rh_{20}$ targets were produced at the Central Research Institute for Physics, Budapest, Hungary, by arc melting and were kindly provided by Dr. L. Keszthelyi.

The $\{^{\text{platinum}}_{\text{palladium}}\}$-iron alloys were produced at McMaster University using an NRC electron-gun and resistance-heating unit. The electron-gun proved ineffective for two reasons: its permanent magnet tended to scatter the iron powder or flakes in the target material, and the melted alloy solidified into a (usually hollow) sphere. The latter fact made the alloy difficult to roll into a flat sheet, particularly for a brittle alloy like PtFe.

To circumvent these problems, a method was devised for forcing the liquid alloy to solidify directly into the required pill-box shape. This method consisted of melting the powdered

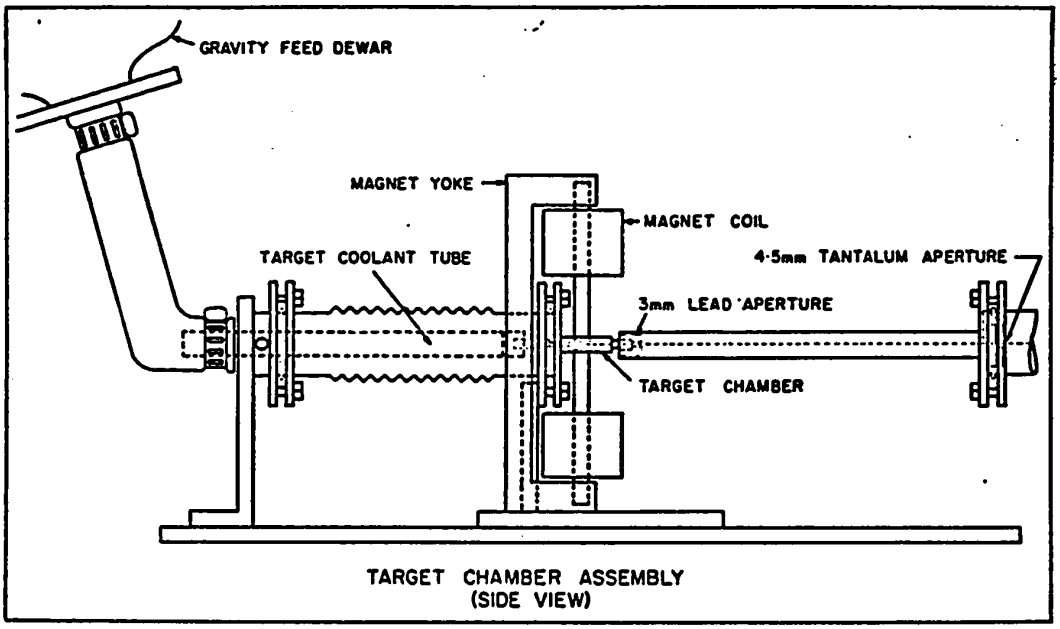

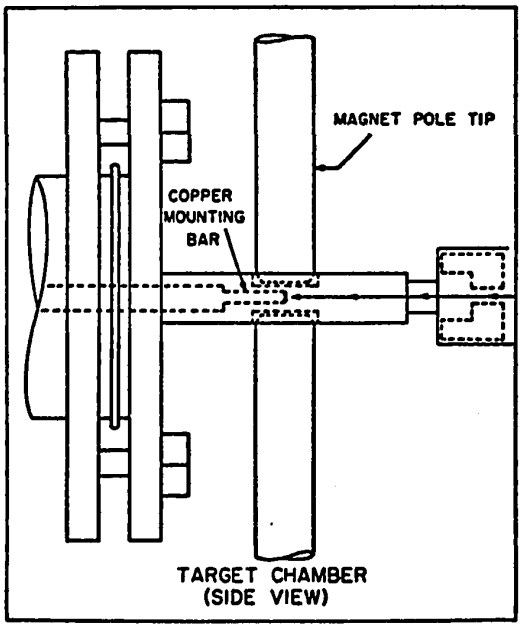

Fig. 4-1

Target Chamber
(Side view)

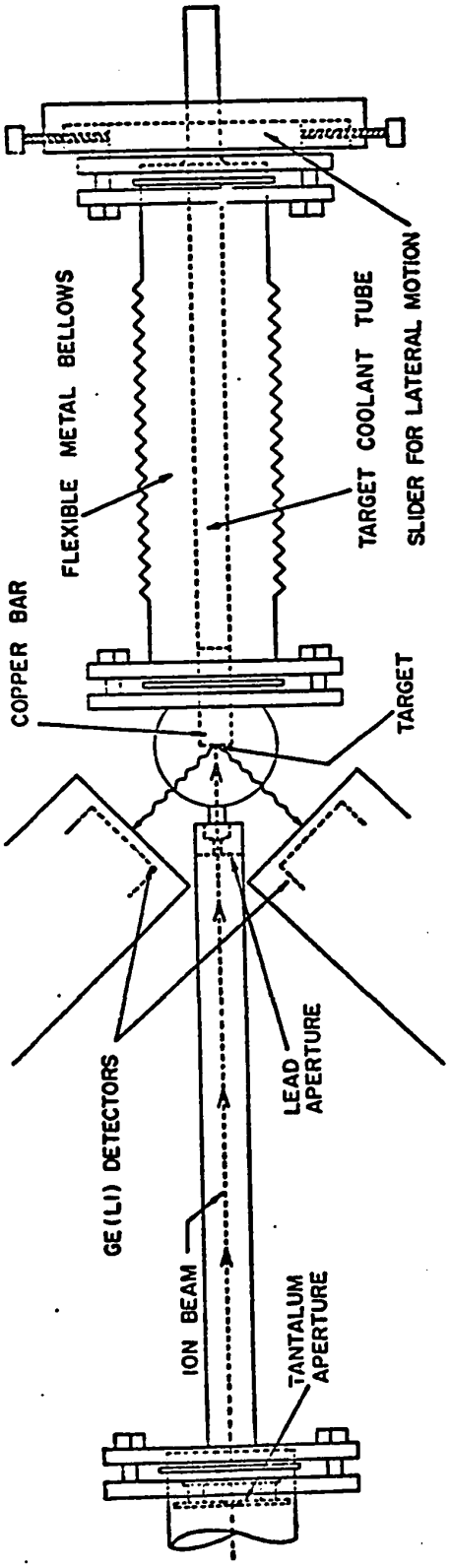

TARGET CHAMBER – TOP VIEW

Fig. 4-2

Target Chamber
(Top view)

materials in a mould fashioned of carbon; the mould featured a carbon plug that pushed down on the melted alloy and forced it to adopt the cylindrical shape of the melting chamber. Carbon was used as the mould material because it provided the high-resistance material that must be mounted between the electrodes of the resistance heating unit. A diagram of the arrangement can be found in Fig. 4.3. The length of the carbon plug was adjusted to suit the amount of target material used. The pill-box shaped solid alloy was then reduced to the desired shape (.2 mm thick×3mm high×4mm wide) by filing and by rubbing with emery cloth.

The targets were checked for magnetic saturation by measuring the magnetization as a function of external field at room temperature using a vibrating-sample magnetometer. Care was taken to provide the same target orientation relative to the external field as was used in the experiments. The (uncalibrated) magnetization curves are presented in Fig. 4-4; the operating points for the experiments are indicated as well as the approximate percentage of full room-temperature magnetization that was achieved. The possibility that the surface magnetization differs from the measured bulk magnetization is discussed in a later chapter.

The targets were soldered onto the front face of a rectangular copper bar with a cross-section of ∿3 mm×16 mm.

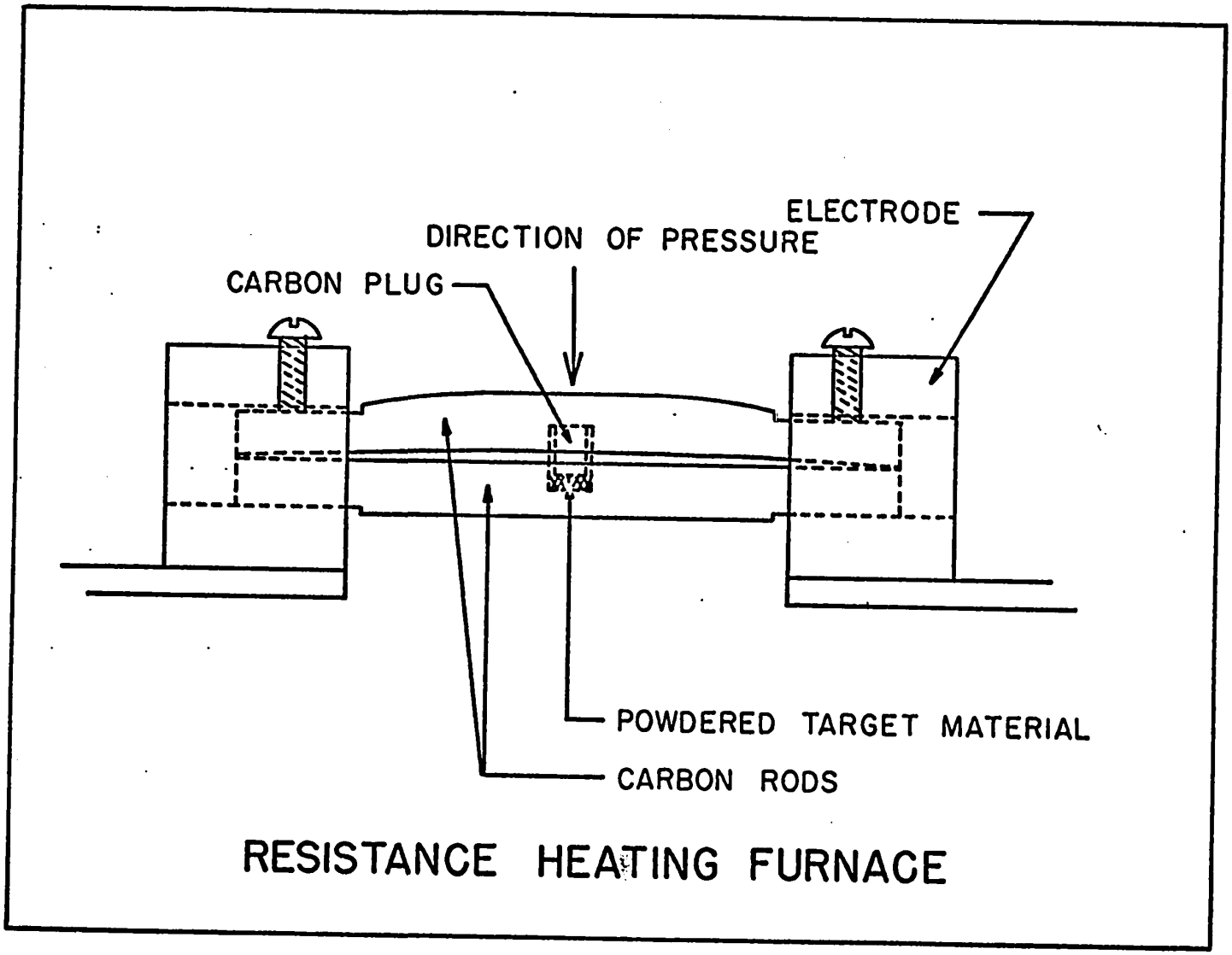

Fig. 4-3

Resistance-heating furnace

FIGURE 4-4

Bulk magnetization as a function of external applied field for $Fe_{80}Rh_{20}$, $Fe_{70}Pd_{30}$, and $Fe_{85}Pt_{15}$ alloys. Measurements were taken at room temperature using a vibrating-sample magnetometer, so the magnetization is expressed in arbitrary units and the three curves have been normalized at 7 kG external field for purposes of comparison. The external field used in the experiments reported in this thesis (3.2 kGauss) is indicated on the diagram .

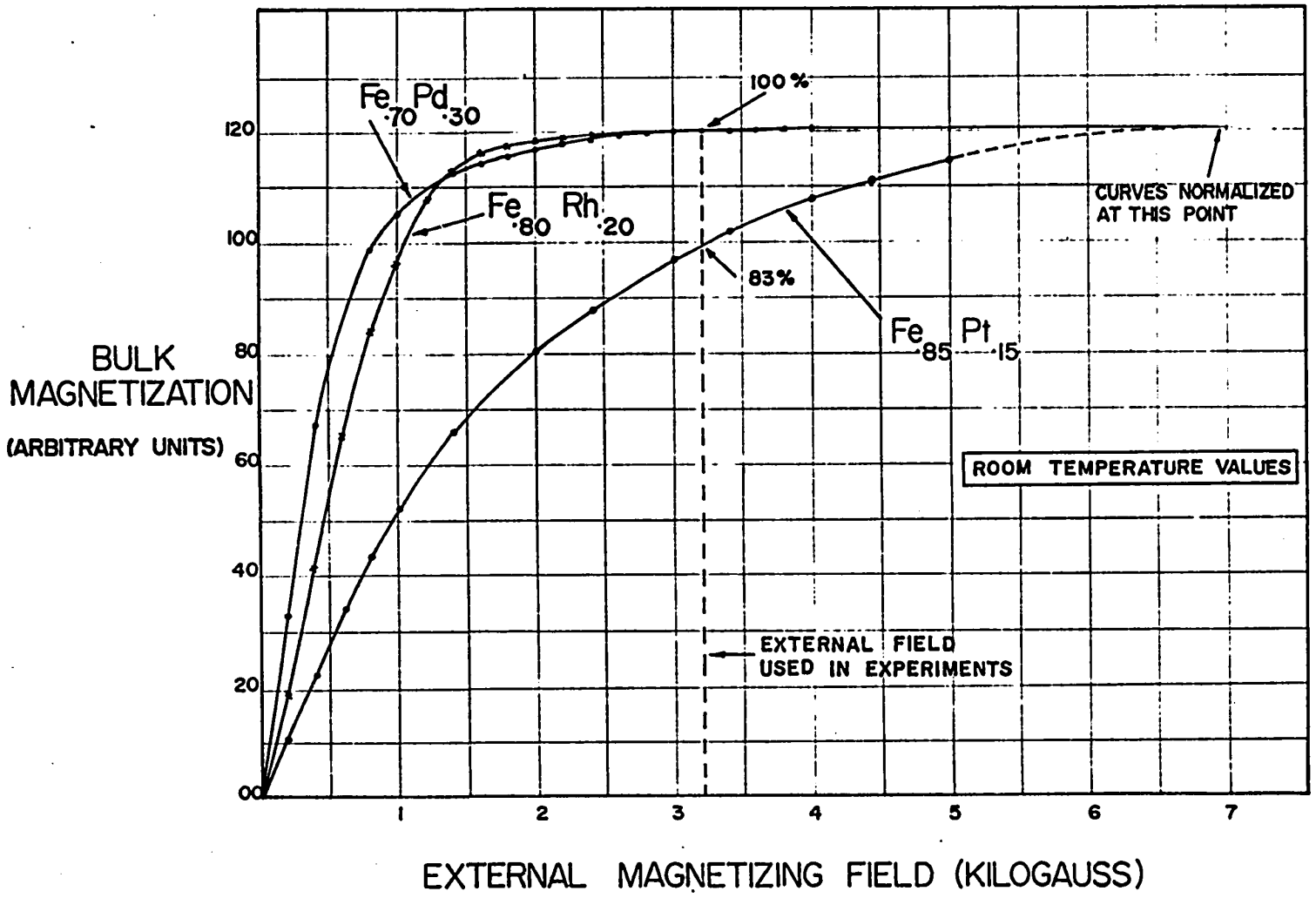
BULK MAGNETIZATION
(ARBITRARY UNITS)
120
100
80
60
40
20
00
1
2
3
4
5
6
7
Fe.70 Pd.30
100%
Fe.80 Rh.20
CURVES NORMALIZED AT THIS POINT
83%
Fe.85 Pt.15
ROOM TEMPERATURE VALUES
EXTERNAL FIELD USED IN EXPERIMENTS
EXTERNAL MAGNETIZING FIELD (KILOGAUSS)

Fig. 4-4

This bar fit snugly into a copper plug that was in direct contact with the target coolant. The distance from coolant to target was 3 cm. The size of the beam spot was $\sim$ 2 mm in diameter, and the highest power delivered by the beam was 3.5 watts for our experiments. Calculations showed that the power radiated to the copper bar from the walls of the target chamber was negligible by comparison. An estimate of the temperature difference $T_{target}-T_{coolant}$ was made. On the basis of these calculations, it is felt that $T_{target}-T_{coolant} \leq 50°C$ is a reasonable estimate for all of our experiments. The two coolants used were room-temperature water and liquid nitrogen. Thus

for R.T. water coolant $293°K < T_{target} < 343°K$

for liquid N_2 coolant $77°K < T_{target} < 127°K$.

C. ELECTROMAGNET

The electromagnet (Fig. 4-1) used to provide the external field consisted of two wire wound coils in series mounted on a C-shaped Armco iron yoke. The coils each contained 3200 turns of ASA number 20 insulated copper wire; the yoke was 1 inch square in cross-section and 12 inches high. The circular Armco-iron pole tips were 1/2 inch in diameter. With a pole-tip separation of 5 mm and a current in the coils of .8 amperes, a magnetic field of 3.2 kilogauss was produced at the centre of the pole-gap.

The profile of the transverse magnetic field as a function of radial distance from the centre of the pole gap

was measured using a Bell gaussmeter Hall probe. The Hall probe was calibrated against the analyzing magnet of the Tandem Accelerator, whose magnetic field is readily measured to high accuracy, using an in situ NMR probe. This field profile was necessary in order to calculate the effect of beam-bending (see Appendix 1) on our experiments.

D. FIELD-REVERSING ELECTRONICS

(i) Switch In an attempt to minimize the effect of systematic errors in count-rate due to short-term and randomly-occurring drifts in the electronics system it is desirable to interchange the roles of the two detectors at regular intervals during the experiment. This is most easily accomplished by reversing the external field direction (and thus the internal field direction in the target). The theory of such errors indicates that their effect can be minimized by making the counting time between field reversals as short as possible. Offsetting this requirement is the need for experimental efficiency which dictates that the counting interval ("on" interval) should be as large as possible compared to the field-reversing interval ("off" interval). The compromise chosen for our experiments was an "on" interval of 20 seconds and an "off" interval of .8 seconds.

Since a current of .8 amperes was used, it was necessary to have a switch which could reverse this current in less than .8 seconds. In the early experiments, a mechanical

relay was used; however, the reliability of its contacts deteriorated as time passed and it was superceded by an electronic switch (Fig. 4-5) which employed four power transistors, two of PNP type and two of NPN type. The direction of current flow was controlled by two logic levels (labelled FD1 or FD2 in Fig. 4-5) applied to the bases of the transistors.

(ii) Logic - Fig. (4-5)

A timer-scaler was used as a timer to count the 20 second intervals. Operated in master mode, it stopped counting and produced a logic pulse when 20 seconds had elapsed. This pulse was fed back to reset the timer/scaler to zero; it also fired a Schmidt trigger circuit, constructed of NAND gates. The fast logic output of this circuit was used to: (a) block the ADC inputs to prevent data accumulation during the switching interval, (b) change the status of the route logic level which controlled where the data was stored in the analyzer, (c) change the status of the logic levels FD1 and FD2 which control the field-reversing switch, thereby reversing the field direction and (d) fire a series of two monostable IC's which delivered a "restart" logic pulse after .8 seconds. The latter pulse was used to remove the blocking signal from the ADC's and to restart the timer/scaler.

SCHEMATIC DIAGRAM OF ELECTRONICS

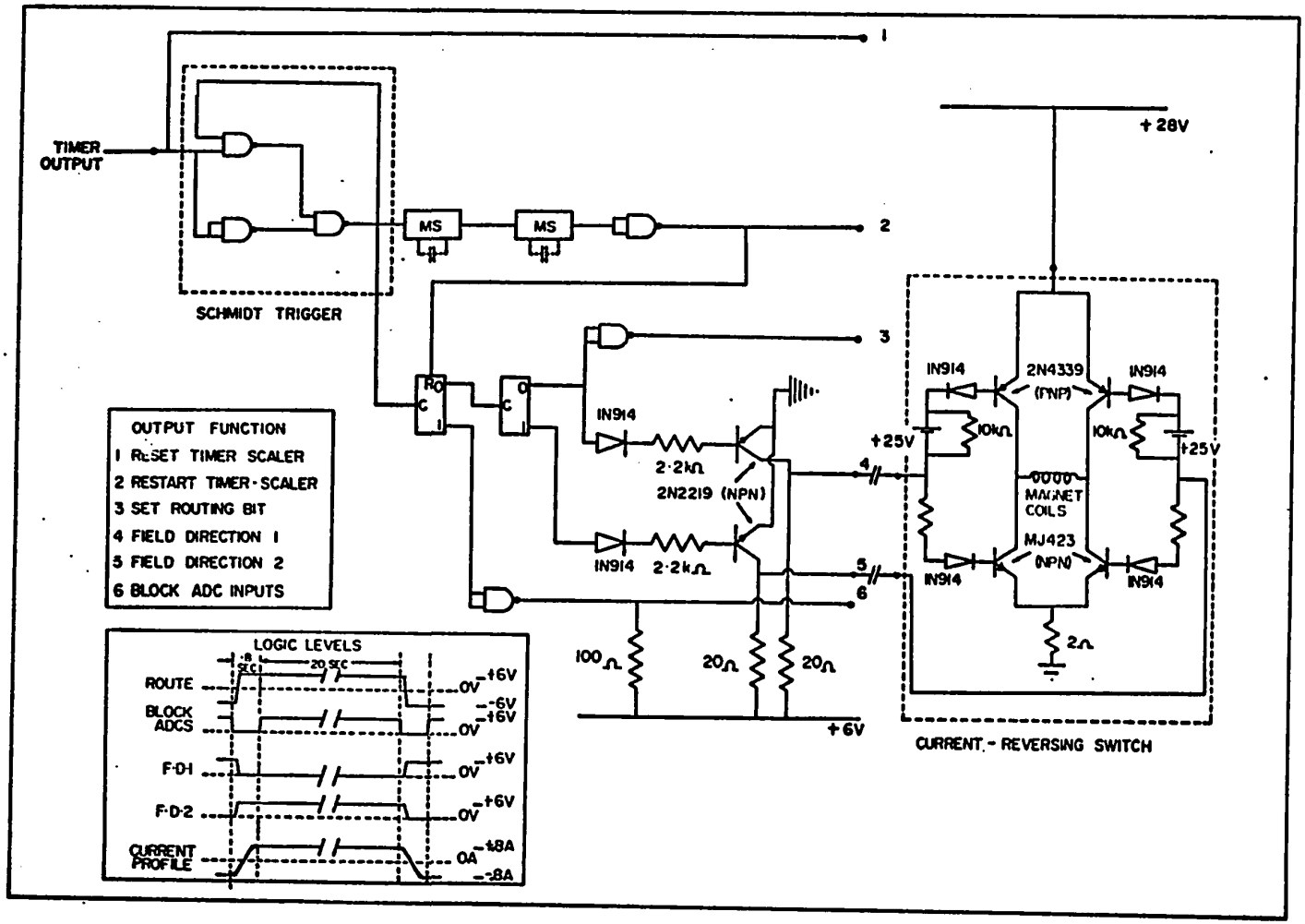

Fig. 4-5

E. ELECTRONICS FOR PULSE-HEIGHT ANALYSIS

A block diagram of the electronics is presented in Fig. 4-6. Two Ge(Li) detectors of large volume (40-50 cc) produced singles gamma-ray spectra which were analyzed and stored separately. A routing bit, whose status was changed during each "off" interval, permitted the spectra for magnetic field "up" and "down" to be stored separately. Four spectra, each 2048 channels in length, were therefore recorded - counter 1, field up and down, and counter 2, field up and down. The pulse-height analysis systems used were either a Nuclear Data 3300 Analyzer, or a PDP-9 digital computer programmed to act as an analyzer.

F. TARGET CHAMBER (Figs.4-1 and 4-2)

The target chamber was a thin-walled stainless-steel "pillbox" 2 inches in diameter and .375 inches high; the walls were of uniform 1 mm thickness. The copper bar on which the target was mounted protruded into the target chamber through a slot at the back end. The copper bar fitted into a copper plug which was mounted on the end of a 3/4 inch diameter stainless-steel tube. This tube permitted coolant (liquid N_2 or water) to be brought to a distance of 3 cm from the target. The stainless steel tube was about 10 inches long, and was

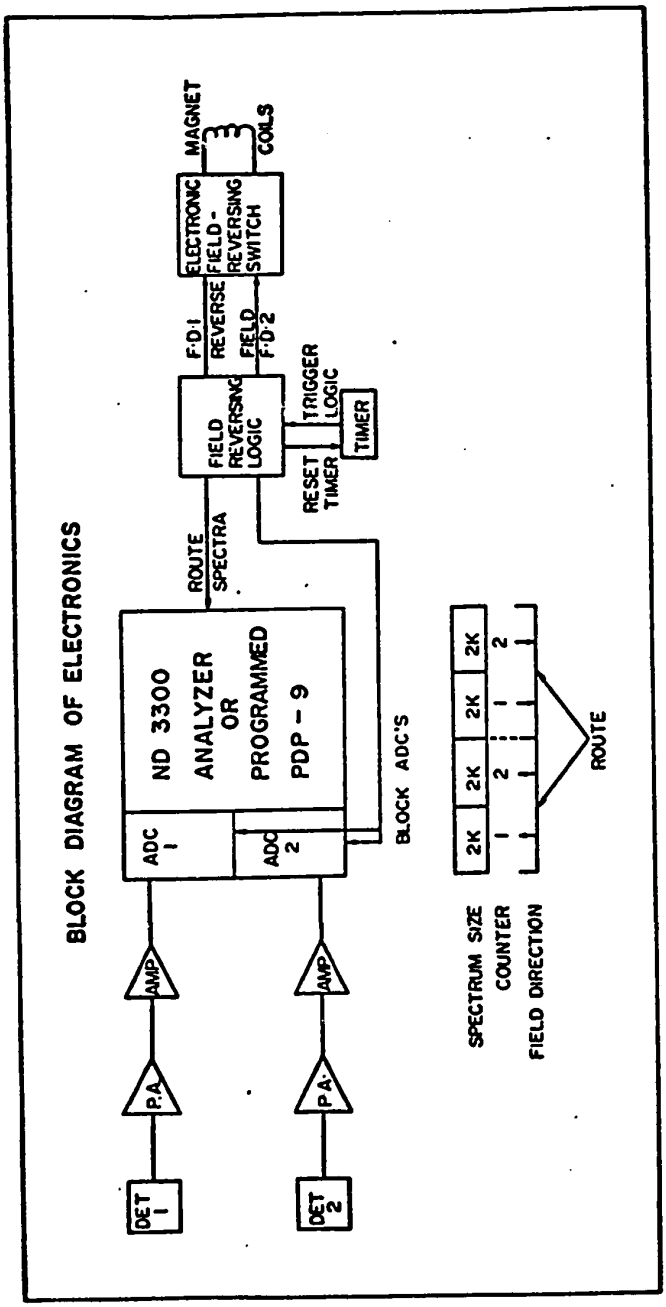
BLOCK DIAGRAM OF ELECTRONICS
DET 1
DET 2
P.A
AMP
ADC 1
ADC 2
ND 3300 ANALYZER OR PROGRAMMED PDP - 9
BLOCK ADC'S
ROUTE SPECTRA
FIELD REVERSING LOGIC
RESET TIMER
TRIGGER LOGIC
TIMER
F·D·1 REVERSE
FIELD F·D·2
ELECTRONIC FIELD-REVERSING SWITCH
MAGNET COILS
SPECTRUM SIZE
COUNTER
FIELD DIRECTION
2K
ROUTE

Fig. 4-6

located along the axis of a flexible metal bellows. The bellows served as a vacuum housing for the coolant tube; however, it also served another function. The coolant tube was welded to a metal blankoff which was in turn vacuum-sealed to the back end of the bellows by a Teflon seal. The target chamber itself was attached to the front end of the bellows by a similar arrangement. This front end was rigidly fixed in position; the back end of the bellows was mounted on a horizontal slider assembly. This feature permitted the coolant tube and target bar to be moved horizontally up to 1/2 inch with respect to the target chamber while the interior of the chamber and bellows was under vacuum. As a result, more than one target could be mounted on the copper bar and moved into the path of the beam as required without letting the chamber up to atmospheric pressure.

It proved necessary to modify the chamber by inserting "pole cups" so that the pole gap could be reduced to 5 mm and the magnetic field increased to 3.2 kG for the experiments on $Fe_{85}Pt_{15}$ alloy. Unfortunately, the pole cups under vacuum then bent inward and touched the copper bar. It was necessary to insert Teflon tape between bar and cup to provide electrical and thermal insulation. This prevented the copper bar from being moved under vacuum conditions, so the advantage was lost for the experiments on $Fe_{85}Pt_{15}$.

The target and cooling tube were electrically isolated from the chamber so that target current could be measured.

Current was also monitored on the two apertures mentioned in Section A to assist in steering and focussing the beam onto target.

CHAPTER V

DATA ANALYSIS AND EXPERIMENTAL RESULTS

This chapter begins with a development of the method of data analysis used to extract the rotation angle $\Delta\theta$. Then a treatment of possible sources of error such as (1) background subtractions in peak area calculations (2) beam bending and (3) indirect feeding of nuclear levels is presented. Some brief comments are made on particular problems of analysis associated with certain excited states. Finally the experimental results are presented.

A. RELATION BETWEEN ROTATION ANGLE AND MEASURED AREAS

The collected data consist of 4 singles gamma ray spectra for counter 1, field up and down, and counter 2, field up and down. Detector 1 is located at -135° and detector 2 at +135°. For a particular nuclear excited state, the quantity of interest in each spectrum is the number of counts collected at a particular excitation energy in the photopeak.

Let $N_1(+)$ = number of counts in detector 1 for field up at 135°

$N_1(-)$ = number of counts in detector 1 for field down at 135°

$N_2(+)$ = number of counts in detector 2 for field up at 135°

$N_2(-)$ = number of counts in detector 2 for field down at 135°.

The number of counts is proportional to the perturbed angular distribution at that angle, i.e.

$$N_1(+) = I_+ \cdot \varepsilon_1 \cdot (1-\bar{\bar{b}}_4+2\bar{\bar{b}}_2(\omega\tau+\bar{\bar{\phi}}_w)$$

where

$$\bar{\bar{\phi}}_w = \frac{\overline{\overline{b_2\phi_w}}}{\bar{\bar{b}}_2} .$$

I is the gamma ray intensity and is the same for both detectors for a given field direction; ε is the efficiency of the gamma ray detector (including the solid angle attenuation factor).

Changing the field direction simply changes the sign of $\omega\tau$ and $\bar{\bar{\phi}}_w$. Letting

$$\bar{\bar{W}}(+) = 1-\bar{\bar{b}}_4+2\bar{\bar{b}}_2(\omega\tau+\bar{\bar{\phi}}_w)$$

$$\bar{\bar{W}}(-) = 1-\bar{\bar{b}}_4-2\bar{\bar{b}}_2(\omega\tau+\bar{\bar{\phi}}_w)$$

we define

$$Q^2_{measured} \equiv \frac{N_1(+)}{N_1(-)} \cdot \frac{N_2(-)}{N_2(+)} = \frac{[I_+\varepsilon_1\bar{\bar{W}}(+)][I_-\varepsilon_2\bar{\bar{W}}(+)]}{[I_-\varepsilon_1\bar{\bar{W}}(-)][I_+\varepsilon_2\bar{\bar{W}}(-)]} = \frac{[\bar{\bar{W}}(+)]^2}{[\bar{\bar{W}}(-)]^2}$$

It can be seen that the advantage of combining the data in this particular way is that the beam intensity factors and detector efficiencies cancel out. Then

$$Q = (Q^2_{meas})^{1/2}$$

$$= \frac{\bar{\bar{W}}(+)}{\bar{\bar{W}}(-)}$$

and

$$\frac{Q-1}{Q+1} = \frac{2\bar{\bar{b}}_2(\omega\tau+\bar{\bar{\phi}}_w)}{1-\bar{\bar{b}}_4} .$$

A. GAMMA-RAY PEAK AREA ANALYSIS

A typical singles gamma ray spectrum is shown in Fig. 5-1.

As stated, the quantity of interest in a given singles spectrum is the number of counts for a particular excitation energy. The finite energy resolution of the detector and pulse-height analysis system means that the number of counts in the photopeak is distributed in a roughly Gaussian distribution over a number of analyzer channels. (Fig. 5-2). The peak is, of course, sitting on the inevitable background that arises mainly from Compton-scattered events from higher energy gamma rays. To find the peak area, it is necessary to estimate and subtract the number of counts in the background under the peak.

In a singles spectrum, this background subtraction can be a major source of error in the measured peak area; another source of error arises when the peak of interest and another peak close in energy are not resolved.

(i) Background Subtraction

While the background is not a linear function of channel number over a large segment of the spectrum, it varies slowly enough that the linear approximation is a good one over small regions. For the analysis, a linear background was assumed under each peak in most cases.

To estimate the background, a sample background window was set on either side of the peak; to make the linear approxi-

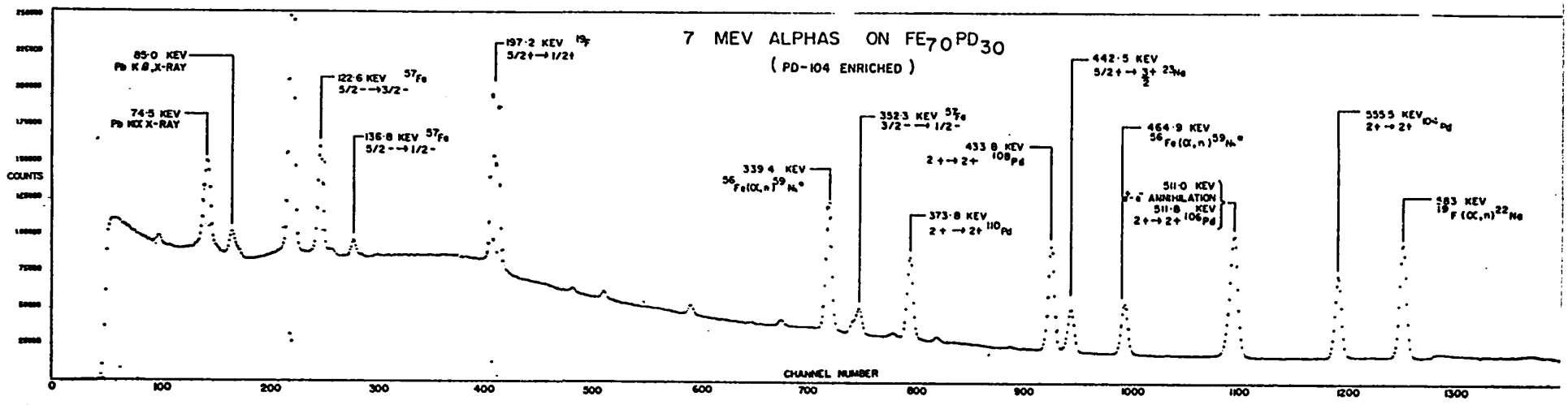
7 MEV ALPHAS ON FE70PD30
(PD-104 ENRICHED)
85·0 KEV
Pb K α,X-RAY
74·5 KEV
Pb Kα X-RAY
122·6 KEV 57Fe
5/2− → 3/2−
136·8 KEV 57Fe
5/2− → 1/2−
197·2 KEV 19F
5/2+ → 1/2+
339·4 KEV
56Fe(α,n)59Ni*
352·3 KEV 57Fe
3/2− → 1/2−
373·8 KEV
2+ → 2+ 110Pd
433·8 KEV
2+ → 2+ 108Pd
442·5 KEV
5/2+ → 3+/2 23Ne
464·9 KEV
56Fe(α,n)59Ni*
511·0 KEV
e+-e− ANNIHILATION
511·8 KEV
2+ → 2+ 106Pd
555·5 KEV 104Pd
2+ → 2+
583 KEV
19F(α,n)22Ne
COUNTS
CHANNEL NUMBER
0
100
200
300
400
500
600
700
800
900
1000
1100
1200
1300

Figure 5-1

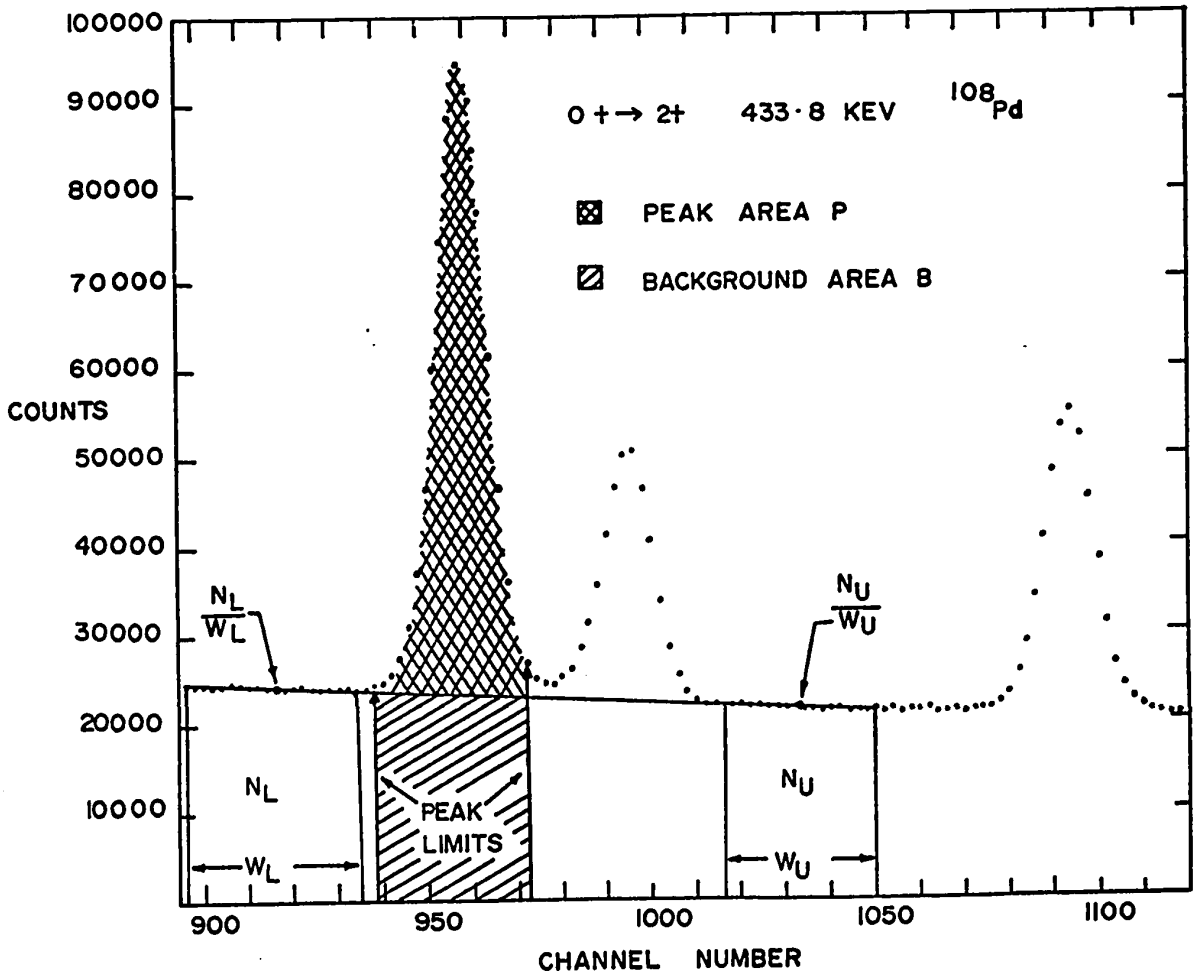
100000
90000
80000
70000
60000
COUNTS
50000
40000
30000
20000
10000
0+→ 2+ 433·8 KEV
108Pd
PEAK AREA P
BACKGROUND AREA B
NL/WL
NU/WU
NL
WL
PEAK LIMITS
NU
WU
900
950
1000
1050
1100
CHANNEL NUMBER

Figure 5-2

mation as valid as possible, the background windows were set as close as possible to the peak itself. As will be shown, the error in the background is usually reduced by making these background windows as wide as possible, all else being equal.

However, in many cases the rules regarding the proximity of the background windows to the peak and the width of these windows had to be modified due to the presence nearby of gamma ray peaks, dropped points, and Compton edges which disrupt the smoothly-varying background.

With reference to Fig.5-2, if the lower and upper background windows contain total numbers of counts N_L and N_U respectively, then the error in the background due to the finite width of the window is given by

$$(\Delta B)^2 = \left(\frac{C_1}{W_L}\right)^2 \left(\frac{N_L}{W_L}\right) + \left(\frac{C_2}{W_U}\right)^2 \left(\frac{N_U}{W_U}\right).$$

When the pure statistical errors in the measured quantities (P+B) and B are taken into account , it is found that the variance in the measured peak area P is given by

$$\Delta P = \left[(P+B)+B + \left(\frac{C_1}{W_L}\right)^2 \left(\frac{N_L}{W_L}\right) + \left(\frac{C_2}{W_U}\right)^2 \left(\frac{N_U}{W_U}\right)\right]^{1/2}$$

The last two terms describe how the choice of background windows increases the error in the measured peak area. The minimum error, for infinitely-wide background windows, is still $[P+B)+B]^{1/2}$.

The effect of the last two terms on the relative error in P was investigated as a function of the width of the background windows. The experiments were of sufficient duration that almost all of the peaks of interest contained > 2×10^5 counts. It was found that, for the experiments involving alpha particles as projectile (P/B $\gtrsim$ 2:3), the relative error in peak area was not appreciably affected (<1%) by the choice of window width, even for the poor statistics ($\sim 1.5 \times 10^4$ counts) of the 408 keV level in ^{198}Pt. For the experiments using ^{12}C and ^{16}O as projectiles (P/B $\gtrsim$ 1:5), the higher background required that the window width be no smaller than three channels in order to make the effect of the window width unimportant in a relative sense (< 1%). For the statistically poor 408 keV peak in ^{198}Pt, the windows could not be more than 4-5 channels wide in practice; this increased the relative error in P by $\sim$ 3.5% for this peak.

(ii) Unresolved Doublets

The energy resolution of the Ge(Li) detectors and amplifying system employed was 2.0 to 2.5 keV at low count rate; under actual high count rate conditions, the system resolution was $\sim$ 2.7 to 3.5 kev.

In some cases, the peak of interest was so close to a neighbouring peak that the two peaks were not completely resolved. In this case, one has the choice of a variety of methods for extracting the area of the peak of interest.

One method attempted was the fitting of the multiplets

by trial functions (skewed Gaussians); a non-linear least-squares fit was performed using the peak height, width, position and skewness as parameters.

It was found that under the high count rate conditions of the experiments, the peak shape varied considerably from one experimental period to the next; this variable peak shape was caused mainly by adjustments in the amplifying electronics (e.g. pole-zero adjustment) which were not reproducible in successive experiments. It was not possible to find a sufficiently general trial function which would provide good fits to doublets in all of the experimental spectra. For this reason, the fitting procedure was abandoned.

One method that was employed when the uninteresting member of the doublet was a reasonably small fraction of the interesting member was simply to treat the doublet as a single peak. Provided that the background peak is a small fraction of the peak of interest, the ratio of counts for field up and field down can be quite insensitive to the systematic over-estimate of each peak area. This error in $\omega\tau$ is even less if the same target and same method of analysis are used to measure the b_2 coefficient. The validity of this method had to be judged for individual cases. In cases where the two peaks were poorly resolved, one had no choice but to treat the data by this method.

Another method, employed where the peaks were reasonably well-resolved and the statistics in the peak of interest were good, was to set the peak limits so as to exclude from con-

sideration that part of the interesting peak which is likely to contain overlap with the uninteresting peak, and then to analyze the peak of interest as a singlet. This method was employed whenever possible.

Beam Bending

As the charged projectile ion enters the fringing field of the electromagnet, it is bent in a curved path in the horizontal plane. This bending of the beam not only causes a shift in the location at which it strikes the target (beam shift), but also alters the angle at which it strikes the target (beam rotation). The changes in count-rate caused by these effects can be comparable to the change in count rate caused by the perturbation of the angular distribution; it is, therefore, important to correct for the effect of beam-bending. A detailed analysis of beam-bending corrections for singles experiments is presented in Appendix 1, and the calculated corrections to the measured quantity $\frac{Q-1}{Q+1}$ are recorded in Table 5-1. The beam-bending calculations were checked by a measurement of $\frac{Q-1}{Q+1}$ for levels in ^{55}Fe excited in the reaction $^{52}Cr(\alpha,n)^{55}Fe$; They agreed with the measured values within experimental error. It is worthy of note that the calculation achieved considerably better accuracy than the experimental measurement of beam-bending. It is also noteworthy that the experimental measurement of the beam-bending effect requires at least two states with widely-separated b_2 coefficients in their angular distribution

TABLE 5-1 Summary of Beam-Bending Corrections

$$\left(\frac{Q-1}{Q+1}\right)\times 10^3 = (6.39-43.9\ b_2)\ \frac{Zi}{\sqrt{AE}}$$

Z = projectile charge state E = projectile energy

A = projectile mass number i = magnet current (amperes)

Projectile	Energy (Mev)	Charge State	Target Species	ΔE (kev)	b_2	$\left(\frac{Q-1}{Q+1}\right)\times 10^3$ B.b a)
Alpha	5	2+	103 RH	295	-.215	+5.7
	6				-.187	+4.8
	7				-.165	+4.1
	8				-.146	+3.6
	9				-.131	+3.4
Alpha	5	2+	103 RH	357	+.151	-0.08
	6				+.137	-0.12
	7				+.125	+0.27
	8				+.114	+0.40
	9				+.103	+0.50
^{16}O	35	4+	103 RH	295	-.131	+1.6
	35	4+	103 RH	357	+.104	-0.3
Alpha	6	2+	104 PD	556	+.209	-0.6
	7				+.191	-0.4
	8				+.187	-0.3
	6	2+	108 PD	434	+.188	- .8
	7				+.178	- .5
	8				+.158	- .3
	6	2+	110 PD	374	+.178	- .4
	7				+.161	-.15
	8				+.149	-.02
Alpha	7	2+	195 PT	211	+.0405	+1.4
			195 PT	239	+.128	+0.2
			194 PT	329	+.173	-0.4
			196 PT	356	+.176	-0.4
			198 PT	408	+.186	+0.5
^{16}O	35	5+	195 PT	211	+.0345	+0.8
			195 PT	239	+.108	+0.3
			194 PT	329	+.152	-0.06
			196 PT	356	+.159	-0.1
			198 PT	408	+.165	-0.2
^{12}C	20	3+	194 PT	329	+.182	-0.3

a) Beam-bending corrections are opposite in sign to the values in this column.

(preferably one positive and one negative), because the size of the effect is a function of the b_2 coefficient.

Indirect Feeding of Nuclear Level

While most of the Coulomb excitation of a nuclear state occurs directly via E2 excitation, part of the contribution to the population of the state can come from Coulomb-excited states of higher energy which gamma-decay to the state of interest. Since the indirect feeding of the level involves an intermediate gamma ray, the angular distribution for the gamma rays created by indirect feeding can be considerably different than for those created by direct Coulomb excitation. In addition, if the mean life of the upper state is long compared to the lower one, the mean life of the indirect process is essentially determined by the upper state's mean life. The theory of the effect of indirect feeding on the observed rotation angle $\omega\tau$ and on the effective mean life $\tau_{eff.}$ is presented in detail in Appendix B. Indirect feeding was found to be important in the case of the 295 keV $3/2^-$ level in ^{103}Rh and the 211 keV $3/2^-$ level in ^{195}Pt due to the existence of the 357 keV $5/2^-$ level in ^{103}Rh and the 239 keV $5/2^-$ level in ^{195}Pt.

Following the convention of Appendix B, the upper level is level A and the lower level is level B.

As discussed in the Appendix, the angular distribution coefficients for level B are linear combinations of the coefficients that are appropriate for direct excitation of level A

and level B. Similarly, the effect of indirect feeding on the observed rotation angle for a perturbed angular distribution may be summarized by saying that the observed static and transient rotations for the lower state (B) correspond to linear combinations of the static and transient rotations for both the upper (A) and lower (B) states. If indirect feeding were not important, one could separate static and transient effects by plotting $\frac{\Delta\theta}{g} = (\frac{\omega}{g})\tau + (\frac{\phi}{g})$ for two or more states as a function of mean life τ. However, when a nuclear level is subject to indirect feeding, to consider the observed rotation for that particular level to have this form one must choose between two possibilities. The first option is to use the measured rotation angle for state (A) to correct the rotation angle for state (B) for the influence of state (A). The second option requires one to absorb the average static rotation $\omega_A\tau_A$ by expressing this rotation in terms of the static rotation $\omega_B\tau_B$, and, as a consequence, to define an effective mean life for state (B) that contains an explicit dependence on the ratio of g factors (g_A/g_B). The approach that is preferable must be decided for each case of interest. A full sample calculation for the case of ^{103}Rh is presented in Appendix B. The results for the case of the 295 keV level in ^{103}Rh and the 211 keV level in ^{195}Pt are presented in Table 5-2. For both of these levels, it can be seen that the indirect feeding effect is by no means negligible.

TABLE 5-2 SUMMARY OF INDIRECT FEEDING CALCULATIONS FOR ^{103}Rh AND ^{195}Pt

103 RH	Mixing Ratio δ [a]	$A_2^{(2)}$	U_2	$F_2(I_A I_B,2,2)$	$A_2'=A_2^{(2)}\times U_2\times F_2$	A_4'
B≡295 kev	.183(.010) [b]	.7743	1	.5000	-.3872	0. (A_4=0)
A≡357 kev	∞	.7743	.7483	-.5345	-.3097	0. (U_4=0)
195 PT						
B≡211 kev	-.38(2) [c]	-.2013	1	-.5000	+.1006	0. (A_4=0)
A≡239 kev	∞	-.2013	.7483	-.5345	+.0805	0. (U_4=0)

103 RH		a_2^{thick}	$Q_2\times A_2'\times a_2$ (Q_2 = .93)	$(\bar{b}_2/\bar{b}_0)=(.75\ Q_2 a_2 A_2')/(1+.25 Q_2 a_2 A_2')$ d ≡ direct i ≡ indirect
9 Mev α	295 kev	.469	-.169	-.133 d
	357 kev	.534	-.154	-.120 i
8 Mev α	295 kev	.525	-.189	-.149 d
	357 kev	.593	-.171	-.134 i
7 Mev α	295 kev	.593	-.213	-.169 d
	357 kev	.656	-.189	-.149 i
6 Mev α	295 kev	.668	-.240	-.192 d
	357 kev	.738	-.212	-.168 i

TABLE 5-2 (CONTINUED)

		a_2^{thick}	$Q_2 \times A_2' \times a_2$ (Q_2 = .93)	$(\bar{b}_2/\bar{b}_0)=(.75\ Q_2 a_2 A_2')/(1+.25 Q_2 a_2 A_2')$ d ≡ direct i ≡ indirect
5 Mev α	295 kev	.755	-.272	-.219 d
	357 kev	.821	-.236	-.188 i
35 Mev ^{16}O	295 kev	.477	-.172	-.134 d
	357 kev	.536	-.154	-.120 i
195 PT				
.7 Mev α (Q_2=.95)	211 keV	.637	+.0597	+.0441 d
	239 kev	.678	+.0508	+.0377 i
35 Mev ^{16}O	211 kev	.520	+.0487	+.0360 d
	239 kev	.560	+.0451	+.0334 i

	$B(E2)$ $e^2 barn^2$	Ratio (1)	(2) $\frac{I^{total}_{cascade}}{I^{total}_{crossover}}$	(1)×(2) = P
103 RH				
A≡357	.392(27)[d]	1.83(18)	.154(10)[e]	.283(34)
B≡295	.223(15)*			
195 PT				
A≡239	.67 (3)[c]	1.52(10)	.953(58)[c]	1.45(13)
B≡211	.44 (2)			

(continued next page)

TABLE 5-2 (CONTINUED)

		R = Ratio of Thick Target Yields (A/B)	S = R×(P)	$\beta = \frac{s}{1+s}$	$\alpha = \frac{1}{1+s}$
103 RH	5 Mev α	.617	.175	.148	.852
	6 Mev α	.684	.194	.1625	.838
	7 Mev α	.756	.214	.176	.824
	8 Mev α	.811	.229	.186	.814
	9 Mev α	.868	.245	.197	.803
	10 Mev α	.885	.250	.200	.800
	35 Mev ^{16}O	.850	.240	.193	.807
195 PT	7 Mev α	.858	1.25	.555	.445
	35 Mev ^{16}O	.890	1.29	.563	.437

(continued next page)

TABLE 5-2 (continued)

	Projectile	α	$\frac{\bar{b}_2^d}{\bar{b}_0^d}$	β	$\frac{\bar{b}_2^i}{\bar{b}_0^i}$	$\bar{b}_2^m = \alpha\frac{\bar{b}_2^d}{\bar{b}_0^d} + \beta\frac{\bar{b}_2^i}{\bar{b}_0^i}$	$C = \frac{\beta}{\bar{b}_2^m}\frac{\bar{b}_2^i}{\bar{b}_-^i}$	$(\Delta\theta_B^{corr} = \Delta\theta_B^{meas} - C\Delta\theta_A^{meas})$
103 RH	5 Mev α	.852	-.219	.148	-.188		-.215	+.129
	6 Mev α	.838	-.192	.163	-.168		-.187	+.146
	7 Mev α	.824	-.169	.176	-.149		-.165	+.159
	8 Mev α	.814	-.149	.186	-.134		-.146	+.171
	9 Mev α	.803	-.133	.197	-.120		-.131	+.180
	35 Mev ^{16}O	.807	-.134	.193	-.120		-.131	+.177
195 PT	7 Mev α	.445	+.044	1.555	+.0377		+.0405	+.516
	35 Mev ^{16}O	.437	+.036	0.563	+.0334		+.0345	+.545

*Corrected to be consistent with cascade/crossover ratio of Grunditz et al[e] used in this thesis

a) Brink-Rose definition b) G1 c) N1 d) S6 e) G3 f) N1 g) N1

E. SEPARATION OF STATIC AND TRANSIENT EFFECTS

The approach used in the data analysis is based upon the basic assumption that the transient field acts only during the time that the recoiling ion is slowing down and can be considered as an impulsive rotation; the observed rotation angle is therefore assumed to have the form $\Delta\theta = \omega\tau + \bar{\bar{\phi}}_w$, where $\bar{\bar{\phi}}_w$ is the transient contribution, τ is the mean life of the state, and $\omega\tau$ is the average static rotation. If the g factors of all states studied for a given element were the same, then the ω value and $\bar{\bar{\phi}}_w$ value for each state would be the same; the measured rotation angles, $\Delta\theta$, plotted vs mean life for these states, would lie on a straight line of slope ω and intercept $\bar{\bar{\phi}}_w$. If all of the states are 2+ states of vibrational character in even-even nuclei, the assumption of equal g factors may be justifiable; however, even in this case g factors of 2+ states measured by radioactivity indicate that the g-factors can be different. If odd-A nuclei are involved, it can certainly not be assumed that all g-factors are equal. If the g-factors of all of the states are known by measurement from independent experiments, the static and transient contributions can be extracted by plotting $\frac{\Delta\theta}{g}$ vs τ; the data points will define a straight line of slope $\frac{\omega}{g}$ and intercept $\frac{\phi}{g}$. The reader will recall that these quantities correspond to $\frac{\mu_N}{\hbar} H_{\text{static}}^{\text{average}}$ and $\frac{\overline{b_2\phi_w}}{\bar{b}_2 g}$ respectively, where

$$\frac{\phi_w}{g} = \frac{\mu_N}{\hbar} \int_0^{t_s} H_{\text{transient}}(t) e^{-t/\tau} \frac{dt}{\tau}$$

F. METALLURGICAL CONSIDERATIONS

Several criteria were applied in choosing the elements to be alloyed with iron. First, the element had to be soluble in iron over a reasonable range of concentrations. Second, to optimize the experimental data rate, the concentration of solute was to be as large as possible compatible with the requirement that the resultant alloy be ferromagnetic and almost fully magnetizable in moderate external fields. These metallurgical restrictions, combined with nuclear considerations, severely limit the number of candidates for study. Rhodium, palladium and platinum were three metals that satisfied the criteria. The magnetization curves of Figure 4-4 indicate the degree of full room temperature bulk magnetization achieved for each alloy used in the experiments.

G. CHOICE OF TARGET COOLANTS

The experiments on $Fe_{80}Rh_{20}$ and $Fe_{70}Pd_{30}$ alloy were performed with both water cooling and liquid nitrogen cooling of the target. This was done to investigate whether the experimental results depended upon target temperature. Two possible causes of such a temperature dependence are: (1) beam heating of the target, which, for water cooling, might destroy some of the ferromagnetism by raising the local temperature in the target near or above the Curie temperature of the alloy, and (2) for liquid nitrogen cooling, a decrease in the rate of annealing of radiation damage due to the fact that vacancy mobility is inhibited below room temperature. The first effect

could lower the average observed static field for the water-cooled target while the second effect could reduce the average observed static field for the liquid nitrogen cooled target. If the experimental results are the same within error for both target coolants, one could conclude that neither of the above mechanisms affect the measured quantities in a significant way.

H. CHOICE OF PROJECTILE AND ENERGY

The reader will recall that V_p is the velocity at which Lindhard and Winther's transient field changes from a $\frac{1}{v}$ dependence (above V_p) to a constant value (below V_p). In view of theoretical difficulties in calculating V_p, it is treated in the theory as an empirical parameter. Perhaps the most intuitive estimate of V_p would be $V_p = V_o \equiv \frac{c}{137}$ because the ion velocity then equals the orbital 3d electron velocity in iron, and according to Bohr's treatment of ionic energy loss, at this velocity, the probabilities of pickup and loss of 3d electrons become equal. Below this velocity, the average number of 3d electrons is most likely to remain constant, and equal to the number appropriate to a nonionized atom. So one might expect that any change in the velocity dependence of the transient field would occur at $V_p = V_o$. The experimental results accumulated to date, mainly from IMPACT experiments are, in general, approximately a factor of 2 larger than the theoretical predictions and one can obtain better agreement with experiment by assuming that $V_p = \frac{V_o}{2}$.

For our experiments, alpha particles were chosen as projectiles in conjunction with target atoms of mass number $A \sim 100$ because the range of 5 to 9 Mev alpha particle energy was just right for varying the maximum initial recoil velocity of target atoms through the velocity $\frac{V_o}{2} = 1.1 \times 10^8$ cm/sec. This seemed the most likely velocity region for observing any sudden changes in transient field behaviour. Below 5 Mev alpha energy, the Coulomb excitation cross-section became prohibitively low; above 9 Mev alpha energy, one is near the top or over the Coulomb barrier for light impurities and the background from nuclear reactions makes the peak-to-background ratio poor.

At or above 10 Mev, perhaps the most serious difficulty for alloys rich in iron is the predominance of lines in the spectrum from the reaction $^{56}Fe(\alpha,n)^{59}Ni^*$. In particular, the Coulomb excitation lines are dominated by a very strong 339 kev line; this is the first excited state in ^{59}Ni. At 10 Mev and above, if the count rate is kept at a level that preserves a reasonable dead time (< 50%) in the pulse-height analysis system and reasonable detector resolution, then the counting rate in the Coulomb excitation lines is very poor. A further drawback at or above 10 mev alpha energy is neutron damage to the Ge(Li) detectors caused by neutrons from the reaction quoted above.

The experiments employing ^{16}O projectiles were performed using $Fe_{80}Rh_{20}$ and $Fe_{85}Pt_{15}$ alloy targets to provide points of contact with IMPACT experiments, and to provide recoil velocity

coordinates far in excess of the value $\frac{V_o}{2}$. The experiment employing 20 Mev ^{12}C on the $Fe_{85}Pt_{15}$ target was intended to provide a maximum initial recoil velocity coordinate intermediate between the coordinates for 7 mev alpha ($V_{recoil} < \frac{V_o}{2}$) and 35 mev ^{16}O ($V_{recoil} >> \frac{V_o}{2}$) projectiles. For Pt, ^{7}Li is the required projectile for varying the Pt recoil velocity through the value $\frac{V_o}{2}$. However, an experiment with 15 Mev ^{7}Li projectiles was attempted and aborted due to the very high level of background and consequent low counting rate in the Coulomb excited peaks of interest.

I. $\underline{Fe_{80}Rh_{20}}$ ALLOY

Apart from metallurgical considerations, rhodium was chosen for study because:

(1) it is monoisotopic and has two states, ($J\pi$ = 3/2-, ΔE = 295 kev) and ($J\pi$ = 5/2-, ΔE = 357 keV) which are readily Coulomb excited,

(2) one state is short-lived (295 kev, τ = 10.4 psec) and one is relatively long-lived (357 kev, τ = 86.3 psec). Since the average static rotation for the short-lived state is small, this state should be most sensitive to transient field effects, while the long-lived state should have a large static field component. This is convenient for separating "static" from "transient" field effects.

As the study proceeded, it became apparent that the indirect feeding of the 295 kev state from the 357 kev state was a significant factor.

It was decided to correct for the influence of state A by subtracting the measured rotation for state A from the measured rotation for state B, following the procedure outlined in Appendix B. The results are listed in Table 5-3 and are plotted in Figure 5-3.

There have been several measurements of the g-factors of the 295 kev and 357 kev states[B6,R1,S4]; these authors have assumed that the effect of indirect feeding on the measured rotation angle of the 295 kev state is negligible. The only work[S5] which does account for indirect feeding uses the singles technique, bombarding a $Fe_{97}Rh_3$ target with 5 Mev protons; the results reported herein agree with the numbers reported in this paper which indicate that most of the observed rotation for the 295 kev state is due to the indirect feeding component. When corrected for indirect feeding, the net rotation angle of the 295 kev state is small and the uncertainty in its value is increased due to the uncertainty in the size of the indirect feeding component. As a result, the g factor reported for this state in reference S5 has a 57% uncertainty (g_{295} = .28(16), g_{357} = .54(3)). The analysis that produced these numbers assumed that the transient field contribution was negligible for 5 Mev proton bombardment.

All authors agree that the g factors of the two states are far from equal. It is therefore necessary to analyze the data by plotting $\frac{\Delta\theta}{g}$ vs τ. The g factor of the 357 kev state

was taken to be .54(3), and its mean life τ = 86.3(3.6) psec from the average of B(E2) values measured by Coulomb excitation[M4,B8,S6]. The mean life of the 295 kev state was taken to be 10.4±.6 psec[G1]. In view of the large uncertainty in the g factor of the 295 kev state arising from the correction for indirect feeding, it was felt that the fairest way to analyze the data was by treating g_{295} as a parameter to be varied between the quoted limits on its value (.12 to .48). The data were analyzed in this way and are plotted in Figures 5-4 and 5-5 for 4 different values of g_{295} (g = .20, .28, .36, .44). For g = .12, the error bars on the extracted quantities became so large that the data were meaningless. In analyzing the data, the values g = .54, τ_{357} = 86.3, τ_{295} = 10.4 were used, and no error was assumed in these quantities. This procedure is justifiable because one is interested in the slope and intercept as a function of projectile energy; as long as one uses the same values for these quantities for all projectile energies, any error incurred by the particular values chosen for these quantities will be a systematic one. With reference to Figures 5-4 and 5-5, this means that, for any choice of g_{295}, varying the values of g_{357}, τ_{357}, and τ_{295} within the quoted errors has the effect of shifting the entire set of data slightly upward or downward, but does not seriously affect the relative positions of the data points as a function of projectile energy.

TABLE 5-3 Summary of Measurement of Rotation Angles for $Fe_{80}Rh_{20}$ Experiments

τ_{295} = 10.4(.6) psec

τ_{357} = 86.3(3.6) psec

ΔE (keV)	Beam	$(\frac{Q-1}{Q+1})\times10^3$ meas	Beam-Bending Correction	$(\frac{Q-1}{Q+1})\times10^3$ corr	b_2 (5% error)	$\Delta\vartheta=\frac{1}{2b_2}(\frac{Q-1}{Q+1})\times10^3$ corr (milliradians)	g
(H_2O cooled)							
295	5 Mev α	-2.14(.73)	-5.66	-7.80(.73)	-.215	18.14(1.9)	.28(16)
	6 Mev α	-3.73(1.00)	-4.77	-8.60(1.00)	-.187	23.0 (2.9)	
	7 Mev α	-1.68(1.06)	-4.12	-5.80(1.06)	-.165	17.6 (3.3)	
	8 Mev α	-1.84(1.06)	-3.62	-5.49(1.06)	-.146	18.7 (3.7)	
	9 Mev α	-2.80(1.42)	-3.43	-6.23(1.42)	-.131	23.8 (5.7)	
	35 Mev ^{16}O	-0.49	-1.64	-2.1 (2.6)	-.131	8.1 (10.2)	
(LN_2 cooled)							
	5 Mev α	-1.89(.62)	-5.66	-7.55(.62)	-.215	17.5 (1.7)	
	6 Mev α	-2.30(.85)	-4.77	-7.07(.85)	-.187	18.9 (2.7)	
	7 Mev α	-2.11(.91)	-4.12	-6.23(.91)	-.165	18.9 (3.0)	
	8 Mev α	-2.02(.91)	-3.62	-5.67(.91)	-.146	19.3 (3.3)	
	9 Mev α	-2.60(1.21)	-3.43	-5.84(1.21)	-.131	23.0 (4.7)	
(H_2O cooled)							
357	5 Mev α	+30.6(1.2)	+.087	+30.7(1.2)	+.151	101.5 (8.5)	.54(3)
	6 Mev α	+30.2(1.3)	-.12	+30.2(1.3)	+.137	110.4 (9.4)	
	7 Mev α	+28.4(1.4)	-.27	+28.4(1.4)	+.125	114.0 (8.0)	
	8 Mev α	+25.8(1.4)	-.40	+25.8(1.4)	+.1135	113.5 (8.3)	
	9 Mev α	+24.3(1.6)	-.50	+24.3(1.6)	+.103	118.0 (9.9)	
	35 Mev ^{16}O	+18.0(2.6)	+.29	+18.3(2.6)	+.104	87.9(13.5)	

(continued next page)

TABLE 5-3 (continued)

ΔE (kev)	Beam	$(\frac{Q-1}{Q+1})\times10^3$ meas	Beam-Bending Correction	$(\frac{Q-1}{Q+1})\times10^3$ corr	b_2 (5% error)	$\Delta\theta=\frac{1}{2b_2}(\frac{Q-1}{Q+1})\times10^3$ corr (milliradians)	g
(LN_2 cooled)							
	5	30.4(1.01)	+.087	31.1(1.0)	+.151	101.0(5.9)	
	6	32.3(1.11)	-.12	32.7(1.1)	+.137	117.3(6.9)	
	7	30.7(1.19)	-.27	30.7(1.2)	+.125	121.8(7.5)	
	8	24.2(1.16)	-.40	24.1(1.3)	+.1135	105.7(7.0)	
	9	24.5(1.40)	-.50	24.1(1.4)	+.103	116.5(8.5)	

Δθ VS PROJECTILE ENERGY

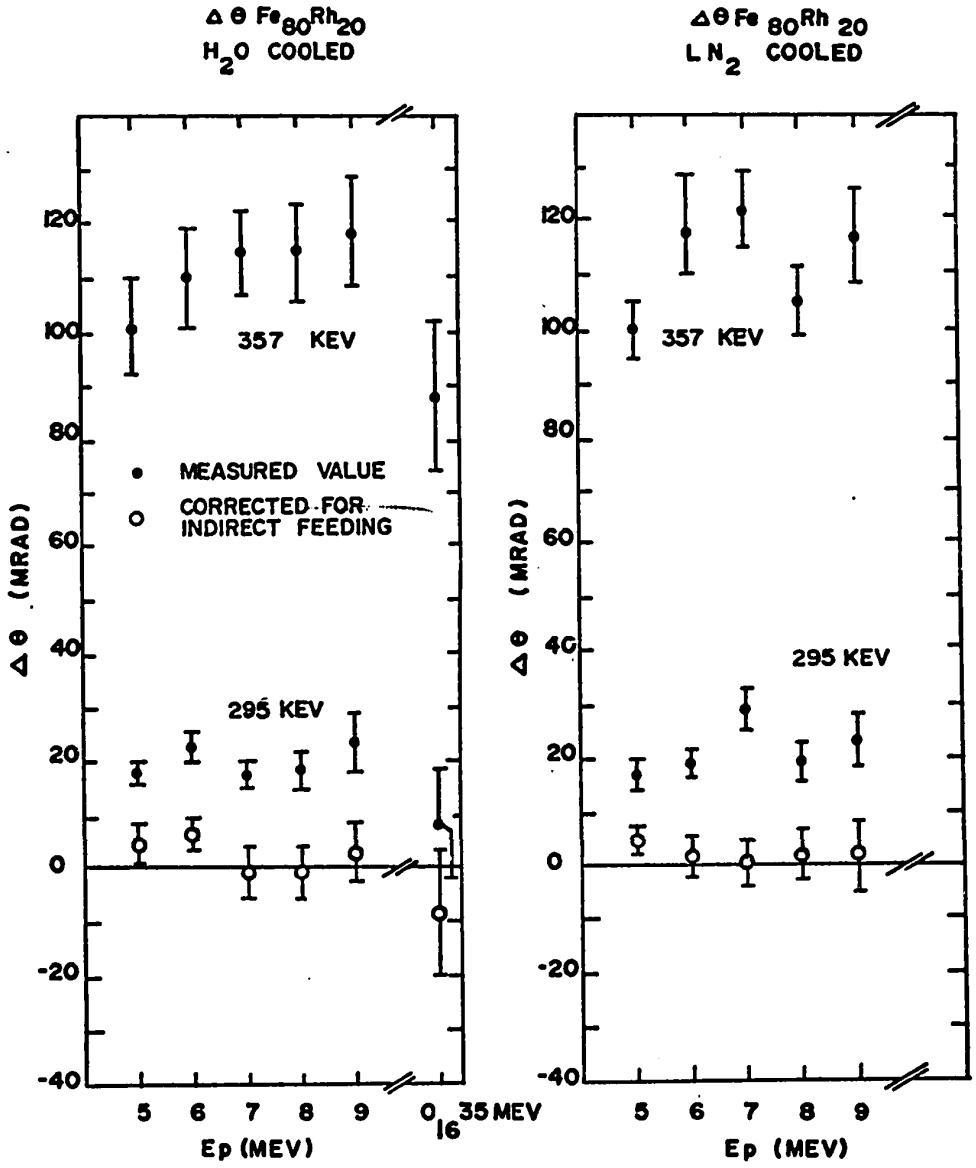

Figure 5-3

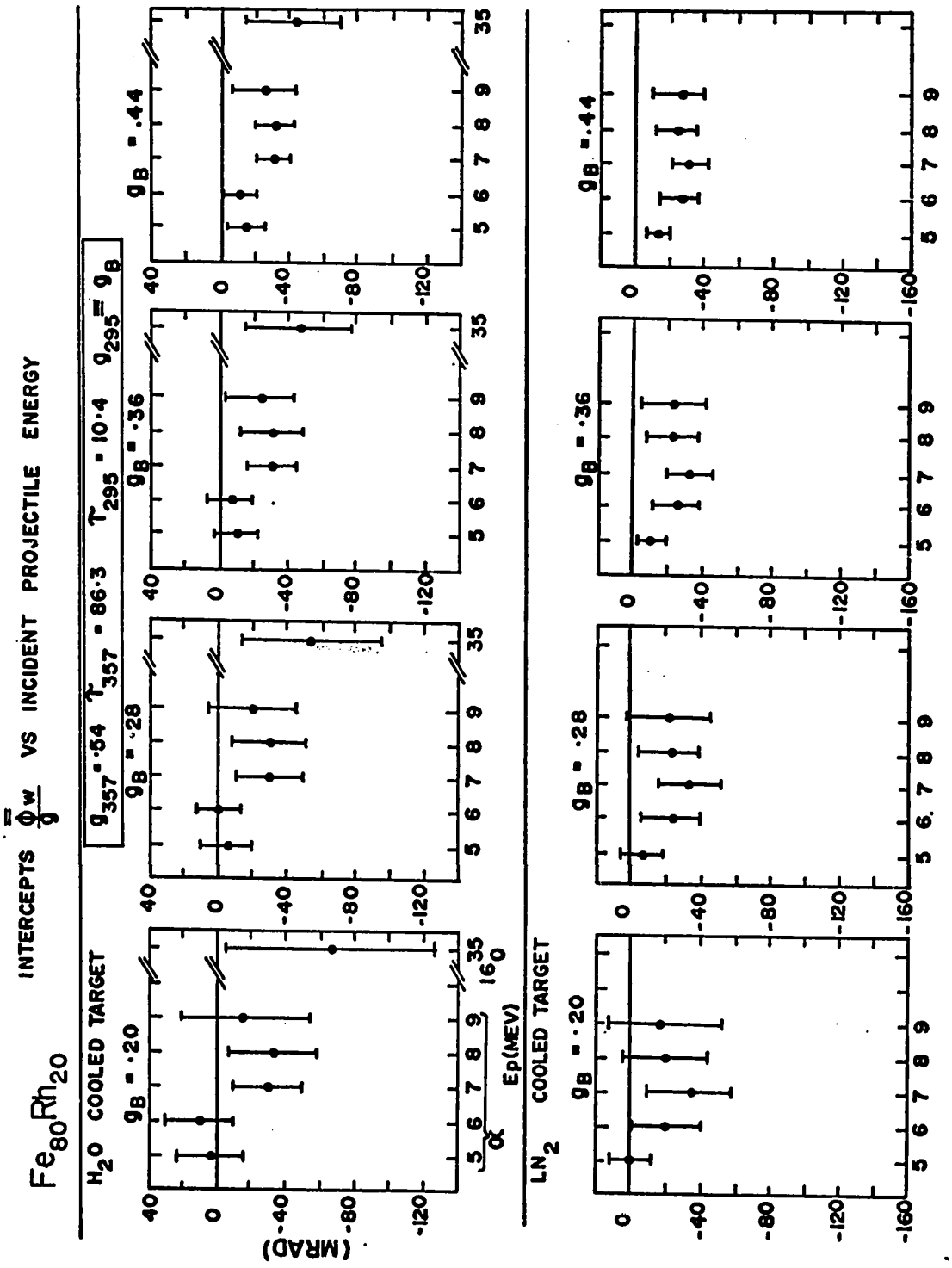
INTERCEPTS $\frac{\Phi w}{g}$ VS INCIDENT PROJECTILE ENERGY
$Fe_{80}Rh_{20}$
H_2O COOLED TARGET
g_{357} = .54 T_{357} = 86.3 T_{295} = 10.4 $g_{295} = g_B$
g_B = .20
g_B = .28
g_B = .36
g_B = .44
LN_2 COOLED TARGET
g_B = .20
g_B = .28
g_B = .36
g_B = .44
(MRAD)
Ep(MEV)
α
^{16}O
^{35}

Figure 5-4

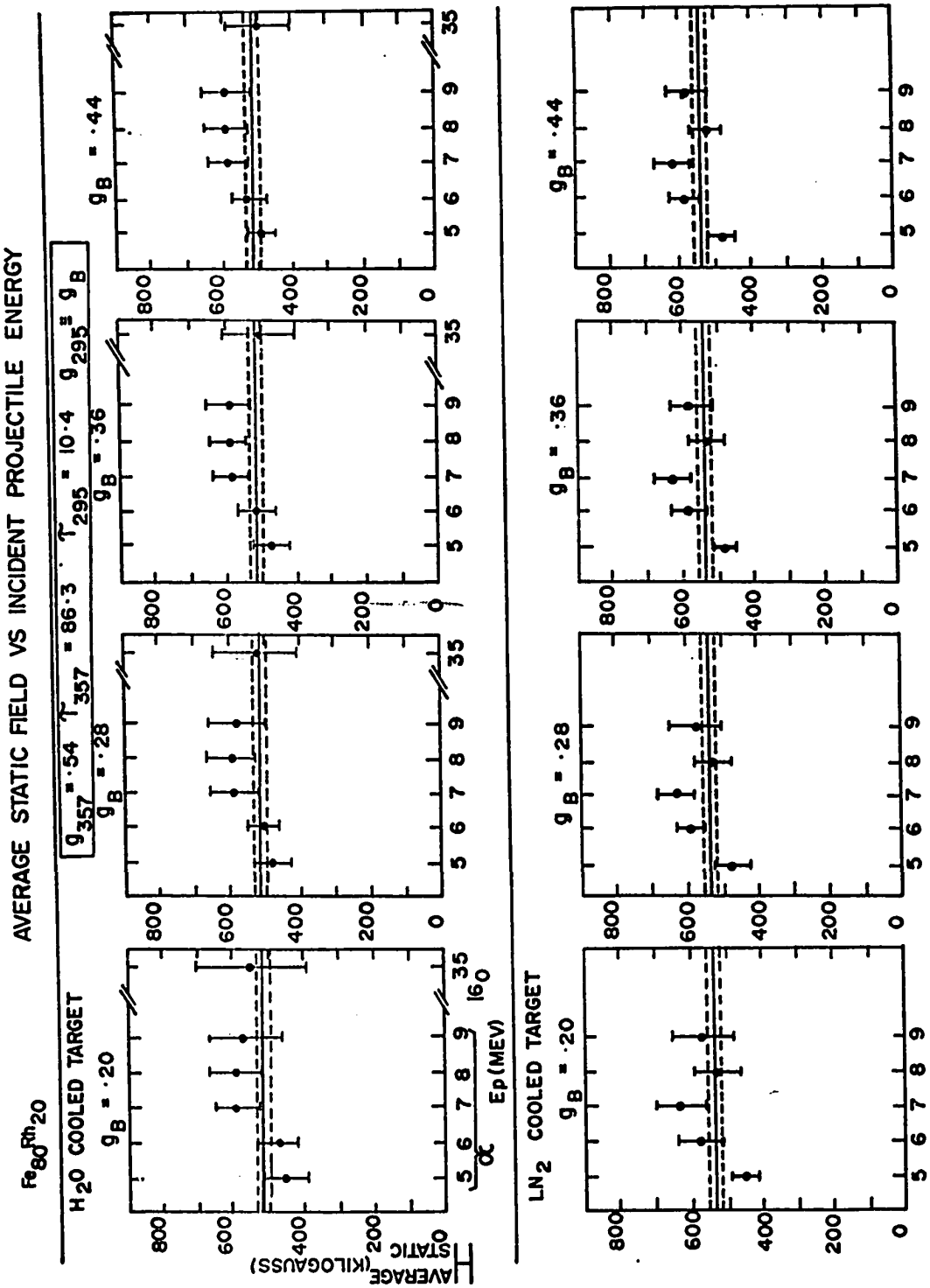
AVERAGE STATIC FIELD VS INCIDENT PROJECTILE ENERGY
$Fe_{80}Rh_{20}$
H_2O COOLED TARGET
LN_2 COOLED TARGET
$g_{357} = \cdot 54$ $\tau_{357} = 86 \cdot 3$ $\tau_{295} = 10 \cdot 4$ $g_{295} = g_B$
$g_B = \cdot 20$
$g_B = \cdot 28$
$g_B = \cdot 36$
$g_B = \cdot 44$
AVERAGE STATIC (KILOGAUSS)
Ep(MEV)
α
^{16}O

Figure 5-5

J. $Fe_{70}Pd_{30}$ ALLOY

Palladium was chosen for study because it is close to rhodium in mass number and because it has three isotopes with first 2+ states which have a nice spread in mean life (^{104}Pd, 556 kev, τ = 15.1 psec; ^{108}Pd, 434 kev, τ = 34.9 psec; ^{110}Pd, 374 kev, τ = 61.6 psec). It was desired to test whether possible changes in both static and transient field as a function of projectile energy, observed in the experiments on $Fe_{80}Rh_{20}$ alloy, were reproducible in a case where indirect feeding was not important. Only the 511 kev level in ^{106}Pd has had its g-factor measured with a diffused radioactive source. Unfortunately, this level was masked in our experiments by strong 511 kev electron-positron annihilation radiation, so no rotation angle could be measured for this state. For the states that were studied, two sets of g-factor measurements have been reported by other workers. The first [H2] was an IMPACT experiment using 38.5 Mev ^{16}O ions; the analysis assumed that the average static field seen by a stopped ion in an IMPACT experiment is the same as the internal field measured in a diffused radioactive source. Agnihotry et al[A4], employed the singles technique with 5 Mev alpha particle projectiles. They measured the internal field on ^{106}Pd using ^{106}Ru activity diffused into their $Fe_{80}Pd_{20}$ target. However, in view of the discussion of radiation damage and final site of recoiling ion presented in Chapter II, it is not obvious that the internal field measured following diffusion

should equal the internal field measured under dynamic bombardment conditions for either a singles (light projectile) or IMPACT (heavy projectile) experiment. Experiments on ion implantation have indicated that, in certain cases, internal fields measured by ion implantation agree with internal fields measured in diffused sources, but there are at least as many cases where the values do not agree.

Because of the difficulties stated above in measuring the g-factors of ^{104,108,110}Pd, it was decided that it was best not to introduce bias into the data analysis arising from possibly incorrect g-factor values. Straight lines were least-squares fit to plots of $\Delta\theta$ vs τ for the 374 kev, 434 kev, and 556 kev levels. The systematics of first 2+ states in even-even nuclei would seem to indicate that the g-factors for the states in ^{104,108,110}Pd can be considered equal to within 20% with reasonable certainty. So even if the least-squares fit straight line has an "incorrect" slope and intercept by virtue of unequal g-factors, this error will be a systematic one, and will be independent of projectile bombarding energy; therefore the comparison of slopes and intercepts for different bombarding energies will still be meaningful. Experimental results for this alloy are listed in Table 5-4 and plotted in Figures 5-6, 5-7 and 5-8.

The target consisted of 3 components; (1) natural Pd (2) Pd enriched to 63% in ^{104}Pd and (3) natural iron. These

TABLE 5-4 Summary of Calculations of Rotation Angles for $Fe_{70}Pd_{30}$ Alloy

$\tau_{374} = 61.6(4.1)$ $\tau_{434} = 34.9(2.3)$ $\tau_{556} = 15.1(1.5)$

ΔE (keV)	Beam	$(\frac{Q-1}{Q+1})\times10^3$ meas	Beam-Bending Correction	$(\frac{Q-1}{Q+1})\times10^3$ corr	b_2 (5% error)	$\Delta\theta=\frac{1}{2b_2}(\frac{Q-1}{Q+1})\times10^3$ corr (milliradians)	g
(H_2O Cool)							
373.8	6 Mev α	10.8(1.3)	+.4(.15)	11.2(1.4)	.178	31.3(4.0)	
	7 Mev α	9.2(1.2)	+.2(.15)	9.4(1.4)	.188	28.9(4.0)	
	8 Mev α	7.7(2.5)	-0.02(.15)	7.7(3.6)	.204	26.8(8.8)	
433.9	6 Mev α	5.8(1.1)	.5(.15)	6.3(1.3)	.188	16.8(3.0)	
	7 Mev α	5.7(.9)	.3(.15)	6.0(1.1)	.178	16.8(2.7)	
	8 Mev α	8.9(1.7)	.1(.15)	9.0(1.9)	.158	28.4(5.6)	
555.5	6 Mev α	4.2(1.4)	.6(.15)	4.8(1.6)	.204	11.9(3.5)	
	7 Mev α	2.2(1.0)	.4(.15)	2.6(1.2)	.191	6.8(2.6)	
	8 Mev α	2.1(1.7)	.3(.15)	2.4(1.9)	.187	6.2(4.6)	
(LN_2 cool)							
373.8	6 Mev α	8.7(1.2)	.4(.15)	9.1(1.4)	.178	25.5(3.6)	
	7 Mev α	11.0(1.5)	.2(.15)	11.2(1.7)	.188	34.7(5.0)	
	8 Mev α	11.3(1.9)	-.02(.15)	11.3(2.1)	.204	39.1(6.9)	
433.9	6 Mev α	6.2(.9)	.5(.15)	6.7(1.1)	.188	17.8(2.6)	
	7 Mev α	7.5(1.0)	.3(.15)	7.8(1.2)	.178	21.7(3.0)	
	8 Mev α	5.5(1.2)	.1(.15)	5.6(1.4)	.158	17.6(3.9)	
555.5	6 Mev α	3.6(1.3)	.6(.15)	4.2(1.5)	.204	10.3(3.2)	
	7 Mev α	4.5(1.2)	.4(.15)	4.9(1.4)	.191	12.8(3.3)	
	8 Mev α	3.3(1.3)	.3(.15)	3.6(1.5)	.187	9.5(3.5)	

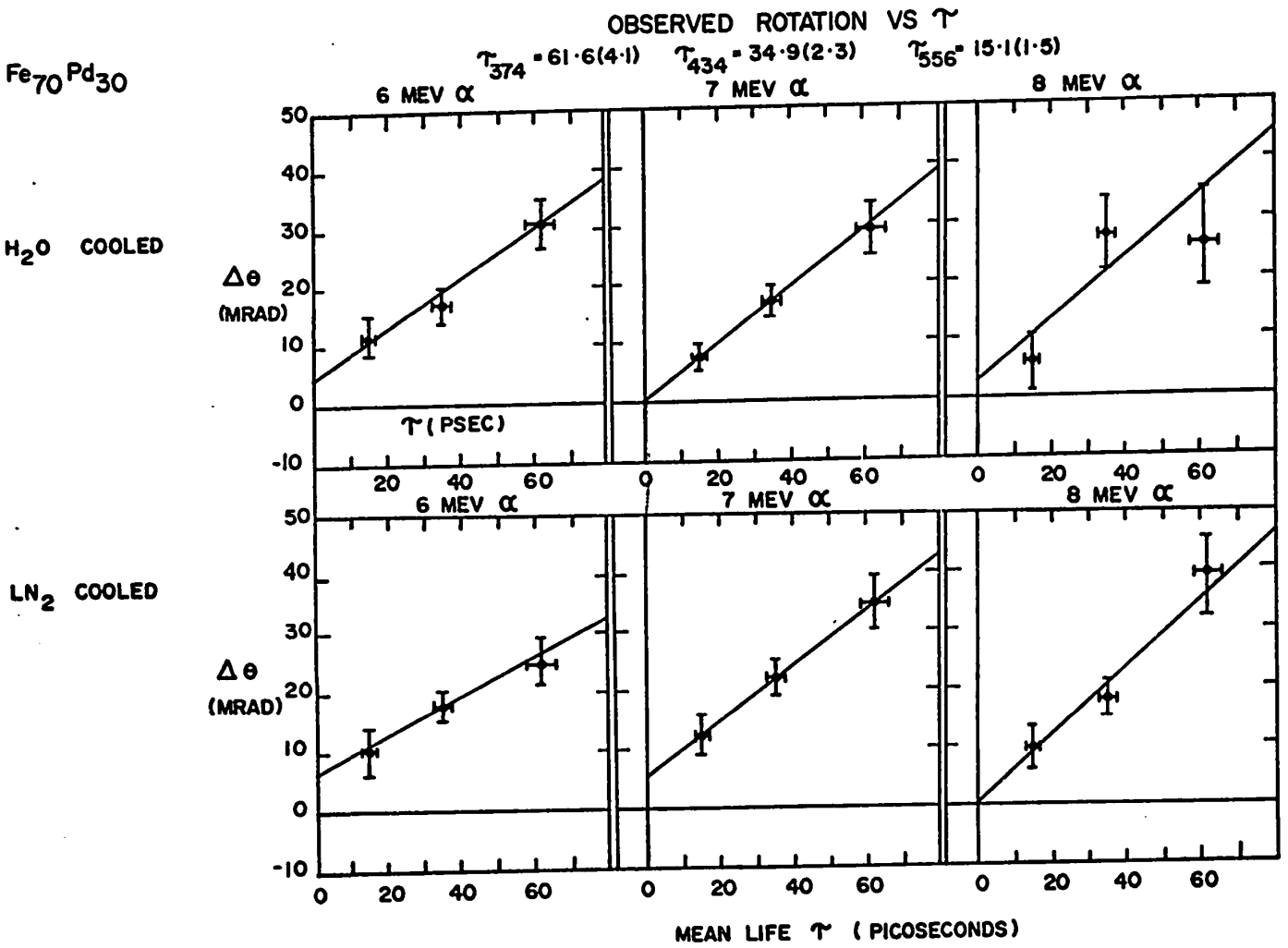
OBSERVED ROTATION VS τ
τ374 = 61·6(4·1)
τ434 = 34·9(2·3)
τ556 = 15·1(1·5)
Fe70Pd30
H2O COOLED
LN2 COOLED
6 MEV α
7 MEV α
8 MEV α
Δθ (MRAD)
τ (PSEC)
MEAN LIFE τ (PICOSECONDS)

Figure 5-6

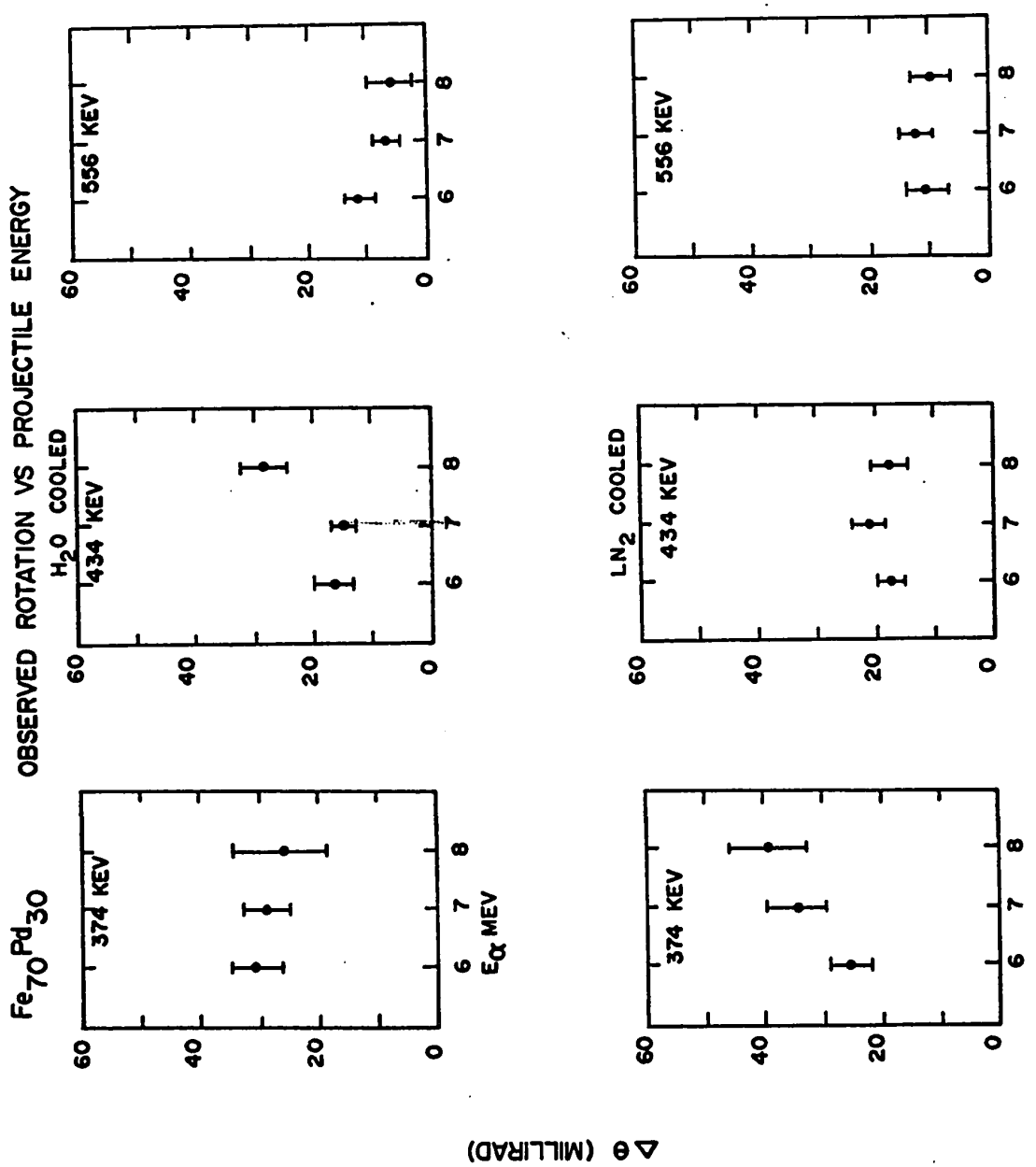
OBSERVED ROTATION VS PROJECTILE ENERGY
$Fe_{70}Pd_{30}$
374 KEV
434 KEV
556 KEV
H_2O COOLED
LN_2 COOLED
E_α MEV
Δθ (MILLIRAD)

Figure 5-7

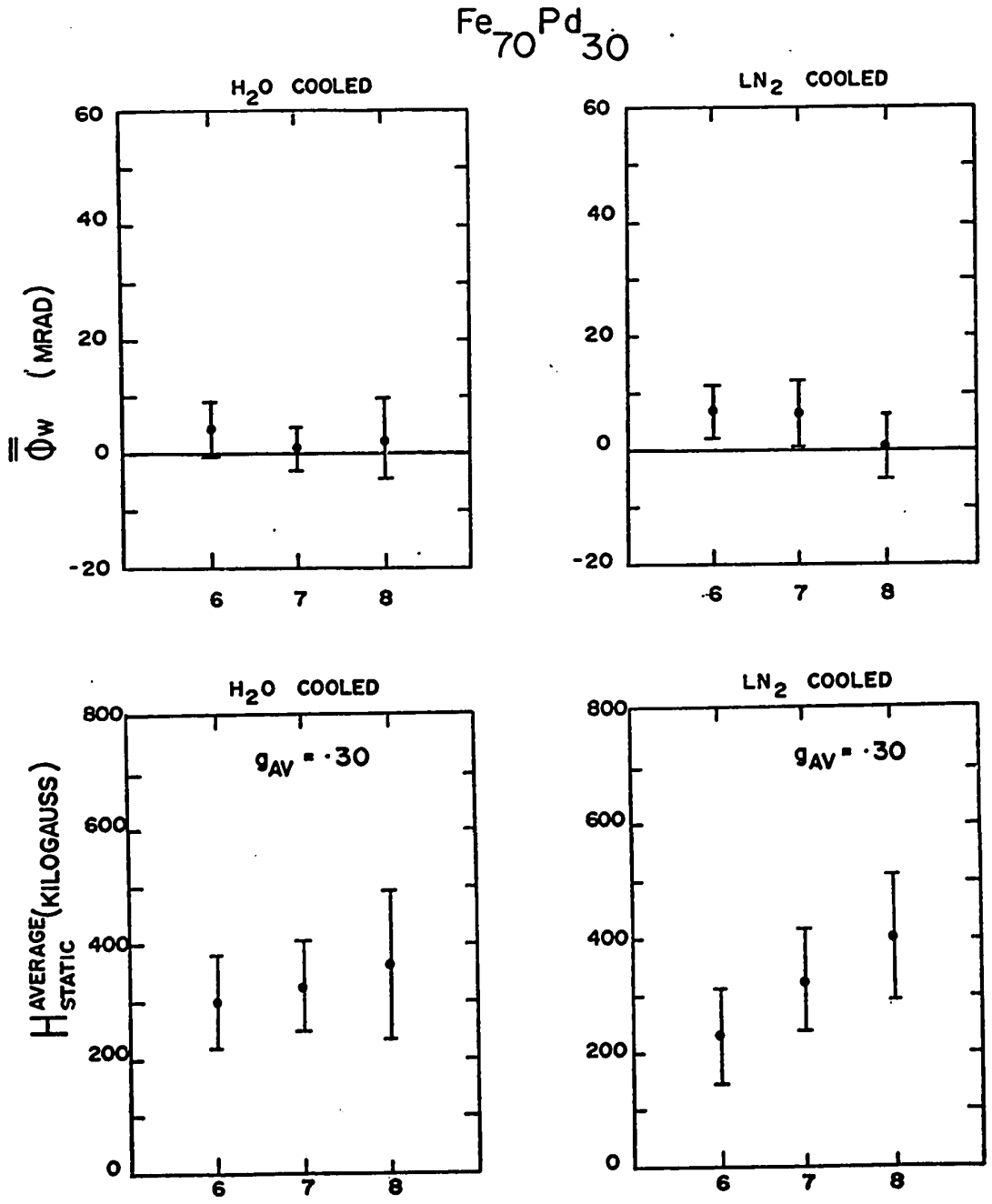
Fe70Pd30
H2O COOLED
LN2 COOLED
≡ Φw (MRAD)
60
40
20
0
-20
6
7
8
H2O COOLED
LN2 COOLED
gAV = ·30
gAV = ·30
H AVERAGE STATIC (KILOGAUSS)
800
600
400
200
0
6
7
8

Figure 5-8

components were mixed in appropriate amounts so that the 374 kev, 434 kev and 556 kev levels were of comparable intensity and the overall Pd concentration was 30 atomic per cent.

K. $Fe_{85}Pt_{15}$ ALLOY (Table 5-5, Fig. 5-9)

Platinum was chosen for study because its large mass (A ∿ 195) would permit one to use alpha particles, ^{12}C, and ^{16}O projectiles to probe different regions of recoil velocity than was the case with medium-A nuclei (A ∿ 100). It also offered an opportunity to test the dependence of transient field on the Z of the target. Its isotopes have a total of 5 states, with a wide spread in mean life, which can be readily Coulomb-excited, and two of the states (^{194}Pt, 329 kev, τ = 51.0 psec; ^{196}Pt, 356 kev, τ = 43.5 psec) have had their g factors measured by radioactivity measurements in diffused sources. The remaining three states are in ^{195}Pt(211 kev, τ = 97 psec; 239 kev, τ = 115 psec) and in ^{198}Pt(408 kev, τ = 27.7 psec.).

In extracting peak areas, the analysis was complicated by the fact that (1) the 329 kev peak was located atop the Compton edge for the 511 kev annihilation radiation,and (2) the 356 kev line was not completely resolved from a 352 kev line that arose from Coulomb excitation of ^{57}Fe. The presence of the Compton edge under the 329 kev peak made the background very non-linear and caused it to change curvature from one side of the peak to the other. This change in curvature made it

difficult to choose an analytic function that would fit the background well on both sides of the peak. Both linear and parabolic background functions were used, with a variety of background windows. An average of those values of Q^2 that agreed within error was adopted as the accepted value. For the spectra with 35 Mev ^{16}O and 20 Mev ^{12}C projectiles, the above problems of irregular background shape were so acute for 329 kev and 211 kev peaks that a new method of background analysis was adopted. A numerical function was chosen by graphical means which varied smoothly and fit the background shape rather well; then this numerical function was used to fit both field up and field down backgrounds using a scaling factor as the only degree of freedom.

For the 356 kev peak, an attempt was made to minimize the effect of the incompletely resolved 352 kev peak by setting the lower peak window so as to exclude all of the 352 kev peak from the calculated area.

Since not all of the states under consideration were first 2+ states in even-even isotopes, and the g-factors of the first 2+ states were known to small error, it was decided to analyze the data by doing a linear least squares fit to a plot of $\frac{\Delta\theta}{g}$ vs τ . Because ^{198}Pt is only 7.23% abundant in natural platinum the 408 kev line from ^{198}Pt was of low intensity and tended to be swamped by the tail of a strong line at 417 kev. A meaningful number for this state could be extracted only for the spectrum with 7 Mev alpha projectiles. For the 211 kev

level, the value of the E2/M1 mixing ratio for the 3/2- → 1/2- 211 kev transition results in a small A_2 angular distribution coefficient. As a result, the measured value of $(\frac{Q-1}{Q+1})$ is small, and has a large relative error. This fact has meant that previous measurements of the g factor of this state by other workers[K7,V1], have had large relative errors associated with them. In view of this large relative error, the 211 kev level did not appear tc be very useful in a study of the projectile energy dependence of the transient field. Therefore, it was decided to use the data points from the 408 kev, 329 kev, 356 kev and 239 kev levels for 7 Mev alpha projectiles to measure the g factor of the 211 kev state with full corrections for indirect feeding.

Using the straight line fit to $\frac{\Delta\theta}{g}$ vs τ for these four states, and employing the uncertainties in the slope and intercept of this line, the value of $\frac{\Delta\theta}{g}$ appropriate to τ = 97(6) (the mean life of the 211 kev state) was calculated. The uncertainty in τ was incorporated into the uncertainty in $\frac{\Delta\theta}{g}$. Then the measured rotation angle of the 211 kev state, corrected for indirect feeding from the 295 kev state, was used to calculate g_{211} from the relation $g_{211} = \Delta\theta_{Corr}/(\Delta\theta/g)$. The result was g_{211} = .164(66). This number is in agreement within error with the results of previous workers (Varga et al[V1], g_{211} = .104(21); Kugel et al[K7], g_{211} = .16(6)). Only one of these authors[V1] has taken indirect feeding into account.

TABLE 5-5 Summary of Measurement of Rotation Angles for $Fe_{85}Pt_{15}$ Experiments

τ_{211} = 97(6) τ_{239} = 115(5.8) τ_{329} = 51.0(2.6) τ_{356} = 43.5(1.8) τ_{408} = 27.4(4.3)

ΔE (keV)	Beam	$(\frac{Q-1}{Q+1})\times 10^3$ meas	Beam-Bending Correction	$(\frac{Q-1}{Q+1})\times 10^3$ corr	b_2 (5% error)	$\Delta\theta=\frac{1}{2b_2}(\frac{Q-1}{Q+1})\times 10^3$ corr (milliradians)	g
(H_2O cooled)							
211	7 Mev α	9.5(1.33)	-1.4	8.1(1.33)	.0405	100(17)	-
239		24.3(2.99)	-0.2	24.1(2.99)	.128	90.6(12.5)	.231(14)
329		15.4(0.83)	+0.4	15.8(0.83)	.173	45.6(3.3)	.298(18)
356		14.3(1.5)	+0.4	14.7(1.5)	.176	41.7(4.7)	.323(20)
408		9.3(8.0)	+0.5	9.8(8.0)	.186	26.3(21.6)	.28(4)
211	35 Mev ^{16}O	17.3(4.4)	-0.8	16.5(4.4)	.0345	239(65)	-
239		29.7(6.5)	-0.3	29.4(6.5)	.108	136(31)	.231(14)
329		12.8(1.3)	+0.6	13.4(1.3)	.152	42.3(4.9)	.298(18)
356		11.4(2.2)	+0.1	11.5(2.2)	.159	36.2(7.3)	.323(20)
408		-		-	.165	-	.38 (4)
329	^{12}C	18.6(5.0)	+0.3	18.9(5.0)	.182	51.2(13.7)	.298(18)

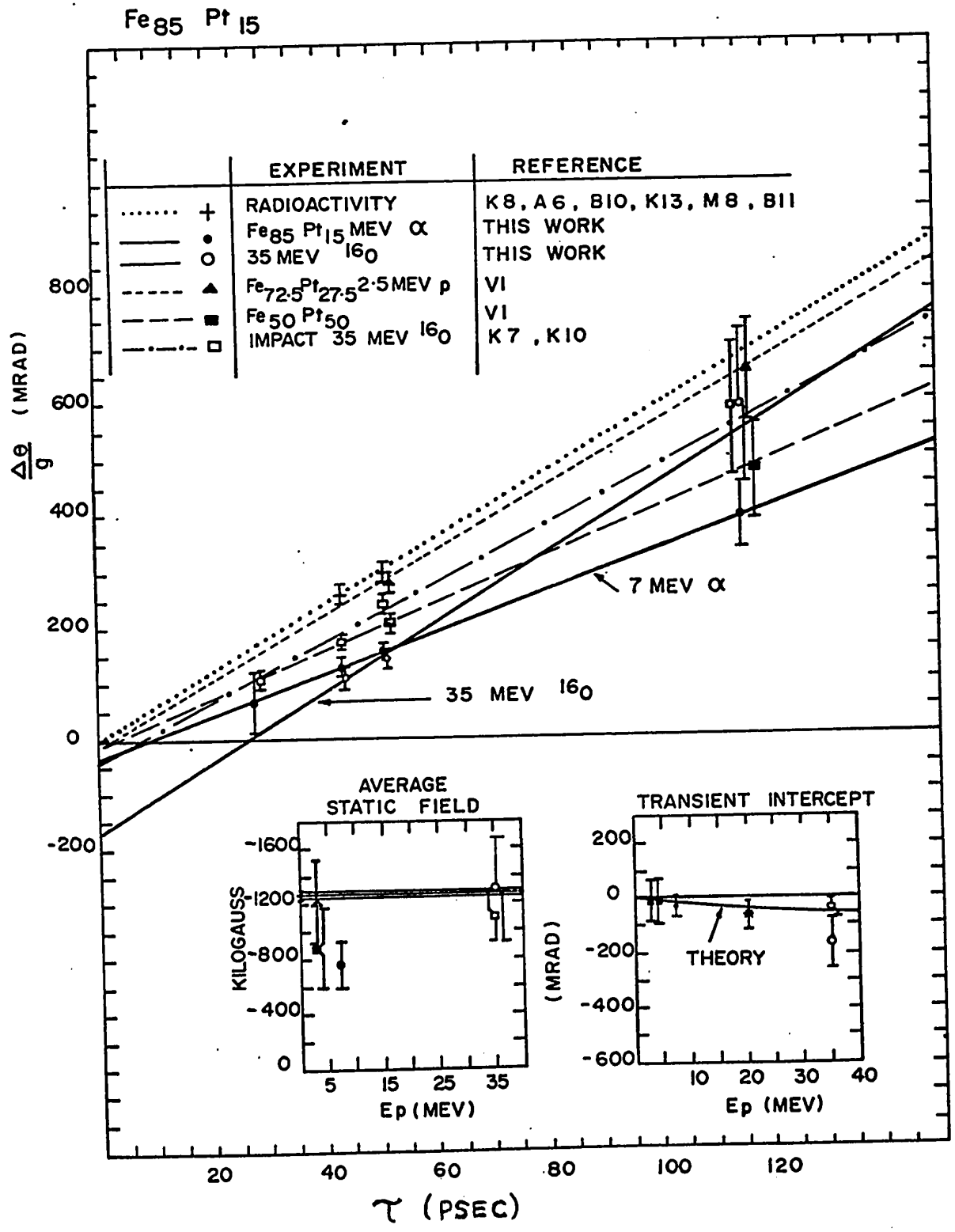
Fe85 Pt15
EXPERIMENT
REFERENCE
RADIOACTIVITY
K8, A6, B10, K13, M8, B11
Fe85 Pt15 MEV α
THIS WORK
35 MEV 16O
THIS WORK
Fe72.5Pt27.5 2.5 MEV p
VI
Fe50 Pt50
VI
IMPACT 35 MEV 16O
K7, K10
Δθ/g (MRAD)
800
600
400
200
0
-200
7 MEV α
35 MEV 16O
AVERAGE STATIC FIELD
KILOGAUSS
-1600
-1200
-800
-400
0
5
15
25
35
Ep (MEV)
TRANSIENT INTERCEPT
(MRAD)
200
0
-200
-400
-600
THEORY
10
20
30
40
Ep (MEV)
20
40
60
80
100
120
τ (PSEC)

Figure 5-9.

CHAPTER VI

DISCUSSION OF RESULTS

In this chapter, the experimental results reported in Chapter V are discussed with the purpose of drawing conclusions regarding the behaviour of the transient and average static rotations as a function of low projectile recoil velocity. A comparison with the theoretical prediction of the observed transient rotation as a function of recoil velocity, which was developed in Chapter III using Lindhard and Winther's transient field theory, is presented.

Finally a comparison is drawn between the current results and relevant results of other workers.

Figures 6-1 through 6-3 contain the measured intercepts $\frac{\bar{\phi}_w}{g}$ and the theoretical curves calculated as outlined in Chapter III, for $Fe_{80}Rh_{20}$, $Fe_{70}Pd_{30}$, and $Fe_{85}Pt_{15}$; the data are plotted as a function of the maximum initial recoil velocity appropriate to each experiment.

From these figures, it can be seen that generally the experimental values agree within error with the theoretical predictions for each alloy. Some comments on specific cases are in order.

A. $Fe_{80}Rh_{20}$ ALLOY

As already discussed it was deemed prudent to analyze the results for different values of the g factor

TABLE 6-1 Summary of Transient Field Calculations for Representative Cases

Nucleus	Projectile	E (Mev)	ΔE (kev)	Maximum Initial Recoil Velocity ($\times 10^8$ cm/sec.)	Transient Field ϕ_W/g (mrad)	Transient Field $\bar{\phi}_W/g$ (mrad)	Transient Field $\bar{\bar{\phi}}_W/g$ (mrad)
103 RH	Alpha	5	357	1.14	9.14	6.44	5.84
		6		1.25	10.04	7.54	6.59
		7		1.36	10.80	8.84	7.40
		8		1.45	11.46	10.33	8.28
		9		1.54	12.04	12.13	9.22
		10		1.63	12.57	14.23	10.25
103 RH	^{16}O	10	357	2.92	18.08	15.06	14.87
		15		3.59	19.79	16.48	16.14
		20		4.17	20.89	17.75	17.14
		25		4.66	21.66	19.17	18.13
		30		5.10	22.25	20.80	19.17
		35		5.52	22.72	22.58	20.26
194 PT	Alpha	5	329	0.62	17.91	12.37	11.84
		6		0.68	19.47	13.52	12.78
		7		0.74	20.87	14.80	13.69
		8		0.79	22.17	16.23	14.65
		9		0.84	23.38	17.81	15.67
		10		0.88	24.52	19.70	16.75
194 PT	^{16}O	10	329	1.74	42.82	34.28	34.22
		15		2.04	47.33	37.02	36.31
		20		2.36	51.50	39.97	38.92
		25		2.64	54.72	42.92	41.26
		30		2.89	57.31	46.06	43.55
		35		3.12	59.57	49.54	45.95

Figure 6-1 (Integrated transient rotation/g) vs maximum initial recoil velocity for rhodium in iron

Key: (1) - Singles, 2.5 Mev protons on $Fe_{97}Rh_{03}$ alloy (Ref.S5)

(2) - Singles, 5-9 Mev alphas on $Fe_{80}Rh_{20}$ alloy (This work)

(3) - Singles 35 MeV ^{16}O on $Fe_{80}Rh_{20}$ alloy (This work)

(4) - IMPACT, ∿ 35 Mev ^{16}O (R1)

Figure 6-2 Integrated transient rotation vs maximum initial recoil velocity for palladium in iron.

Key: (1) - 5 Mev alphas on $Fe_{80}Pd_{20}$ alloy (Ref. A4)

(2) - 6-8 Mev alphas on $Fe_{70}Pd_{30}$ alloy (This work)

(3) - IMPACT, ∿ 35 Mev ^{16}O (Ref. H2)

Figure 6-3 (Integrated transient rotation/g) vs maximum initial recoil velocity for platinum in iron

Key: (1) - 2.5 Mev protons on $Fe_{72.5}Pt_{27.5}$ and $Fe_{50}Pt_{50}$ alloys (Ref. V1)

(2) - 7 Mev alphas on $Fe_{85}Pt_{15}$ alloy (This work)

*(3) - IMPACT, ^{196}Pt, 35 MeV ^{16}O, also ^{32}S and ^{35}Cl beams.

(4) IMPACT, 35 Mev ^{16}O (Ref. K10)

(5) 35 Mev ^{16}O on $Fe_{85}Pt_{15}$ alloy (This work)

*These points are extracted assuming that static field is same as for radioactivity measurements. Ref. G.M. Heestand, P. Hvelplund, B. Skaali, B. Herskind, Phys. Rev. B2 (1970) 3698.

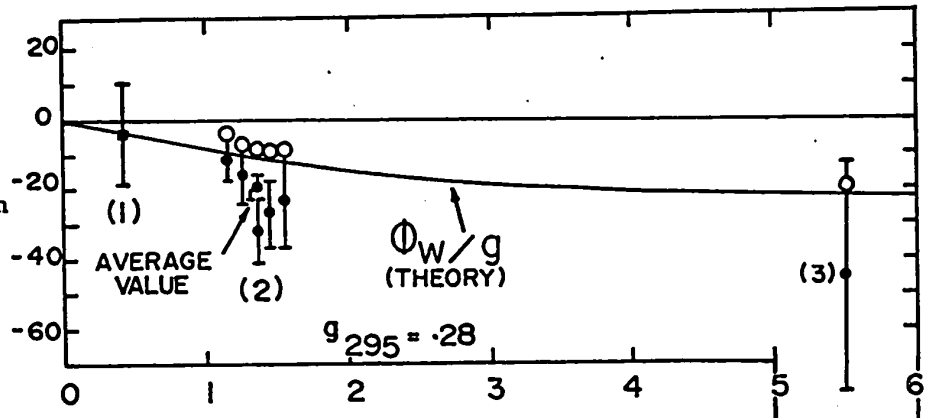

Figure 6-1

Rhodium in Iron

(Open circles are values of $\bar{\Phi}_w/g$)

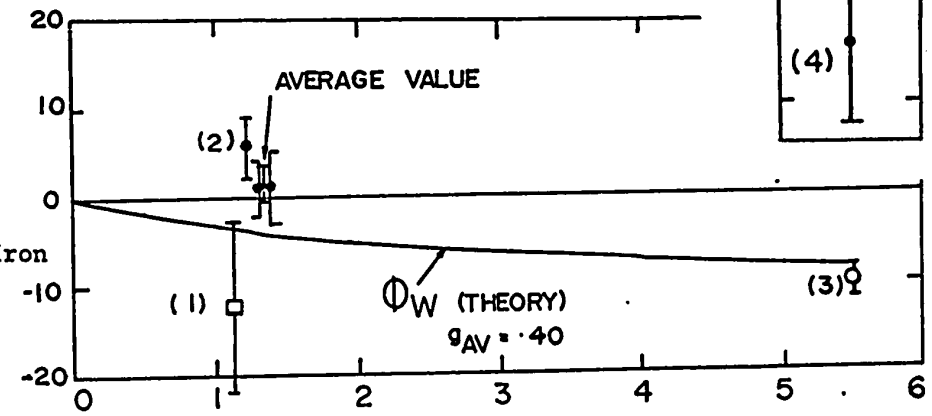

Figure 6-2

Palladium in Iron

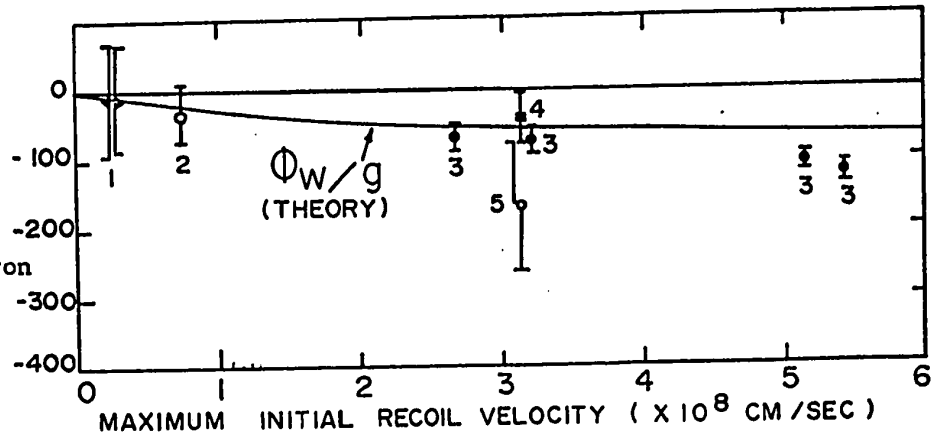

Figure 6-3

Platinum in Iron

TABLE 6-2 Summary of Measured Rotation Angles for Rhodium-103 in Iron

Experiment			Δθ (milliradians)		
Method	Target	Projectile	295 kev[a]	357 kev	Reference
Singles	$Fe_{80}Rh_{20}$	5 Mev alpha	18.1(1.9	101.5(8.5)	This work
	(H_2O cool)	6 Mev alpha	23.0(2.9)	110.4(9.4)	This work
		7 Mev alpha	17.6(3.3)	114.0(8.0)	This work
		8 Mev alpha	18.7(3.7)	113.5(8.3)	This work
		9 Mev alpha	23.8(5.7)	118.0(9.9)	This work
		35 Mev ^{16}O	8.1(10.2)	87.9(13.5)	This work
	$Fe_{80}Rh_{20}$	5 Mev alpha	17.6(1.7)	101.0(5.9)	This work
	(LN_2 cool)	6 Mev alpha	18.9(2.7)	117.3(6.9)	This work
		7 Mev alpha	18.9(3.0)	121.8(7.5)	This work
		8 Mev alpha	19.3(3.3)	105.7(7.0)	This work
		9 Mev alpha	23.0(4.7)	116.5(8.5)	This work
Singles	$Fe_{95}Rh_{05}$	5 Mev alpha	29 (7)	108 (14)	B6
Singles	$Fe_{97}Rh_{03}$	2.5 Mev protons	23 (3)	121 (5)	S5
IMPACT	Sandwich	∿35 Mev ^{16}O	-4 (5)	103 (7)	R1

a) Not corrected for indirect feeding

TABLE 6-3 Summary of Measured Rotation Angles for Palladium in Iron

Experiment			Δθ (milliradians)				
Method	Target	Projectile	^{104}Pd 556 kev	^{106}Pd 512 kev	^{108}Pd 434 kev	^{110}Pd 374 kev	Reference
Singles	$Fe_{70}Pd_{30}$ (H_2O cool)	6 Mev alpha	11.9(3.5)		16.8(3.0)	31.3(4.0)	This work
		7 Mev alpha	6.8(2.6)		16.8(2.7)	28.9(4.0)	This work
		8 Mev alpha	6.2(4.6)		28.4(5.6)	26.8(8.8)	This work
	$Fe_{70}Pd_{30}$ (LN_2 cool)	6 Mev alpha	10.3(3.2)		17.8(2.6)	25.5(3.6)	This work
		7 Mev alpha	12.8(3.3)		21.7(3.0)	34.7(5.0)	This work
		8 Mev alpha	9.5(3.5)		17.6(3.9)	39.1(6.9)	This work
	(H_2O+LN_2 cool)	weighted average	9.0(1.5)		18.1(1.4)	32.1(2.7)	
Singles	$Fe_{80}Pd_{20}$	5 Mev alpha			13.2(2.8)	33.8(6.0)	A4
IMPACT	Sandwich	∿35 Mev ^{16}O	-0.8(1.4)	4.5(2.6)	17.5(1.6)	35.0(2.3)	H2
Radioactivity	Diffused ^{106}Rh in iron	-		17.6(.3)			A5
				18.0(.7)			M5
				17.6(.3)			B9
				1.73(.11)			J1[a]

TABLE 6-4 Summary of Measured Rotation Angles for Platinum in Iron

Method	Target	Projectile	Δθ (milliradians) ^{194}Pt 329 keV	^{195}Pt 211 a) keV	^{195}Pt 239 keV	^{196}Pt 356 kev	^{198}Pt 408 kev	Reference
Singles	$Fe_{85}Pt_{15}$	7 Mev α	45.6(3.3)	100(17.1)	90.6(12.5)	41.7(4.7)	26.3(21.6)	This work
	(H_2O COOL)	35 Mev ^{16}O	42.3(4.9)	239(65)	136(31)	36.2(7.3)	-	This work
		20 Mev ^{12}C	51.2(13.7)	-	-	-	-	This work
Singles (LN_2 COOL)	$Fe_{72.5}Pt_{27.5}$	2.5 Mev protons	84.5(2.8)	58(14) b)	151(19)			V1
	$Fe_{50}Pt_{50}$		61.0(3.5)	38(13)	110(10)			V1
IMPACT	Sandwich	35 Mev ^{16}O	70(4)			55(3)	30.5(2.0)	K10
			73(5)	80(24)	135(27)	66(13)		K7
Radio-activity	Diffused in iron	-	91.6(6.7)					K8
		-	99.0(9.0)					A6
			97(4)					B10
			87(4)					K13
		Accepted	90(2)					M8
						81.8(4.7)		
Radio-activity	Implanted source	-				85.0(5.2)		B11
						Accepted 83.4(3.5)		

a) Not corrected for indirect feeding

b) Corrected for indirect feeding

of the 295 keV state because of the uncertainty in its value due to the indirect feeding component. From Fig. 5-4 it can be seen that the general shape of the curve of $\bar{\phi}_w/g$ as a function of E_p is not very sensitive to the assumed value of the g factor of the 295 kev state. The reason for this is clear from Fig. 5-3: when the effect of the 357 kev state is extracted, the rotation angles of the 295 kev state are close to zero, within error. Thus, their absolute values will not change greatly when scaled by a g factor whose value is changed by a factor of 2. However the absolute value of the uncertainty in this rotation angle also scales with the g factor. Hence the absolute uncertainty in the intercept is largest for the smallest assumed value of g.

There appears to be a trend, independent of the assumed value for g_{295} toward an increase in the negative value of the intercept in passing from 5 to 9 Mev alpha particles. This trend occurs both for H_2O-cooled and liquid nitrogen-cooled targets. If $g_{295} < .20$, the uncertainties in the intercepts become too large to make the results meaningful. For larger values of g_{295}, the uncertainty in each intercept becomes smaller. Until the g factor of the 295 keV state is known to much better accuracy, one cannot draw a definite conclusion about the statistical significance of the change in the value of the intercept. If $g_{295} > .36$,it would appear that the values of the intercepts at 7 and 8 Mev alpha energy are larger than the theoretical predictions,while at 5 and 6 Mev alpha energy, the values agree with

the theoretical predictions within error.

The cause of the change in the value of the intercept as a function of projectile energy can be seen by referring to Fig. 5-3. From this figure, it can be seen that the measured rotation angle of the 295 kev state, when corrected for the influence of the 357 kev state, is constant within error. On the other hand, the measured rotation angle of the 357 kev state appears to increase monotonically in passing from 5 to 9 Mev alpha energy. Since a horizontal straight line can be drawn through the alpha particle points with a $\chi^2 \lesssim 1$, it cannot be concluded that this trend is statistically significant. The decrease in the rotation angle from ^{4}He to ^{16}O projectile can be accounted for in terms of the transient field effect. The intercept for ^{16}O projectile agrees with the theoretical prediction within error, but the uncertainty in the experimental value is large. The intercepts for 7,8, and 9 Mev alpha energy are all negative and non-zero if $g_{295} > .28$.

B. $Fe_{70}Pd_{30}$ ALLOY

Reference to Figures 5-6, 5-7, and 5-8 indicates that, for the experiments with 6, 7 and 8 Mev alpha particle projectiles on water-cooled and liquid nitrogen-cooled targets, the intercepts are either zero or positive to within 10 milliradians. No systematic change of statistical significance in the intercept values could be discerned as a function of projectile energy. The static field values for all of the experiments were equal within error. The positive intercepts

can be explained if the g factors of the 556 kev and 434 kev states are larger than the g factor of the 374 kev state. This conclusion is consistent with the measured values of the g factors of these states reported by Heestand[H2] and Agnihotry[A4]; these authors used IMPACT with oxygen ions and singles perturbed angular distributions with 5 Mev alphas respectively.

Since no systematic trend in the values of the intercepts or slopes could be noted, it was decided to treat the 6 experiments (6, 7, 8, Mev and H_2O, LN_2 coolants) as six repeated measurements of the same rotation angles. For each nuclear state, all of the rotation angles which were equal within experimental error were averaged. The weighted averages are listed in Table 6-3. Then a least-squares fit to $\Delta\theta$ vs τ was carried out. The intercept was not zero within error.

A value for the internal field was extracted by assuming that, to a first approximation, the g factors of the three states were equal to the g factor of the 512 kev first 2+ state in ^{106}Pd. This g factor has been measured both in an external field and with a radioactive source diffused in iron[A5,M5,B9,J1]. A weighted average of the rotation angles measured by the latter four authors was carried out with the result $\omega\tau_{AV}$ = 17.45(.25) mrad. The mean life of the 512 kev state was determined by taking a weighted average of the available B(E2) values for this state which agreed within experimental error. The result

was τ_{512} = 16.60(.65) p sec. The value of the internal field was assumed to be the same as the internal field measured in ^{105}Pd (the hyperfine anomaly is expected to be only 2 or 3 percent), H_o = -573(20) kGauss. From these measurements, one obtains g_{512} = .400(17) . Then $H^{\text{average}}_{\text{static}} = \frac{\hbar}{\mu_N} \frac{\omega_{Av}}{g_{512}}$ = -271(20) kGauss. The mean lives of the first 2+ states in ^{104,108,110}Pd were taken to be weighted averages of all measurements to date which agreed within error .

These average values were τ_{556} 14.5(.8) p sec, τ_{434} = 35.2(1.6) psec, and τ_{374} = 63.5(2.2) p sec.

The g factors of the 556, 434, 374 kev states were extracted from the relation: $\frac{(\omega\tau)_x}{g_x} = \frac{\omega_{av}\tau_x}{g_{512}}$. The results are: g_{556} = .479(91) , g_{434} = .396(46) and g_{374} = .389(36) These can be compared with the values .32(8), .33(3), .27(3) and .26(46), .32(6), .26(3) reported by Heestand[H2] and Agnihotry[A4] for the g factors of the 556, 434, and 374 kev states.

C. $Fe_{85}Pt_{15}$ ALLOY

Plots of $\frac{\Delta\theta}{g}$ vs τ are presented in Figure 5-9 for 7 Mev alpha and 35 Mev ^{16}O projectiles. (The value for the 329 kev state and 20 Mev ^{12}C projectile is also included. The intercepts extracted from these data are plotted in Figure 5-9. For the 7 Mev α data, the intercept is seen to agree with the theoretical prediction within experimental error. For the 35 Mev ^{16}O data, the experimental value of the intercept exceeds the theoretical prediction, in spite of the large error bar on the experimental point.

The static field values show a substantial increase from 7 Mev alpha to 35 Mev ^{16}O projectile. The value for 35 Mev ^{16}O ($H_{static}^{average}$=-1300±390 kGauss) is consistent with the NMR value measured by Kontani[K5] in dilute alloy at liquid helium temperature (1280±25 kGauss) while the value for 7 Mev alpha projectile ($H_{static}^{average}$ =-768±170 kGauss) is not.

There is a considerable spread in the values of the internal field for Pt in Fe reported in different measurements. Kontani[K5] quotes the most precise measurement using spin-echo NMR on < 1% Pt in iron at 4.2°K (H_{int} = -1280(25)kGauss). This is the value most often quoted. Ho and Phillips[H4] obtained 1390 kGauss (no error quoted) using a specific heat measurement on 3.2% in iron. Buyrn and Grodzins[B10] measured 1350±50 kGauss using Mossbauer effect on dilute alloy. Agresti et al[A8] measured 1190±40 kGauss using Mossbauer effect on 3% Pt alloy and Atac et al[A9] measured 1240±150 kGauss using Mossbauer. Benczer-Koller[B12] et al. used Mossbauer effect to measure the internal field on Pt in iron using concentrated (10%, 30%, 50% Pt in iron) alloys; they also used X-ray diffraction to investigate the lattice structure. While they could only determine that $-1.2 \leq H_{int} \leq -2.9$ MGauss, their X-ray studies revealed a b.c.c. lattice with lattice parameters midway between the lattice parameters of the b.c.c. Fe lattice and f.c.c. Pt lattice; the $Fe_{70}Pt_{30}$ and $Fe_{50}Pt_{50}$ alloys had disordered structures. Following Beraud[B11] et al, the accepted mean value for $\lesssim$ 3% Pt, from the above measurements, was taken to be 1270± 25 kGauss.

It is not possible to make the observed average static field for 7 Mev alpha and 35 Mev ^{16}O projectiles in our experiments agree simultaneously with previous measurements of the internal field on platinum in iron. The oxygen value agrees with the above value, while the 7 Mev alpha measurement does not. If the alloy were completely random, then the average static field would scale with the iron concentration. So in a random alloy, one might reasonably expect the average static field to be $\sim$ 15% smaller than for a dilute alloy. Figure 4-4 indicates that for our experiment, the $Fe_{85}Pt_{15}$ alloy was magnetized only to about 83% of full room-temperature magnetization. In this case, one might expect the average static field to be .83 of the value appropriate to full magnetization. If one scales the 7 Mev alpha value for the average static field by .85×.83 = .705, one can almost obtain agreement with the value 1270±25, but then the average static field for the oxygen data is high with respect to this value.

One can postulate several possible explanations for the change in static field between 7 Mev alpha and 35 Mev ^{16}O projectiles. One possible explanation is that radiation reduces the average observed field in the case of alpha particle bombardment. It will be recalled that the damage density is greatest for high current runs with low energy projectiles. To check for possible changes in the observed rotation angle, as a fraction of beam dose, the measured quantity $\frac{Q-1}{Q+1}$ was monitored as a function of beam dose for the experiment employing

7 Mev alpha particles on $Fe_{85}Pt_{15}$. The results are displayed in Fig. 6-4. They indicate that, within experimental error, the value of $\frac{Q-1}{Q+1}$ is consistent with the final value throughout the course of the experiment. If accumulated radiation damage is responsible for a dramatic reduction in the observed static field for this experiment, the effect of the damage must grow with a time constant that is very short compared to the duration of the experiment. This conclusion is inconsistent with the crude calculations of Chapter II, which indicate that even after 1 day of continuous bombardment, the average damage density is still likely to be $\lesssim$ 1-5%. It is felt that radiation damage effects are not able to account for the large change in average static field between 7 Mev alpha and 35 Mev ^{16}O bombardments.

Another possible explanation of the change in average "static" field is related to the proximity of the Coulomb excited atoms to the surface of the target. Ion implantation implants atoms within 100 to 200 Å of the surface; in this case, the measured field has been shown to be sensitive to the thickness of the oxide layer on the target surface. For Coulomb excitation with ^{16}O, the excited atoms are distributed with decreasing probability over a region of the order of 5-10 microns (5 to 10 $\times$ 10^4 Å). This case is likely to be free of surface oxide effects, but one cannot discount the effect of surface domains; in iron, it is known that the domains at the surface of the specimen prefer to align themselves

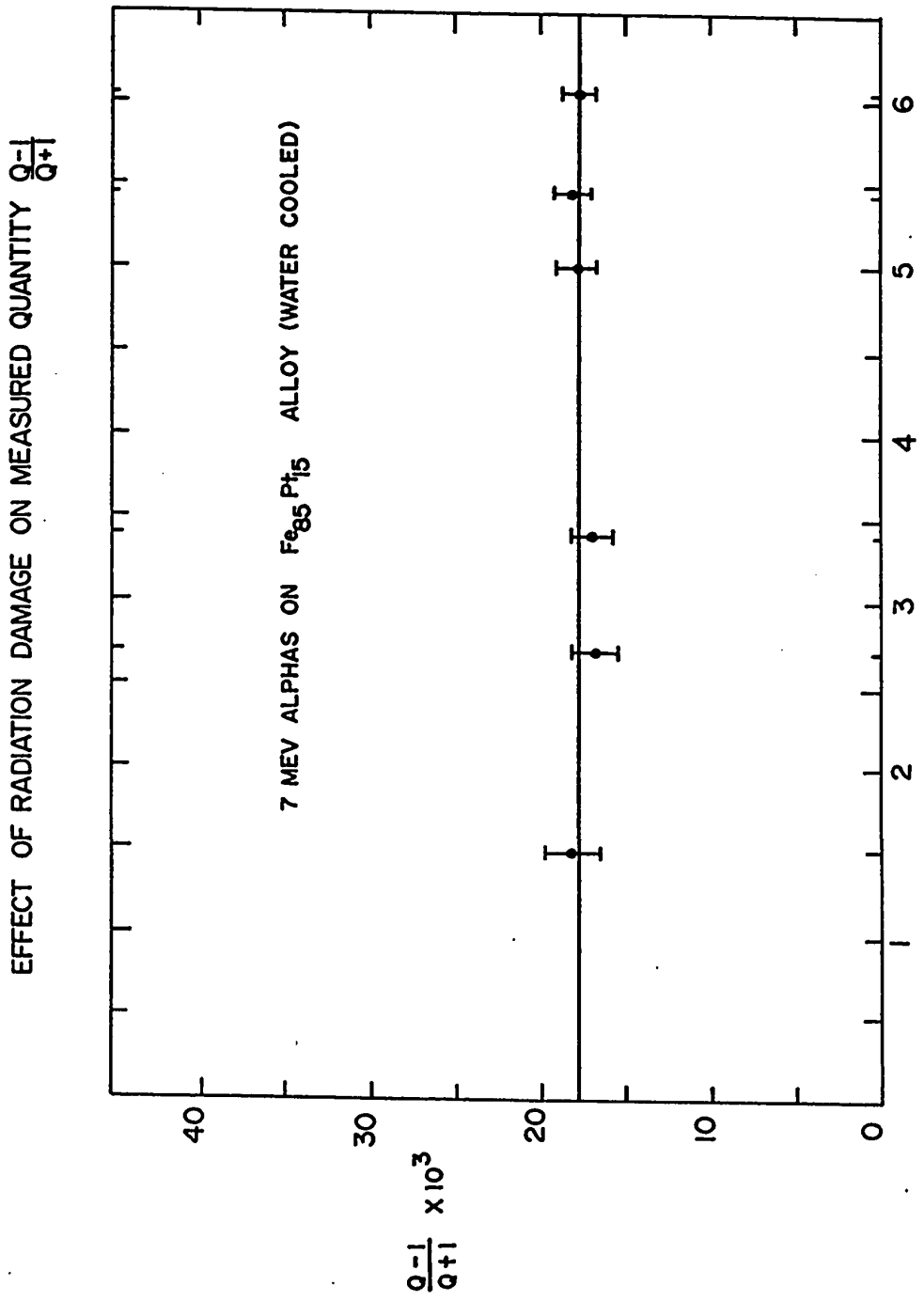
EFFECT OF RADIATION DAMAGE ON MEASURED QUANTITY $\frac{Q-1}{Q+1}$
7 MEV ALPHAS ON $Fe_{85}Pt_{15}$ ALLOY (WATER COOLED)
$\frac{Q-1}{Q+1} \times 10^3$
0
10
20
30
40
1
2
3
4
5
6
BEAM DOSE (MICROAMP - HOURS)

Figure 6-4

perpendicular to the surface. These domains are particularly difficult to magnetize.

This effect would be expected to be more serious for 35 Mev ^{16}O projectiles than for 7 Mev alpha projectiles (Fig. 2-2), so it is difficult to see how it could explain why the field for ^{16}O projectile is <u>larger</u> than for 7 Mev alpha projectile. A typical dimension for a surface domain in iron is 10 microns, so the fact that the surface magnetization differs from the bulk magnetization cannot be ruled out as a possible cause of the observation of low average static fields. Still another possible explanation of different observed field values is the difficulty of aligning the internal field at an impurity site with the external field when the impurity atom is significantly larger or smaller than the iron atom[A10]. This difference in size is most serious for Pt in iron (as opposed to rhodium or palladium in iron). The effect is dubbed the conical field effect because field directions at the impurity site define a cone about the direction of the external field with an opening angle of anywhere from 0 to 30° depending upon the case considered. Such a conical field effect at the impurity site would not show up in a bulk magnetization measurement. While such an effect can reduce the observed average static field in an alloy, it is difficult to decide how this effect could be related to a change in average static field for different projectiles.

A final possible explanation of the change in average

static field is related to the possibility that the "alloy" is not homogeneous. If the "alloy" contained microscopic platinum-rich regions, then most of the Coulomb excited platinum atoms would come from these regions. If the recoil velocity following collision with an alpha particle were not sufficiently large, then the atom, after coming to rest, could still find itself in the same platinum-rich region, with a correspondingly low internal field at the platinum sites; if the recoil velocity for ^{16}O bombardment were large enough to drive the Coulomb-excited atoms out of the platinum-rich region, they would find themselves in an iron rich region, with a correspondingly higher internal field. Since no investigation of the homogeneity of the $Fe_{85}Pt_{15}$ alloy was carried out, this final explanation must reside in the realm of speculation. It would, however, account qualitatively for the observed change in average static field.

In view of the apparent changes in average observed static field for $Fe_{85}Pt_{15}$ and (possibly) for $Fe_{80}Rh_{20}$ alloys, some comments on the strucutre of these alloys are in order.

D. ALLOY CRYSTAL STRUCTURE

(i) $Fe_{80}Rh_{20}$: Shirane et al.[S2] have investigated the structure of iron-rhodium alloy both above and below 20 atomic per cent rhodium concentration using X-ray diffraction and Mössbauer effect. Below 20 atomic percent Rh, the preferred structure is body centered cubic (α phase) with Rh at the center of iron cubes. Above 20 atomic percent, the alloy prefers

to adopt the CsCl structure (α' phase); two distinct average hyperfine fields are observed at the iron nuclei. This result is interpreted in terms of two distinct sites for iron atoms in the CsCl structure. The cæsium chloride structure can be considered to be composed of two interpenetrating simple cubic sublattices. On one sublattice, only iron atoms are present; on the other sublattice, rhodium and iron atoms are distributed randomly. In this structure, a rhodium atom will always see 8 iron nearest neighbours. Chao et al.[C1] point out that the sharp transition from α to α' phase at 20 atomic percent rhodium concentration indicated on the phase diagram of Shirane et al. does not satisfy Gibbs' phase rule. To satisfy the phase rule, they propose a narrow region of mixed α and α' phase at 20 atomic percent concentration. However, for both α and α' phase, a rhodium atom should see 8 iron nearest neighbours, and thus the measured internal field should be the same as that measured for very dilute alloys. Kontani[K5], using NMR, has measured the internal field on Rh in iron-rhodium alloys with rhodium concentrations of from 0 to 50 atomic per cent; he observes an average internal field that is roughly constant within error over this range of concentration, a result that is consistent with the phase diagram of Shirane. One might conclude, therefore, that the measured internal field should correspond to that observed by Kontani. Figure 5-5

indicates that this is indeed the case for 6 to 9 Mev alpha particle bombardment and 35 Mev ^{16}O bombardment, for both water-cooled and liquid nitrogen-cooled targets. The measured field for 5 Mev alpha bombardment is slightly lower than Kontani's value for both target coolants. Of course, the degree of order in the alloy depends in large measure on its method of formation and its history of heat treatment prior to the experiment. For the $Fe_{80}Rh_{20}$ alloy, it is not known whether the alloy was allowed to cool slowly or whether it was annealed after formation.

(ii) $Fe_{85}Pt_{15}$: Kussman and Rittberg[K6] have investigated the phase diagram of the iron-platinum system. Berkowitz[B5] et al. have investigated the structure and magnetic properties of $Fe_{85.6}Pt_{14.6}$ alloy. The phase diagram indicates that at 15 atomic percent Pt, the equilibrium ordered phase is b.c.c. (α) phase up to 200°C, and non-magnetic γ phase above that temperature. In reference B5, the relative amounts of each phase were determined by X-ray diffraction measurements, and by magnetization measurements which make use of the fact that the different phases have different coercive forces. It was found that the 14.6 at.% Pt alloy, when quenched from 1000°C to 0°C contained 95% volume fraction of α phase, in a highly stressed condition. After 23 hours of heat treatment at temperatures between 500 and 1000°C, this volume fraction decreased to 70%. In our experiments, the temperature of the target was

estimated to be <70°C with water cooling. The alloy for our experiments was formed by allowing the melt to cool to room temperature over a period of 1 hour. No special heat treatment was applied to the target thereafter. The results of Berkowitz would support the view that any ordering that occurred would be α phase. Moreover, in our experiments, the temperature of the target was estimated to be < 70°C, with water cooling, so an α to γ phase transition is not favoured thermodynamically at this temperature. If the local temperature and effect of radiation damage favoured an $\alpha \rightarrow \gamma$ phase transformation for 7 Mev alpha particles, such a transformation could help to explain the low observed average static field.

D. COMPARISON WITH RESULTS OF OTHER WORKERS

In this section, the rotation angles measured by other workers for rhodium, palladium, and platinum in iron for a range of concentrations and using a variety of techniques will be compared with the rotation angles reported in this thesis. As well, experimental results of other workers that are relevant to the study of the velocity dependence of the transient field will be discussed briefly in relation to the present work.

In Tables 6-2, 6-3, and 6-4 is presented a summary of all rotation angles reported in the literature which are free of obvious errors like failure to correct for beam-bending.

(i) Rhodium in iron

Table 6-2 summarizes available data for rhodium in iron. Bhattacherjee et al.[B6] performed a singles experiment on $Fe_{95}Rh_{05}$ alloy using 5 Mev alpha particles. The rotation angles for the 357 kev state in the present work for 5 to 9 Mev alpha particle energy and both target temperatures are in good agreement with their value. The rotation angle for the 295 kev state is in agreement at 8 and 9 Mev alpha energy for both target temperatures. However, Bhattacherjee's rotation angle for the 295 kev state is larger than the rotation angles reported in the present work at 5, 6 and 7 Mev alpha energy, and the results, while not very different, do not quite agree within error. Szökefalvi-Nagy[S5] have performed a singles experiment using 2.5 Mev protons on a liquid-nitrogen-cooled $Fe_{97}Rh_{03}$ alloy target. The maximum

initial recoil velocity for this projectile is a factor of 2.8 lower than for 5 Mev alpha particles. The rotation angle for the 357 kev state is in agreement with the present results for 6, 7, 8 and 9 Mev alpha energy, and both target temperatures. The 5 Mev alpha results are low with respect to the proton result; the discrepancy is 7-10 milliradians. The results of Bhattacherjee and Szökefalvi-Nagy agree within error for both states.

Roney et al.[R1] have performed an IMPACT experiment using $\sim$ 35 Mev ^{16}O ions on a standard layered target. The rotation angles of both states agree with the current results within error for 35 Mev ^{16}O projectile on a water-cooled target. For both of these experiments using ^{16}O projectile, the rotation angles of both the 295 and 357 kev states are significantly lower than the corresponding quantities employing either alpha particles or protons as projectiles. As indicated in Figure 6-1, this discrepancy is adequately accounted for within experimental error by the transient field theory of Lindhard and Winther.

Taken collectively, the data of Table 6-2 would appear to indicate that the transient field effect is small for alpha particle and proton projectiles. Due to the uncertainty in the value of the 295 kev state's g factor, it is not possible at this time to present conclusive evidence for or against the proposal that the transient field falls abruptly to zero when the maximum initial recoil velocity is less than $\frac{V_o}{2}$. This proposal was presented in an earlier paper[C3] on the basis of an identical set of experiments performed by the McMaster group on

$Fe_{51.5}Rh_{48.5}$ alloy. This paper reported sharp changes in both transient and average static fields as the alpha projectile energy was varied from 5 to 10 Mev. Since the publication of that paper, two important developments have occurred. The first was the recognition of the need to account for indirect feeding of the 295 keV state. The data of reference C3 have been reanalyzed to take into account indirect feeding, and the reanalyzed results are presented in Figures 6-5 and 6-6. The second development was an experiment reported by Keszthelyi et al.[K9]; in this experiment, they bombarded FeRh targets of various Rh concentrations with 2.5 Mev protons and monitored the rotation angle of the 357 kev state in rhodium as a function of beam dose. The results for 15, 30, and 48.5 atomic percent rhodium alloy targets are plotted in Figure 6-7. For 15 and 30 atomic percent rhodium, the observed rotation angle did not change as the experiment proceeded. However, for 48.5% rhodium concentration, there is definite evidence that the measured rotation angle decreases significantly as a function of beam dose. Since transient field effects are expected to be small for proton projectiles, and the static rotation of this state is large, the data provide definite evidence that the observed average static field was decreasing as a function of beam dose. Since $Fe_{51.5}Rh_{48.5}$ alloy is highly ordered, the decay of the average static field with increasing beam dose was interpreted in terms of radiation damage to the target structure.

This experiment provides clear evidence that bombardment by the ion beam can affect the measured value of the average

Δθ VS PROJECTILE ENERGY

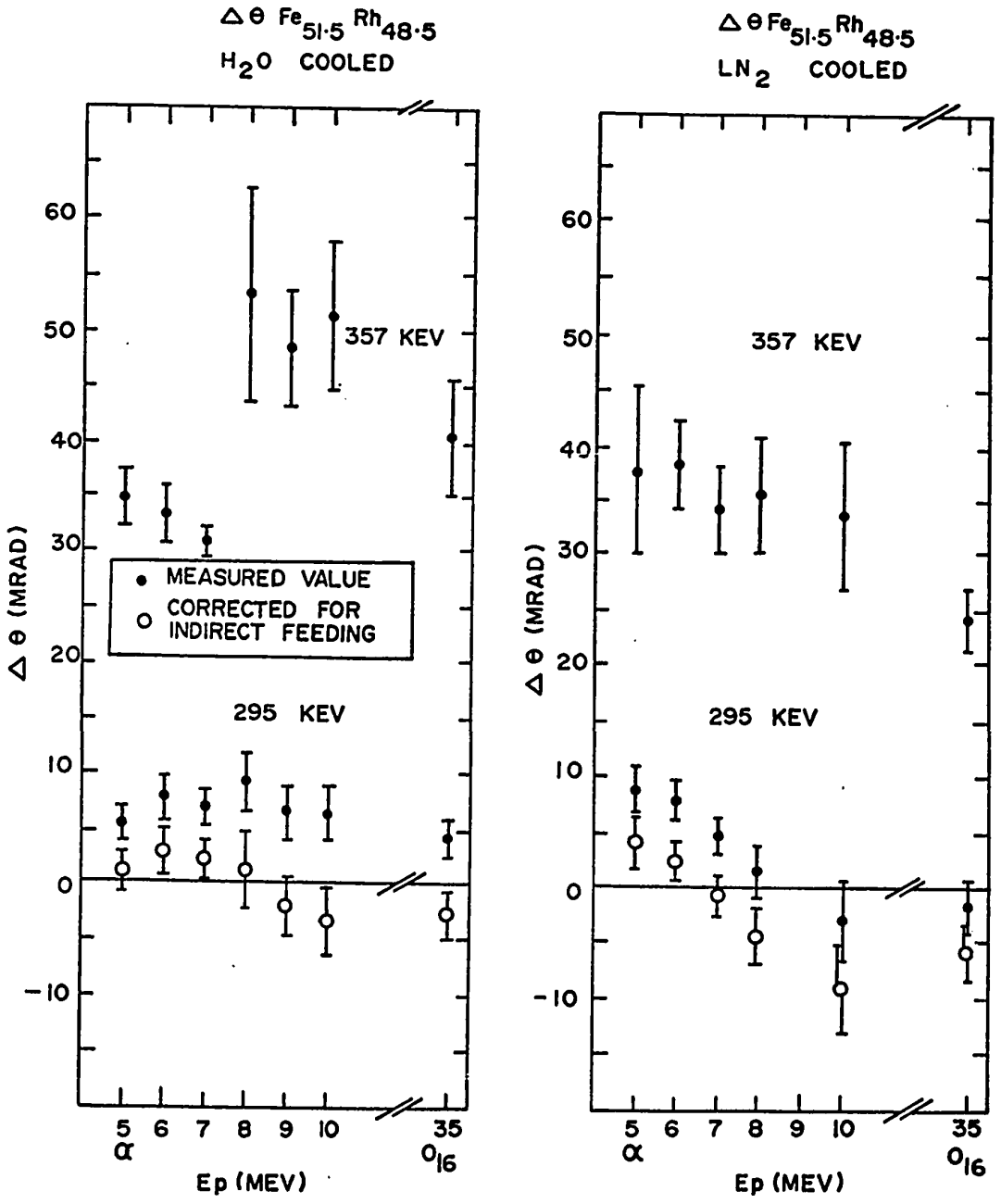

Figure 6-5

$Fe_{51.5}Rh_{48.5}$

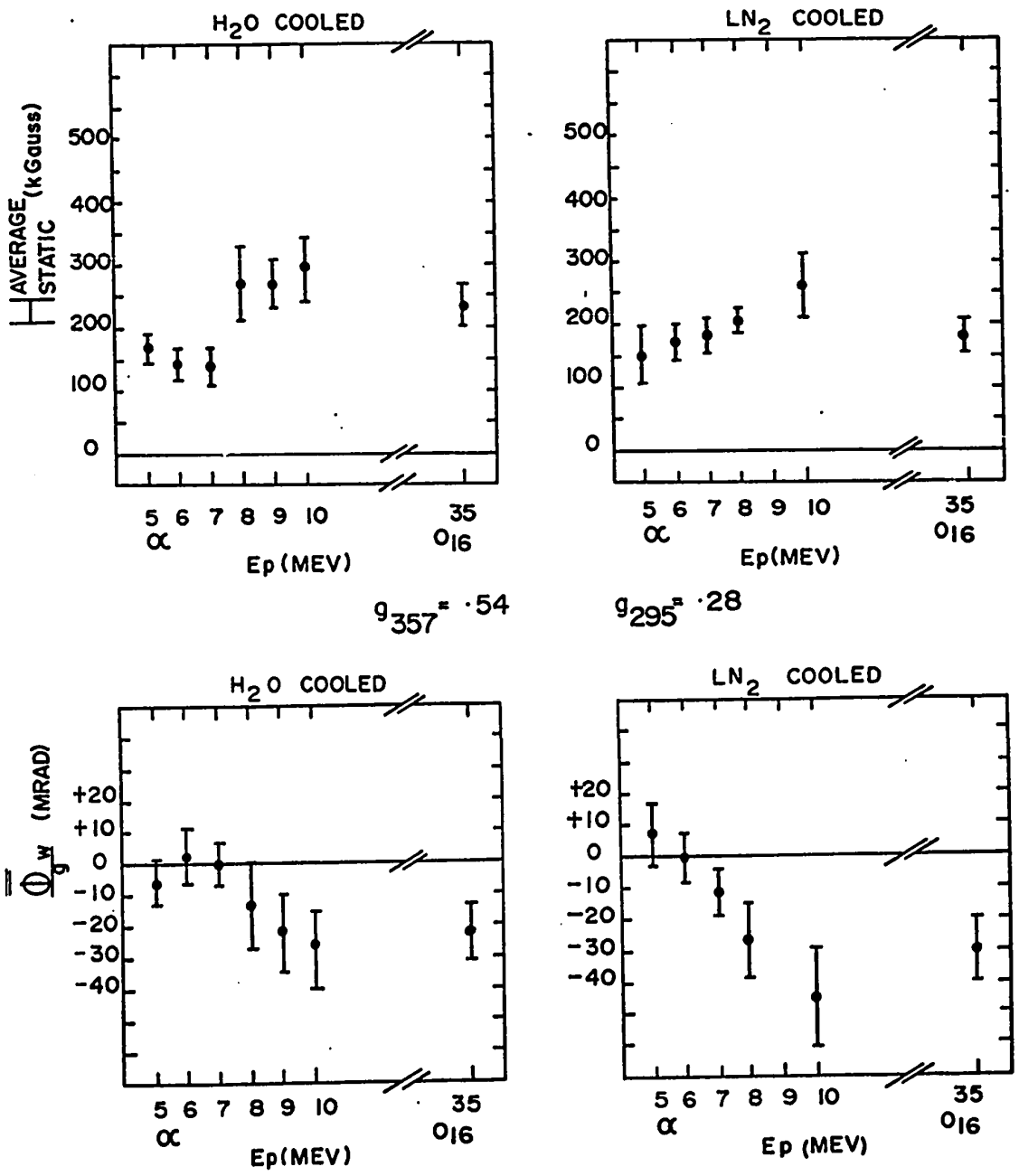

Figure 6-6

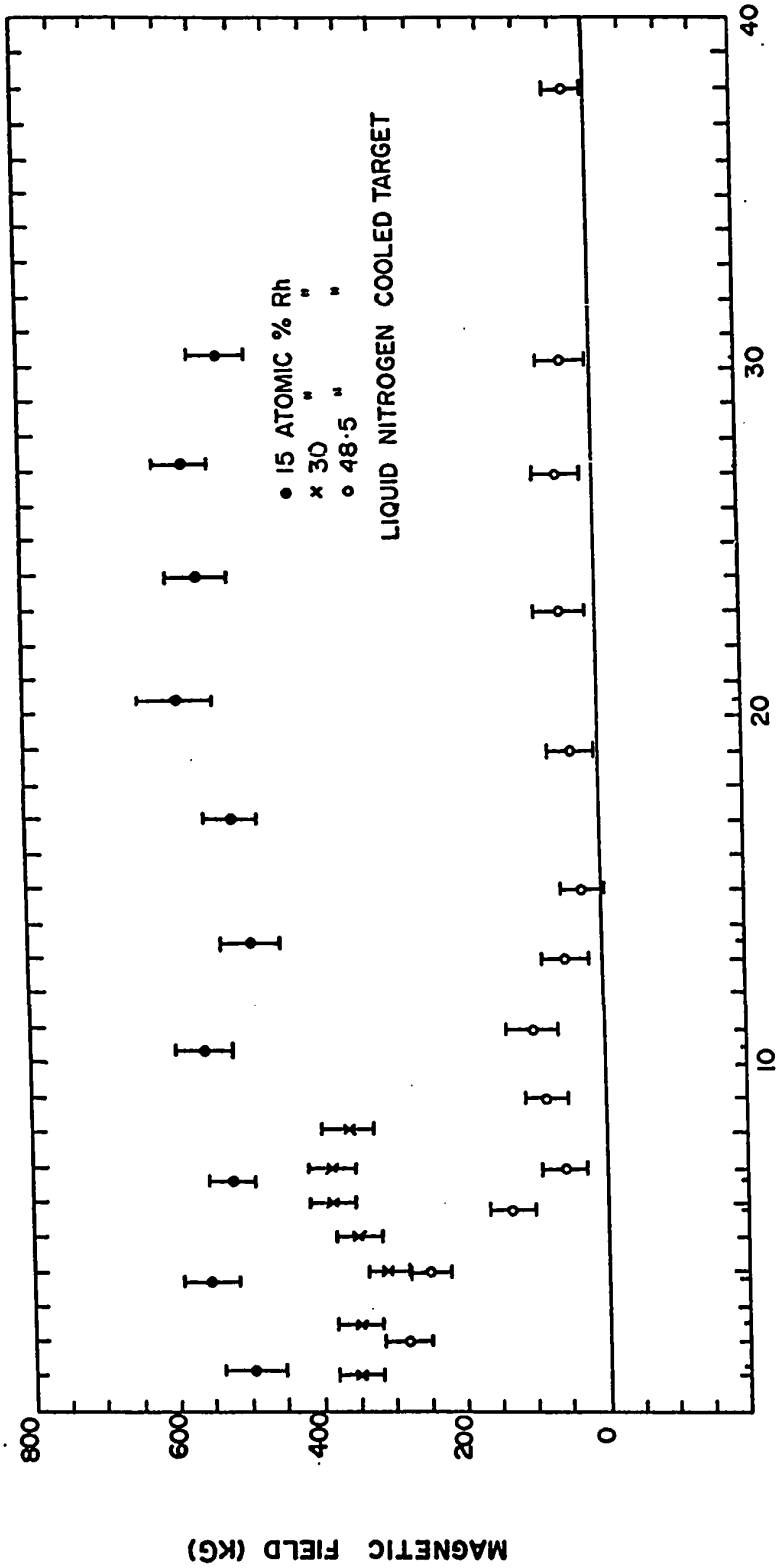
LIQUID NITROGEN COOLED TARGET
• 15 ATOMIC % Rh
× 30 "
○ 48·5 "
IRRADIATION DOSE (MC)
MAGNETIC FIELD (KG)
0
10
20
30
40
200
400
600
800

Figure 6-7

static field in an alloy (in the case of highly ordered FeRh alloy, the effect was to decrease the average field). The result makes the sharp changes in the "static" field for water-cooled $Fe_{51.5}Rh_{48.5}$ target reported in reference C3 understandable in terms of radiation damage. It will be recalled that the damage per Coulomb excitation event is greatest for the lowest energy projectiles. So any lowering of the static field due to radiation damage is most likely to occur at 5 and 6 MeV alpha energy; this is consistent with the observed increase in the static field from 5 to 9 Mev alpha energy. It is still puzzling why a sharp change is observed for a water cooled target but not for a liquid nitrogen cooled target, especially since the static field decay reported in reference K9 was for a liquid-nitrogen-cooled target.

Comparison of Figure 5-4 with Figure 6-5 indicates that the trend toward increasing transient field intercept in going from 5 to 9 Mev alpha energy is common to both experiments.

Finally, it must be noted that the magnetization as a function of applied field was not measured for this alloy; therefore it is possible that the target was not saturated by the external field; this could explain the low rotation angles measured for the 357 kev state and (possibly) the anomalous behaviour of the average static field.

(ii) Palladium in iron

Table 6-3 summarizes available data for palladium in iron. Agnihotry[A4] et al. have reported on experiment on $Fe_{80}Pd_{20}$ alloy using 5 Mev alpha particles. Their measured rotation angle for the 434 kev state in ^{108}Pd is in agreement with the results reported in this thesis for 6 and 7 Mev alpha energy, water-cooled-target and 8 Mev alpha energy, liquid-nitrogen-cooled target, but is low with respect to the current results at 8 Mev alpha energy, water-cooled-target and 6 and 7 Mev alpha energy, liquid-nitrogen-cooled target. The weighted average for 6, 7 and 8 Mev alpha energy and both target coolants exceeds Agnihotry's value by more than one standard deviation. For the 374 kev level in ^{110}Pd, the rotation angles reported in the present work agree with Agnihotry's value for all of the experiments using alpha projectile and liquid-nitrogen-cooled target. The weighted average for this state agrees well with Agnihotry's measurement.

Heestand[H2] has performed an IMPACT experiment using 35 Mev ^{16}O, and has obtained rotation angles for the 556, 512, 434 and 374 kev levels in $^{104,106,108,110}Pd$ respectively. His rotation angle for the 374 kev level agrees with the current values except for the 6 Mev alpha,liquid-nitrogen-cooled target experiment. The weighted average is in good agreement with his value. For the 434 kev state, Heestand's rotation angle agrees with all of the present experiments except for the 6 Mev alpha liquid-nitrogen-cooled target experiment. The weighted average in the present work agrees well with Heestand's value. For the

556 kev state, none of the values reported in the present work agree with Heestand's value. The discrepancy between Heestand's rotation angle and our weighted average value is 7 mrad (more than four standard deviations). A glance at Heestand's rotation angle for the ^{106}Pd 512 kev state indicates that it is considerably lower than the radioactivity results ($\sim$ 13 mrad). The transient field effect can account for these low rotation angles for the 556 kev and 512 kev states in the case of ^{16}O projectiles; one is then led to wonder why the rotation angles for the 374 kev and 434 kev states do not show a similar drop in rotation angle with respect to the alpha particle results. The answer can be found by referring to Figure 6-8. It is evident that the average static field for the ^{16}O bombardment and recoil into pure iron (IMPACT) is larger than the average static field for recoil in $Fe_{70}Pd_{30}$ alloy in which 3 out of every 10 atoms is a Pd atom. For the 374 and 434 kev states, the transient field effect for ^{16}O bombardment and recoil into pure iron is approximately compensated by the lower average static rotation for alpha bombardment of a 30% Pd alloy target.

(iii) Platinum in iron

Table 6-4 summarizes available data for platinum in iron. Examination of this table does not reveal a readily recognizable relationship between the rotation angles measured in different experiments. However, a pattern emerges if $\frac{\Delta\theta}{g}$ is plotted vs τ for each of these experiments. The g factors of the 328, 239 and 356 keV levels in ^{194,195,196}Pt are all known with

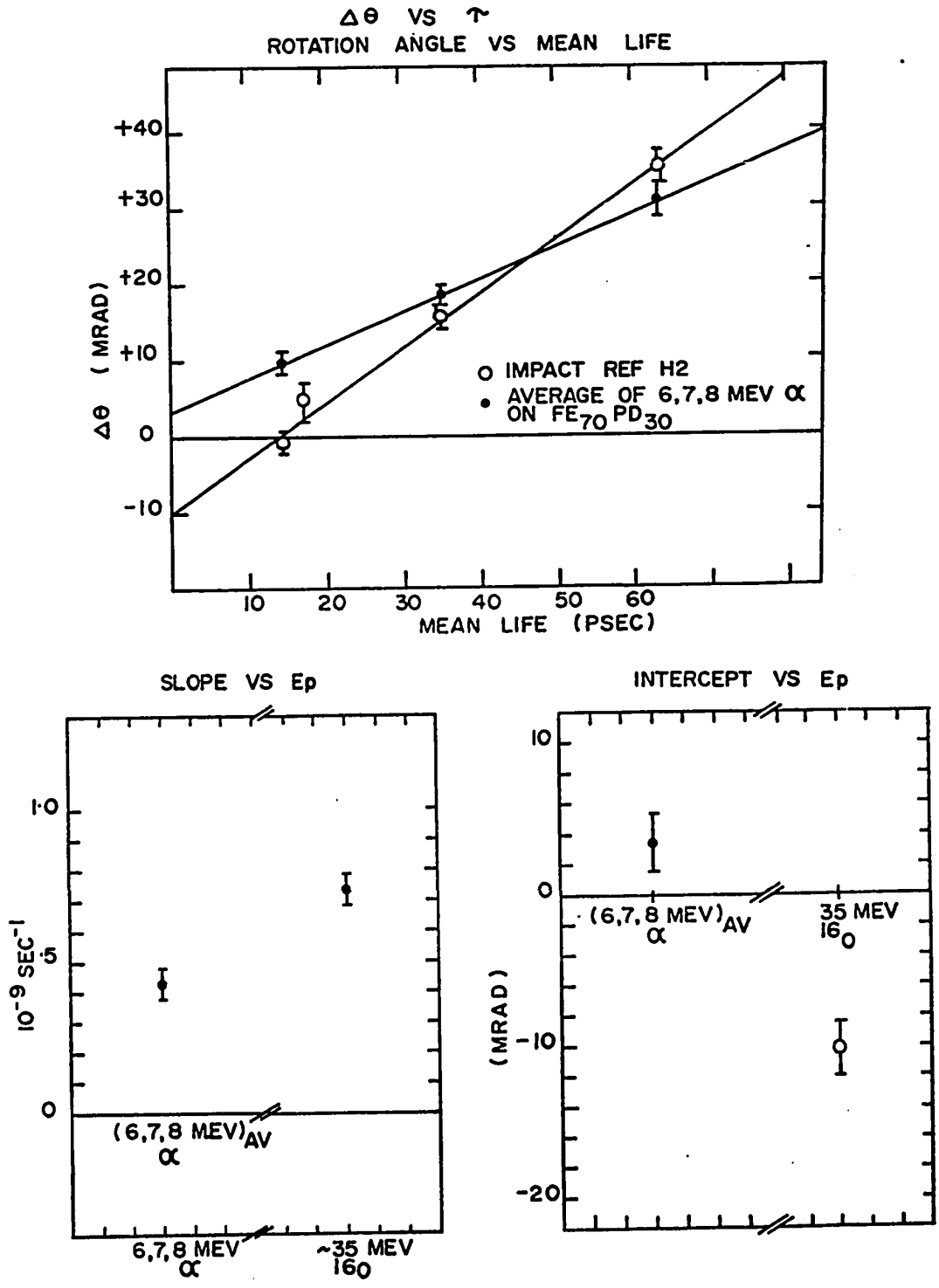
Δθ VS τ
ROTATION ANGLE VS MEAN LIFE
+40
+30
+20
+10
0
-10
Δθ (MRAD)
10
20
30
40
50
60
MEAN LIFE (PSEC)
O IMPACT REF H2
• AVERAGE OF 6,7,8 MEV α ON FE70 PD30
SLOPE VS Ep
1·0
·5
0
10⁻⁹ SEC⁻¹
(6,7,8 MEV)AV α
6,7,8 MEV α
~35 MEV 16O
INTERCEPT VS Ep
10
0
-10
-20
(MRAD)
(6,7,8 MEV)AV α
35 MEV 16O

Figure 6-8

an uncertainty of 6.2% or less, so dividing by the g factors does not seriously increase the uncertainty in the data points. Plots of $\frac{\Delta\theta}{g}$ vs τ for each experiment listed in Table 6-4 are presented in Figure 5-9; also in this figure is a plot of the average static field and transient field for each experiment extracted from the slope and intercept of the straight line that was least-squares fit to each set of data points.

From these data, it would appear that both the singles experiment on $Fe_{85}Pt_{15}$ alloy and coincidence (IMPACT) experiment using 35 Mev ^{16}O projectiles produce average static fields that are consistent with each other, and also equal within error to the field measured using a radioactive source. However, the average static field measured for the 7 Mev alpha singles experiment on $Fe_{85}Pt_{15}$ and the 2.5 Mev proton singles experiment on $Fe_{72.5}Pt_{27.5}$ are both low with respect to these values. The 2.5 Mev proton experiment on $Fe_{50}Pt_{50}$ alloy produces a higher average static field. If there is a consistency in these results, it is not obvious to the author; as a general conclusion, however, one can say that the data indicate that the measured average static field for Pt in Fe depends upon the choice of projectile and energy, as well as target composition.

(iv) Transient field experiments of special significance.

Since the first report of the transient field phenomenon, many experiments have been performed to study the effect. Three of the most important sets of data will be discussed briefly.

One may question whether the transient field phenomenon is in fact associated with the slowing down of the ion; two experiments are particularly relevant to this question. Herskind et al[H3] performed IMPACT experiments using triple layer targets. The first (thin) layer was the material to be Coulomb excited; the second layer was a (thick) copper layer of carefully controlled thickness, and the third (thick) layer was iron. The purpose of the copper layer was to provide an intermediate material through which the recoiling Coulomb-excited ions could pass without experiencing a coherent precession from hyperfine interactions; by varying the thickness of the copper layer, the initial velocity that the recoiling ion had <u>when it entered the iron</u> could be varied. The experimental results indicated that as the copper layer was increased in thickness, the rotation angle went from a negative value (for zero Cu thickness) to a value near zero for 500 $\mu gm/cm^2$ Cu thickness; when the copper thickness was further increased (to $\sim$750 μgm^2) the observed rotation angle was positive and in near agreement with radioactivity results. Finally, when the thickness of the copper layer was increased to $\sim$ 1 mg/cm^2, the observed rotation angle dropped back to zero. These results were interpreted as follows: As the copper thickness increased, the entry velocity <u>into iron</u> for the recoiling ion decreased. Thus, the negative transient rotation in iron experienced by the recoiling ion decreased with increasing copper thickness. At $\sim$ 500 $\mu gm/cm^2$, the transient and static rotations cancelled each other, yielding a null result; as the copper thickness was increased further, the transient rotation decreased even more,and what was

observed was almost entirely a positive static rotation, not far in value from the static rotation measured in a radioactivity experiment. As the copper thickness was increased still further, ($\sim$ 1 mg/cm^2) all of the ions stopped in the copper layer and never reached the iron layer; in this case, neither a transient nor static rotation was observed and the observed rotation angle was again zero. These results seem to indicate that the size of the transient field effect decreases as the entry velocity into iron decreases. They do not, however, preclude the possibility that the transient field effect persists after the ion has come to rest. One of the best pieces of evidence that the transient field effect imparts its full effect in a time comparable to the slowing down time of a recoiling ion is an IMPAC experiment performed by Heestand[H2] on germanium recoiling in iron. The internal field for dilute germanium in iron has been measured to be +70(3) kGauss. Because the internal field is so small, the static rotation is very small, so germanium in iron is a particularly favourable case for studying transient field effects. The results of the IMPACT experiment are consistent with a very small static rotation and a transient rotation of $\sim$ 11 milliradians for each of the 4 states studied in germanium; the first 2+ state in ^{70}Ge has a mean life of 1.92(.20) psec and sees the full transient effect. Therefore it can be concluded that the full transient effect is imparted in a time less than 2 psec.

The velocity dependence of the transient field can be studied simply by plotting the transient rotations measured in different experiments as a function of the initial recoil velocity

appropriate to each experiment. In an IMPACT experiment, one observes the integrated transient rotation directly. In this thesis, it has been demonstrated that the observed transient rotation in a singles experiment corresponds to a double average of ϕ_w over projectile scattering angle and target thickness. $\bar{\bar{\phi}}_w$ is not very different from ϕ_w in most cases; $\bar{\bar{\phi}}_w$ can be larger or smaller than ϕ_w depending upon how the b_2 coefficient behaves as a function of scattering angle. The principal difficulty in studying the velocity-dependence of the transient field is to find suitable combinations of target and projectile which will permit one to scan both high and low velocity regions. For most cases, only radioactivity results (zero velocity) and IMPACT results (high velocity) are available. This thesis has attempted to provide information on the systematic behaviour of the transient field at low recoil velocity.

A notable exception to the general lack of low-velocity experiments is provided by the case of iron recoiling in iron. The first excited state of ^{56}Fe is a 2+ state of 847 kev excitation energy, and mean life 10.4 psec. The rotation angle for this state has been measured by beta-decay[A7] and by resonance fluorescence[M2]; these results correspond essentially to zero recoil velocity. IMPACT experiments with 38.5 Mev ^{16}O ions and 9 and 7.5 Mev alpha particles[H2] have also been performed; as well inelastic proton scattering was carried out at 7.5 and 4.5 Mev proton energy (IMPACT)[H2] and 7.8 Mev proton energy (singles)[K11].

TABLE 6-5 Summary of Experiments on Iron Recoiling in Iron

Experiment	Incident Energy (Mev)	Maximum Recoil Energy (Mev)	Maximum Recoil Velocity ($\times 10^8$ cm/sec)	$\Delta\theta$ (mrad)	"ϕ" [$\Delta\theta$-8.9(2.0)] (mrad)	Reference
847 kev state in ^{56}Fe						
Resonance Fluorescence	-	0	0	8.0(2.0)	+0.9(2.0)	M2
β-γ-γ	-	10^{-4}	.019	9.8(2.0) Av=8.9(1.4)	-0.9(2.0)	A11
$^{56}Fe(pp'\gamma)^{56}Fe^*$ (singles)	7.8	0.54	1.37	+11(2)	+2.1(2.0)	K11
$^{56}Fe(pp'\gamma)^{56}Fe^*$ (coincidence)	4.5	0.28	0.98	+5.5(1.8)	-3.4(1.8)	H2
"	6.6	0.43	1.22	+2.0(3.0)	-6.9(3.0)	M7
"	7.5	0.49	1.30	+2.9(1.7)	-6.0(1.7)	H2
Coulomb Excitation (coincidence)						
alphas	9.0	2.1	2.69	+1.1(2.0)	-7.8(2.0)	H2
alphas	7.5	1.7	2.42	+1.1(3.3)	-7.8(3.3)	H2
^{16}O	38.5	23	8.91	+1.1(1.6)	-7.8(1.6)	H2
alphas (singles) ($Fe_{80}Cr_{20}$)	7.0	1.59	2.34	+6.5(0.9)	-0.3(1.5) [a]	K12

a) deduced from Mossbauer measurement of internal field at iron nuclei in $Fe_{80}Cr_{20}$ alloy (H_{int} = -277(42) kGauss).

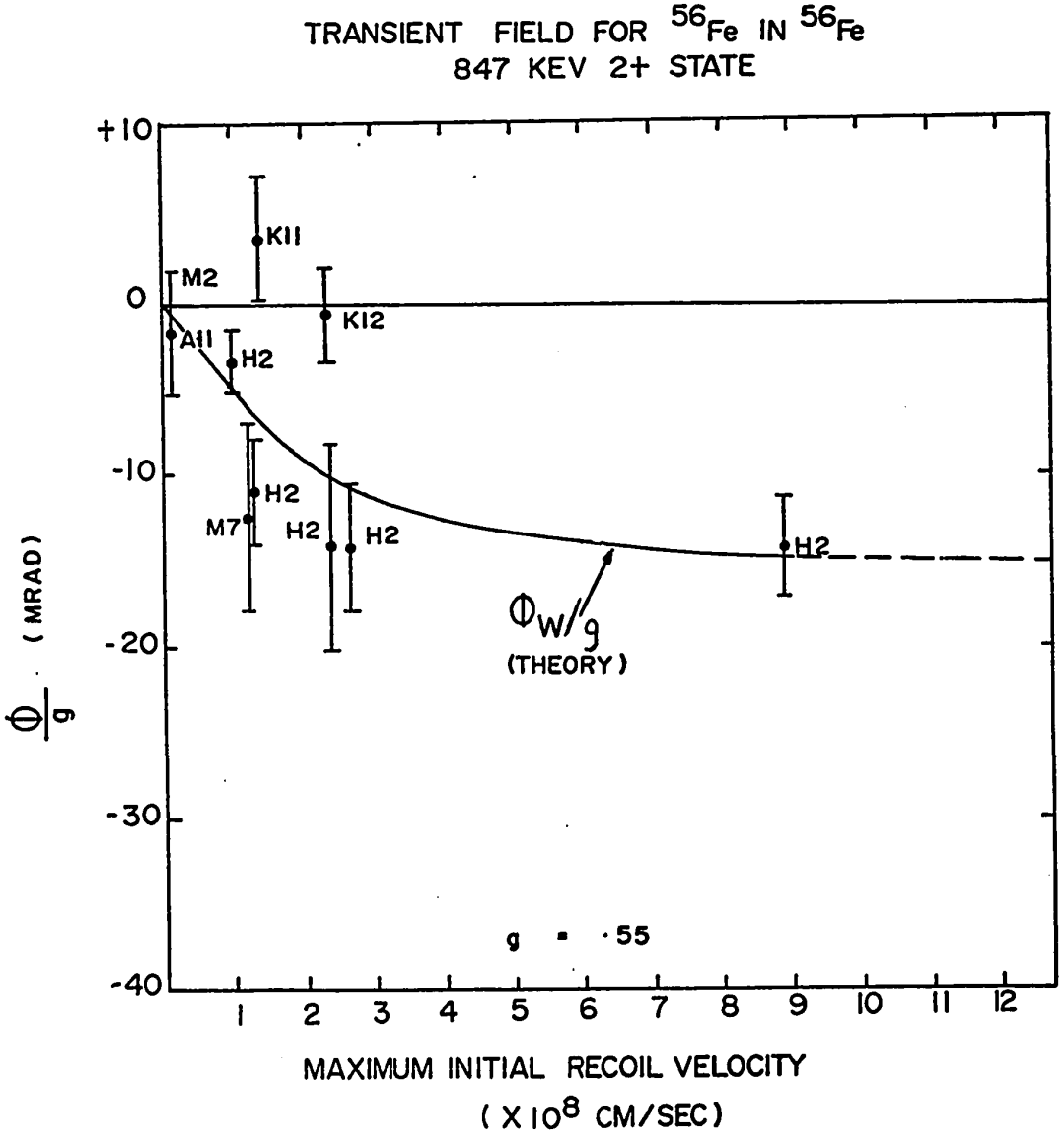
TRANSIENT FIELD FOR ^{56}Fe IN ^{56}Fe
847 KEV 2+ STATE
+10
0
-10
-20
-30
-40
K11
M2
K12
A11
H2
H2
M7
H2
H2
H2
$\Phi_{W//g}$
(THEORY)
g = ·55
1
2
3
4
5
6
7
8
9
10
11
12
MAXIMUM INITIAL RECOIL VELOCITY
(X 10^8 CM/SEC)
$\frac{\Phi}{g}$ (MRAD)

Figure 6-9

Kerr et al[K12] have measured rotation angles for states in ^{55}Fe using the $^{52}Cr(\alpha,n)^{55}Fe$ reaction at 7 Mev alpha bombarding energy. The measured rotation angles and the recoil energy for the various experiments are summarized in Table 6-5, and the data are plotted as a function of initial recoil velocity in Figure 6-9. Making the large assumption that the average static field is approximately the same for all of the experiments, and taking the beta decay and resonance fluorescence measurements to be pure static rotation, the transient field can be seen to grow as a function of recoil velocity in a manner that is well-described by the Lindhard-Winther theory.

CHAPTER VII

SUMMARY

This thesis has presented a study of the velocity dependence of the transient field phenomenon for concentrated alloys of rhodium (20 at %), palladium (30 at %), and platinum (15 at %) in iron. The experiments were performed using the singles perturbed angular distribution technique following Coulomb excitation. A detailed theoretical analysis of the experimental method was presented to describe how the transient field would modify the observed rotation angle. It was found that for the maximum initial recoil velocities appropriate to the experiments described in this thesis, the transient field rotation when averaged over projectile scattering angle and energy, was not very different from the un-averaged value that would be measured in an IMPACT experiment; the double-averaging can provide either a small amplification or small attenuation with respect to the un-averaged rotation, depending upon the projectile and energy considered. Using the transient field theory of Lindhard and Winther[L1], the size of the effect was calculated for the cases of interest. These calculated values were then compared with the experimentally-measured transient rotations as a function of the maximum initial recoil velocity appropriate to each experiment.

For the cases studied, the transient rotation at low velocity was smoothly-varying and was adequately described by the Lindhard and Winther theory. The transient rotations measured for 35 Mev ^{16}O projectiles agree within error with the same quantities measured using the IMPACT technique.

The analysis technique permitted the separation of the transient rotation (experienced while the ion was slowing down) and average static rotation (caused by the average internal field seen after the ion has come to rest). In the case of the platinum alloy, the average internal fields measured under 35 Mev ^{16}O and 7 Mev alpha particle bombardment were significantly different, only the ^{16}O value being consistent with the internal field measured for dilute Pt in iron. Comparison with the results of other workers (Figure 5-9) indicates that not all recoil implantation experiments on Pt in Fe measure the same average internal field. This result emphasizes one of the basic difficulties in using recoil implantation techniques (IMPACT and singles) for g-factor measurements: the lack of knowledge of the value of the average internal field. The results presented in this thesis would indicate that this average internal field can be a function of projectile type and energy as well as of alloy composition.

In the course of the experimental program, it was noted that, in the odd-A isotopes (^{103}Rh, ^{195}Pt), the measured rotation angle of the 3/2- state could contain a component that was due to indirect feeding from the higher-energy 5/2- state. The

theory of the effect of indirect feeding on the measured rotation angle has been worked out for the case of coincidence (IMPACT) and singles experiments. The g factor of the 211 kev state in ^{195}Pt has been remeasured, with corrections for indirect feeding, using the data collected for 7 Mev alpha particle projectiles on an $Fe_{85}Pt_{15}$ target. A value of $g_{211} = .164(66)$ was obtained, in general agreement with previous measurements[V1,K7*]. Only one of these authors has accounted for the effect of indirect feeding[V1]. All of the measurements are in disagreement with the theoretical prediction of Gal[G2] (-.02) based on the core-excitation model.

Indirect feeding corrections were also made to the 295 kev level in ^{103}Rh; at 6 to 9 Mev alpha projectile energy, it was found that almost all of the observed rotation of the 295 kev state is contributed by the indirect feeding component from the 5/2- 357 kev level. If one believes the theoretical prediction of the size of the transient field effect for this experiment ($\sim$ 1 mrad for g = .25), then the data are consistent with a very small g factor for this state.

From the average of 6, 7 and 8 Mev alpha particle bombardment of $Fe_{70}Pd_{30}$ alloy, g factors of the first 2+ states of 556, 434 and 374 kev in $^{104,108,110}Pd$ respectively were measured using an analysis which assumed that the transient field correction was

---

* (Varga et al.[V1], $g_{211} = .104(21)$; Kugel et al[K7], $g_{211} = .16(6)$.

negligible and that the g factors were close in value to the measured g factor of the 2+ 512 kev state in ^{106}Pd. The measured g factors were: $g_{374} = .389(36)$; $g_{434} = .396(46)$; $g_{556} = .479(91)$

A. SUGGESTIONS FOR FURTHER EXPERIMENTS

From the experiments reported in this thesis, several experiments suggest themselves.

Since the interpretation of the $Fe_{80}Rh_{20}$ data depends to some extent upon a more precise knowledge of the g factor of the 295 kev state than is currently available, a measurement of the g factor of this state is highly desirable. A radioactivity measurement of the g factor of this state is a possibility. ^{103}Pd, with a half-life of 17 days, decays to ^{103}Rh with a .07% branch to the 357 kev state. Assuming that the 62 kev (5/2-, 357 kev) to (3/2-,295 kev) transition is pure M1,the angular distribution for the 5/2-(M1) 3/2-(M1+E2) 1/2- cascade is very anisotropic. Calculations indicate that, for a reactor flux of $\sim 1.5 \times 10^{14}$ n/cm^2, and 10 mg of natural Pd, sufficient source activity could be produced to permit a radioactivity perturbed angular correlation experiment on the 295 kev state to be performed in 3 to 4 weeks of counting time.

It would also be desirable to repeat Coulomb excitation on $Fe_{80}Rh_{20}$ alloy at 5 Mev alpha energy and 8 or 9 Mev alpha energy, taking the time necessary to accumulate excellent statistics so that it can be determined whether the possible trend toward increasing average static field and increasing (negative) transient rotation with increasing beam energy is statistically significant.

For the $Fe_{70}Pd_{30}$ alloy, it would be desirable to carry out a bombardment with 35 Mev ^{16}O ions to check whether the average static field increases with respect to the value observed with 7 Mev alpha particle projectiles, as is the case with the $Fe_{85}Pt_{15}$ alloy.

For each of these experiments, it would be highly desirable to monitor $\frac{Q-1}{Q+1}$ as a function of beam dose to check that the internal field does not decay as the run proceeds. To do so, it is only necessary to divide the total run time up into segments and to treat each segment as an individual measurement of $\frac{Q-1}{Q+1}$ (i.e. zero counts at the beginning of each time interval, and an interval that is of sufficient duration to make the statistical error on $\frac{Q-1}{Q+1}$ small enough for the results to be meaningful).

APPENDIX A

CORRECTIONS FOR BEAM-BENDING

As the beam of charged particles enters the magnetic fringing field of the electromagnet, it is bent in a curved path in the horizontal plane by the transverse component of the magnetic field. This shifts the position of the point at which the beam strikes the target (beam shift) and also alters the angle at which it strikes the target (beam rotation). Since the change in count-rate caused by these effects can be comparable to the changes caused by the perturbation of the angular distribution, it is important to be able to correct the data to account for their effect.

A diagram of the situation is presented in Fig. A-1. With reference to this figure, the angle through which the beam is rotated is given by $\Delta\theta = \beta$. Since the angle α is very small, it is given approximately by $\alpha \approx \frac{y}{r\sqrt{2}}$; the fractional change in distance from the detector is given by $\frac{r'-r}{r} = \frac{\Delta r}{r} \approx \frac{y}{r\sqrt{2}}$. The count rate N at the detector will change because (1) the point at which the beam spot strikes the target will be moved nearer or farther from the detector by a fractional amount $\frac{\Delta r}{r}$ and (2) the quantization axis will effectively be rotated through angle β.

The situation for field reversed can be obtained by

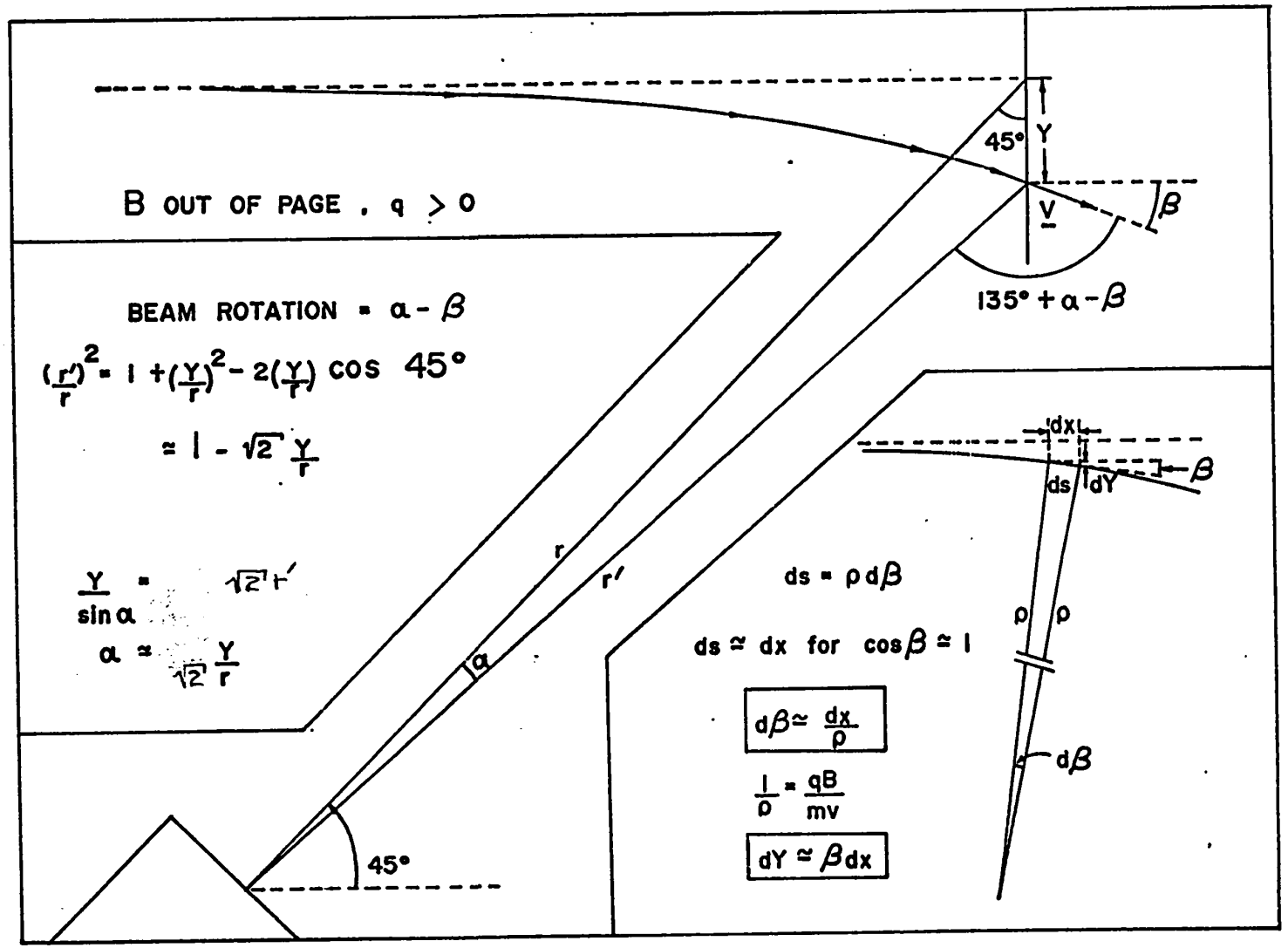

Figure A-1 Beam -Bending Geometry

rotating diagram A-1 through 180° about the undeviated beam axis. If the number of counts for field up in a given counter at 135° is

$$N(+) = N_{\text{undeviated}}\left[\left(\frac{r+\Delta r}{r}\right)^2 - \bar{b}_4 + 2\bar{b}_2(\alpha-\beta)\right]$$

then $$N(-) = N_{\text{undeviated}}\left[\left(\frac{r-\Delta r}{r}\right)^2 - \bar{b}_4 - 2\bar{b}_2(\alpha-\beta)\right]$$

and

$$\frac{Q-1}{Q+1} = \frac{\sqrt{2}\,\frac{Y}{r} + \bar{b}_2\left[\sqrt{2}\,\frac{Y}{r} - 2\beta\right]}{(1 - \bar{b}_4)} \qquad \text{(A-1)}$$

where r is the detector-to-target distance.

The negative of the above expression is the correction that must be applied to the quantity $\frac{Q-1}{Q+1}$ to account for beam-bending.

The angle β turned through can be found using the small angle approximation $\sin\beta \approx \beta$. For a distance dx along the x axis, the angle turned through is given by $d\beta \approx \frac{dx}{\rho}$, where ρ is the radius of curvature for the point x, defined by $\frac{1}{\rho} = \frac{qB(x)}{mV_o}$. Thus

$$\beta(x) = \frac{q}{mV_o}\int_{-\infty}^{x} B(x)\,dx$$

and

$$\beta = \beta(o) = \frac{q}{mV_o}\int_{-\infty}^{o} B(x)\,dx.$$

The beam shift y can be found by noting that $\frac{dy}{dx} \approx \beta(x)$ in the small angle approximation.

So

$$dy = \beta(x)dx \text{ and } Y = \int_{-\infty}^{0} dx \int_{-\infty}^{x} B(x')dx' \ .$$

The integrals $\int_{-\infty}^{0} B(x)dx$ and $\int_{-\infty}^{0} dx \int_{-\infty}^{x} B(x')dx'$ can be evaluated numerically once the profile of the transverse magnetic field B as a function of radial distance x from the centre of the pole tip has been measured. The profile for the electromagnet and pole-gap used in the experiments is shown in Fig.A-2 The beam profile was measured using a Hall probe calibrated against the analyzing magnet of the tandem accelerator. The measured field was accurate to at least 2% over the entire range of measurement. The detector-to-target distance varied slightly from one experiment to the next, but was $\sim$ 50 mm. for all of the experiments. There was a 1% error in this distance measurement.

The beam-bending corrections calculated in this way are listed in Table 5-1 . For the heavy projectiles, ^{12}C and ^{16}O, it was found that the corrections were not negligible.

It is to be noted that the magnitude of the beam-bending correction depends upon the $\bar{b}_2$ coefficient. For back angles, the beam shift and beam rotation corrections are opposite in sign for positive $\bar{b}_2$ coefficients, and add for negative $\bar{b}_2$ coefficients.

A direct measurement of the beam-bending correction was made by carrying out a perturbed angular distribution run using

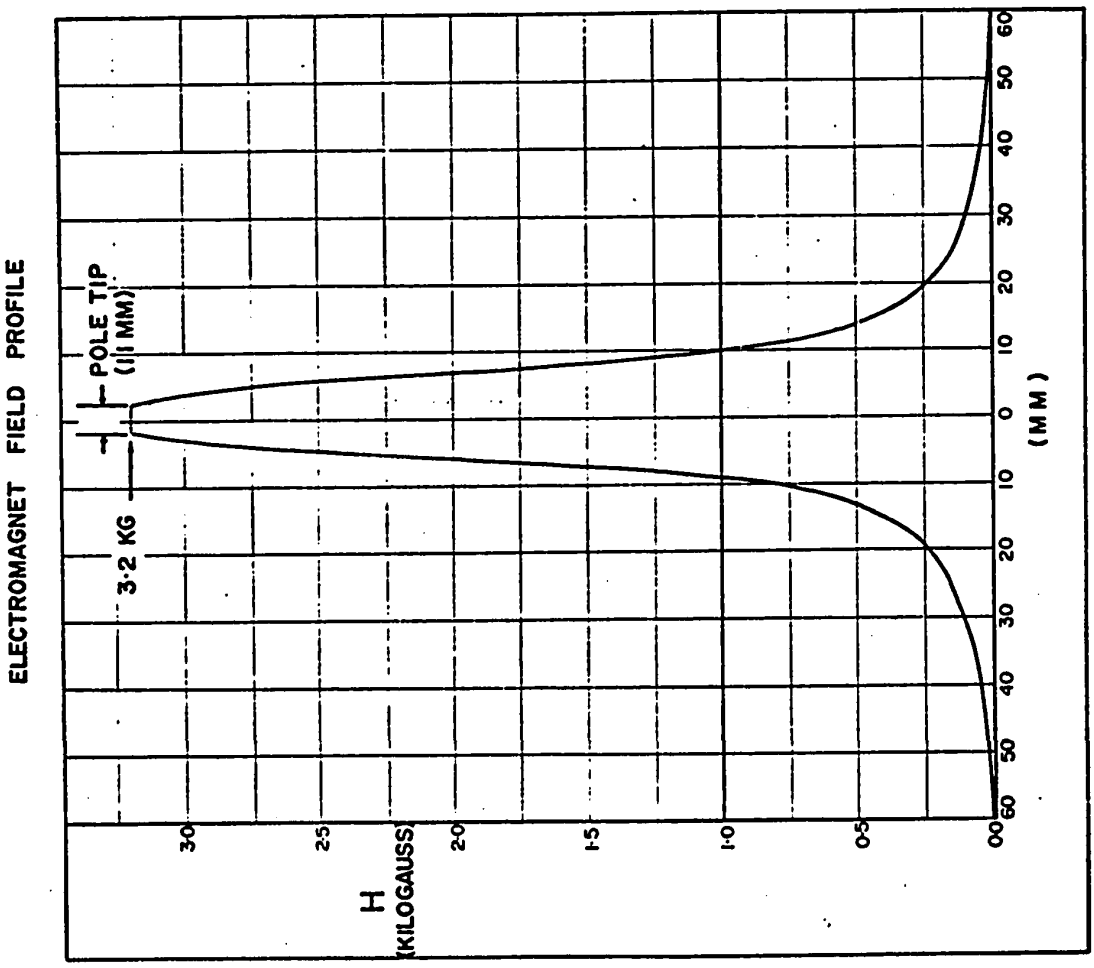
ELECTROMAGNET FIELD PROFILE
POLE TIP
(11 MM)
3·2 KG
H
(KILOGAUSS)
3·0
2·5
2·0
1·5
1·0
0·5
0·0
0
10
20
30
40
50
60
(MM)
RADIAL DISTANCE FROM POLE-TIP CENTRE

Figure A-2

the $^{52}Cr(\alpha,n)^{55}Fe$ reaction with 7 MeV α's; since the chromium target is non-ferromagnetic, any non-zero value measured for $\frac{Q-1}{Q+1}$ must be due solely to beam-bending. This particular reaction was chosen because 3 levels populated in ^{55}Fe - 411, 477 and 931 keV have a nice spread in b_2 values: 0.0, -.208(11) and +.080(5) respectively. According to eq. A-1, a plot of $\frac{Q-1}{Q+1}$ vs b_2 should be a straight line with slope $\sqrt{2}\,\frac{Y}{r} - 2\beta$ and intercept $\sqrt{2}\,\frac{Y}{r}$. The measured values agreed very well with the calculated values within experimental error; the errors in the calculated values and measured values of $\frac{Q-1}{Q+1}$ were 5% and 15%, respectively.

APPENDIX B

INDIRECT FEEDS OF COULOMB-EXCITED LEVELS

A. MODIFICATION OF ANGULAR DISTRIBUTION COEFFICIENTS

Consider a general 3-level scheme (Fig. B-1). Each excited level can be directly populated by E2 Coulomb excitation. In addition, the upper level (A) decays in part directly to the ground state and in part to the lower excited state (B) by gamma-ray emission and internal conversion. It is desired to find the effect of this indirect feeding of level (B) on the measured precession angle for level (B).

The direct excitation and de-excitation can be considered from the point of view of the equivalent gamma-gamma cascade. The process can be summarized by: $I_g(E2)I_B(E2+M1)I_g$.

The angular distribution coefficient A_2 for this process is given by (direct) $A_2^d = A_2^{(1)}A_2^{(2)}$ where

$$A_2^{(1)} = F_2(I_B,I_G,2,2) \cdot a_2^{E2}(\xi_B,\theta_p)$$

and

$$A_2^{(2)} = \frac{F_2(I_B,I_G,1,1) + 2\delta_2 F_2(I_B,I_G,1,2) + \delta_2{}^2 F_2(I_B,I_G,2,2)}{1 + \delta_2{}^2}$$

where $\delta_2{}^2$ = Intensity (E2)/Intensity (M1)

The indirect process can be viewed in terms of the equivalent γ-(γ)-γ cascade (i.e. a triple cascade in which the intermediate radiation is undetected). This process can be summarized by:

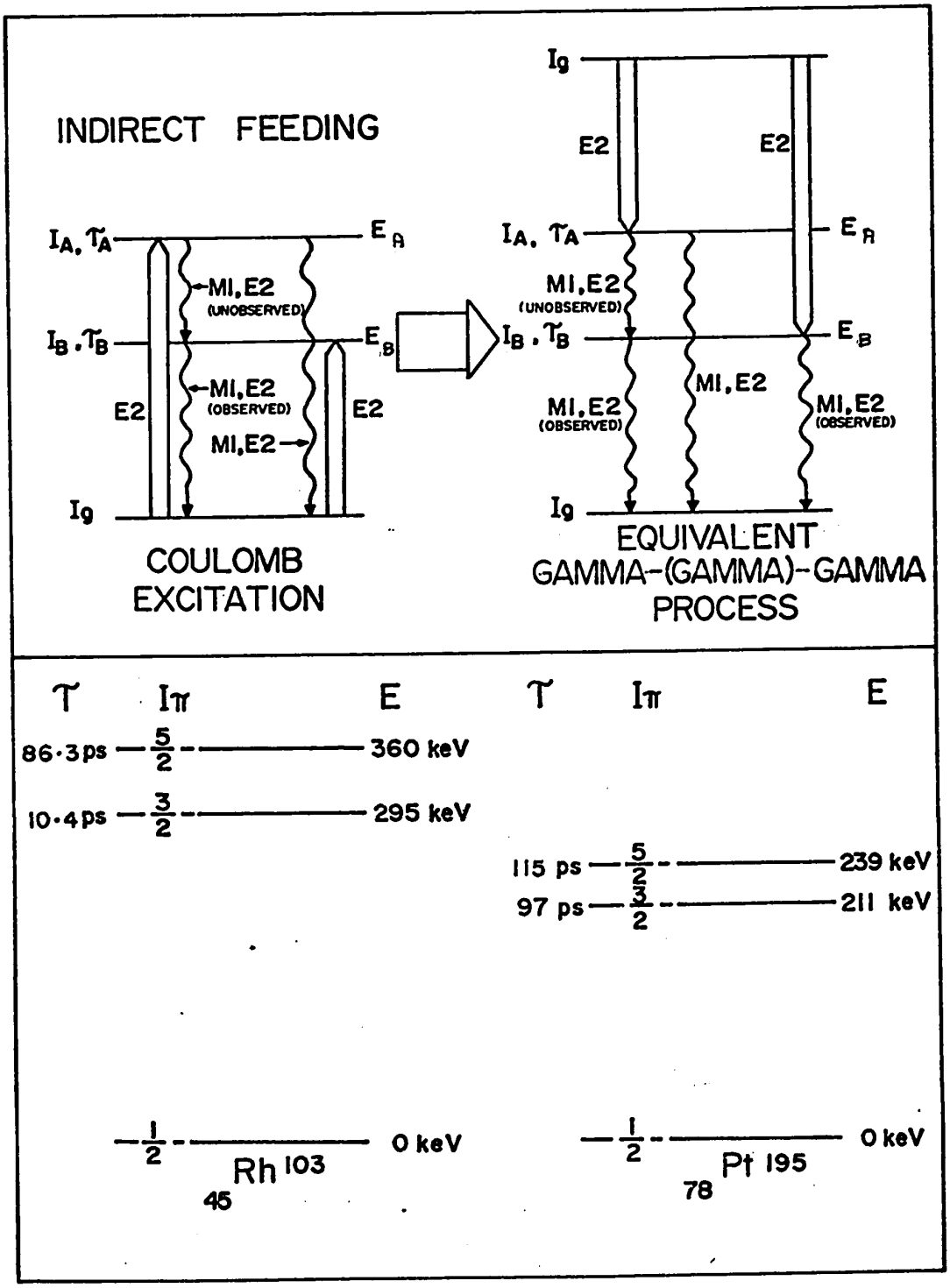
INDIRECT FEEDING
I_A, τ_A
E_A
MI, E2 (UNOBSERVED)
I_B, τ_B
E_B
E2
MI, E2 (OBSERVED)
MI, E2
E2
I_g
COULOMB EXCITATION
I_g
E2
E2
I_A, τ_A
E_A
MI, E2 (UNOBSERVED)
I_B, τ_B
E_B
MI, E2
MI, E2 (OBSERVED)
MI, E2 (OBSERVED)
I_g
EQUIVALENT GAMMA-(GAMMA)-GAMMA PROCESS
τ
Iπ
E
86·3 ps
5/2
360 keV
10·4 ps
3/2
295 keV
Rh 103
45
1/2
0 keV
τ
Iπ
E
115 ps
5/2
239 keV
97 ps
3/2
211 keV
Pt 195
78
1/2
0 keV

Figure B-1

$$I_g(E2)I_A(L_1,L_1')I_B(M1,E2)I_g.$$

Then (indirect) $A_2^i = A_2^{(1)'}U_2A_2^{(2)'}$ where

$$A_2^{(1)'} = F_2(I_A,I_G,2,2)\ a_2^{E2}(\xi_A,\theta_p).$$

$A_2^{(2)'}$ is identical to the factor $A_2^{(2)}$ defined previously.

The function U_2 describes the inevitable attenuation of the angular distribution due to the undetected intermediate radiation, and is given by:

$$U_2 = -\frac{W(I_B,I_A,I_B,I_A;L_1L_1') + \delta_1^2 W(I_B,I_A,I_B,I_A;L_1',L_1')}{1+\delta_1^2}$$

where W is a Racah coefficient and

$$\delta_1^2 = \text{Intensity } (L_1')/\text{Intensity } (L_1).$$

The ratio of A_2 coefficients for indirect and direct processes is given by

$$\frac{A_2^i}{A_2^d} = \frac{a_2(\xi_A,\theta_p)}{a_2(\xi_B,\theta_p)}\ \frac{F_2(I_A,I_G,2,2)}{F_2(I_B I_G,2,2)} \cdot U_2.$$

The values of ξ will change as the projectile energy E_p changes, so one can write

$$\frac{A_2^i}{A_2^d} = R_2(E_p,\theta_p).$$

A similar analysis may be applied to the A_4 coefficients, yielding

$$\frac{A_4^i}{A_4^d} = R_4(E_p,\theta_p).$$

One can write a proportionality relation

$$W(\theta)_{d+i} \propto N_d(1+a_2^d A_2^d P_2(\cos\theta) + a_4^d A_4^d P_4(\cos\theta))$$

$$+ N_i(1 + a_2^i A_2^i P_2(\cos\theta) + a_4^i A_4^i P_4(\cos\theta))$$

where the symbols "d" and "i" refer to the direct and indirect processes respectively and N_d and N_i are the numbers of observed gamma-rays from level B resulting from the direct and indirect feeds, for a particular projectile backscatter angle θ_p, excluding the dependence on gamma-ray emission angle.

$$N_d = [(\text{beam flux}) \times (\text{detector solid angle}) \times (\text{detector efficiency})] \times \left(\frac{d\sigma}{d\Omega}\right)_B$$

where $\left(\frac{d\sigma}{d\Omega}\right)_B$ is the differential Coulomb excitation crossection for level B.

$$N_i = [\qquad\qquad] \times \left(\frac{d\sigma}{d\Omega}\right)_A \times \frac{I_{total}^{A-B}}{I_{total}^{A-G}}$$

where the last term is the ratio of total (gamma-ray + internal conversion electron) intensities for the transitions from level A to B and from level A to the ground (G) state. We define

$$r = \frac{I_{total}^{A-B}}{I_{total}^{A-G}} .$$

For a particular choice of projectile and target isotope,

$$\frac{d\sigma}{d\Omega} = (\text{constant})(E-\Delta E')B(E2)\ \frac{df}{d\Omega}$$

The factors in the square-bracket and the constant in the

expression for $\frac{d\sigma}{d\Omega}$ are the same for both direct and indirect terms, so they will not affect the resultant angular distribution. With a view to averaging over projectile scattering angle and incident energy, one may write

$$W(\theta)_{d+i} \propto (E-\Delta E'_B)B(E2)_B \left(\frac{df}{d\Omega}\right)_B \times [1 + a_2^d A_2^d P_2(\cos\theta) + a_4^d A_4^d P_4(\cos\theta)]$$

$$+ (E-\Delta E'_A)B(E2)_A \left(\frac{df}{d\Omega}\right)_A \times (r) \times [1 + a_2^i A_2^i P_2(\cos\theta) + a_4^i A_4^i P_4(\cos\theta)],$$

When the double average has been carried out, one finds that

$$W(\theta)_{d+i} = B(E2)_B \bar{c}_o^d [1 + \bar{a}_2^d A_2^d P_2(\cos\theta) + \bar{a}_4^d A_4^d P_4(\cos\theta)]$$

$$+ B(E2)_A (\bar{c}_o^i)(r)[1 + \bar{a}_2^i A_2^i P_2(\cos\theta) + \bar{a}_4^i A_4^i P_4(\cos\theta)]$$

where $\bar{c}_o^d = \int_{\Delta E'}^{E_o} \frac{u_2}{E}\, dE$ is proportional to the thick target yield for direct Coulomb excitation of level B and $\bar{c}_o^i$ is the corresponding quantity for level A. The u_2 function is defined at the end of Chapter 3.

Conventionally, the angle-independent part of the angular distribution is normalized to unity. The resultant angular distribution can be written as:

$$W(\theta)_{d+i} = \alpha'[1+\bar{a}_2^d A_2^d P_2(\cos\theta)+\bar{a}_4^d A_4^d P_4(\cos\theta)]$$

$$+ \beta'[1+\bar{a}_2^i A_2^i P_2(\cos\theta)+\bar{a}_4^i A_4^i P_4(\cos\theta)]$$

where α' and β' are given by

$$\alpha' = \frac{1}{1+s} \ , \ \beta' = \frac{s}{1+s} \quad \text{with } s = \frac{B(E2)_A(\bar{\bar{c}}^i_o)(r)}{B(E2)_B(\bar{\bar{c}}^d_o)}$$

α' and β' can be interpreted as the fractions of the overall angular distribution for level B contributed by the direct and indirect processes respectively. If the angular distributions are described in terms of the coefficients b_o, b_2, and b_4, then

$$W(\theta)_{d+i} = \alpha'[\bar{b}^d_o+\bar{b}^d_2\cos 2\theta+\bar{b}^d_4\cos 4\theta]+\beta'[\bar{b}^i_o+\bar{b}^i_2\cos 2\theta+\bar{b}^i_4\cos 4\theta]$$

where $\bar{b}o = 1 + \frac{1}{4}\bar{\bar{a}}_2A_2 + \frac{9}{64}\bar{\bar{a}}_4A_4$

$$\bar{b}_2 = \frac{3}{4}\bar{\bar{a}}_2A_2 + \frac{5}{16}\bar{\bar{a}}_4A_4 \qquad \bar{b}_4 = \frac{35}{64}\bar{\bar{a}}_4A_4.$$

Again normalizing the angle-independent part to unity, the measured angular distribution coefficients will be

$$\bar{b}^m_2 = \alpha\frac{\bar{b}^d_2}{\bar{b}^d_o} + \beta\frac{\bar{b}^i_2}{\bar{b}^i_o} \quad \text{and} \quad \bar{b}^m_4 = \alpha\frac{\bar{b}^d_4}{\bar{b}^d_o} + \beta\frac{\bar{b}^i_4}{\bar{b}^i_o}$$

where α and β are fractional contributions evaluated using a value of s (defined above) that is multiplied by the factor $\frac{\bar{b}^i_o}{\bar{b}^d_o}$

B. EFFECT ON PERTURBED ANGULAR DISTRIBUTION

For a perturbed angular distribution, one begins with the expression appropriate to a particular projectile scattering angle; first the time-averaging for an integral rotation measurement is carried out to yield, for the indirect process

$$W_i(\theta_\gamma,\infty) \propto \Sigma_k b_k^i \{ \frac{\cos(k\theta_\gamma)[1-k^2(\omega_A\tau_A)(\omega_B\tau_B)] - \sin(k\theta_\gamma)[k(\omega_A\tau_A+\omega_B\tau_B)]e^{-t_s/\tau_A}}{[1+(k\omega_B\tau_B)^2][1+(k\omega_A\tau_A)^2]}$$

$$+ \cos(k\theta_\gamma)[1 - e^{-t_s/\tau_A}] - \sin(k\theta_\gamma)\phi_A\}$$

where t_s is the stopping time of the recoiling ion, and for the direct process,

$$W_d(\theta_\gamma,\infty) \propto \Sigma_k b_k^d \{ \frac{\cos(k\theta_\gamma) - \sin(k\theta_\gamma)[k\omega_B\tau_B]}{[1+(k\omega_B\tau_B)^2]} + \cos(k\theta_\gamma)[1-\exp(-t_s/\tau)]$$

$$- \sin(k\theta_\gamma)\phi_B\} .$$

When direct and indirect terms are combined, θ_γ is set equal to 135°, and the averages over projectile scattering angle and energy are carried out, one finds that

$$W_{d\,i}(\theta_\gamma,\infty) = 1 + 2\omega_B\tau_B\{\alpha\frac{\bar{b}_2^d}{\bar{b}_0^d}(1-\frac{t_s}{\tau_B})[1-(2\omega_B\tau_B)^2] + \beta\frac{\bar{b}_2^i}{\bar{b}_0^i}(1-\frac{t_s}{\tau_A})[1-4((\omega_A\tau_A)^2 + (\omega_B\tau_B)^2)]\}$$

$$+ 2\omega_A\tau_A\{\beta\frac{\bar{b}_2^i}{\bar{b}_0^i}(1-\frac{t_s}{\tau_A})[1-4((\omega_A\tau_A)^2+(\omega_B\tau_B)^2)]\} + \alpha\frac{\bar{b}_2^d}{\bar{b}_0^d}\phi_B$$

$$+ \beta\frac{b_2^i}{b_0^i}\phi_A\} \qquad \text{(B-1)}$$

where the b_4 terms have been omitted because they are zero for the two cases of interest in this thesis.

The above expression involves the following approximations:

$$[1+(k\omega\tau)^2]^{-1} \approx 1-(k\omega\tau)^2 \quad \text{and} \quad e^{-t_s/\tau} \approx 1 - \frac{t_s}{\tau} .$$

Since the largest value of $\omega\tau$ encountered in this thesis is

$\lesssim$ .15 radians and the largest ratio of $\frac{t_s}{\tau}$ = .085 (t_s = .89, τ = 10.4 , for the 295 keV level of 16.3 Mev Rh ions recoiling in iron), these approximations are both valid to better than 1%.

Terms of the form $(1 - \frac{t_s}{\tau})$ and $[1 - 4(\omega\tau)^2]$ are correction terms that differ from 1 by < 10%. If one defines

$$A = 1 - (t_s/\tau_B) \qquad B = 1 - (t_s/\tau_A)$$

$$C = 1 - 4(\omega_B\tau_B)^2 \qquad D = 1 - 4[(\omega_A\tau_A)^2 + (\omega_B\tau_B)^2]$$

and extracts the quantity $\bar{b}_2^m = \alpha \frac{\bar{b}_2^d}{\bar{b}_0^d} + \beta \frac{\bar{b}_2^i}{\bar{b}_0^i}$, expression (B-1) can be rewritten as

$$W_{d+i}(\theta_\gamma, \infty) = 1 + 2\bar{b}_2^m(\omega_B\tau_{eff} + \phi_{eff})$$

with

$$\tau_{eff} = \tau_B\{\frac{1}{\bar{b}_2^m}[(\alpha\frac{\bar{b}_2^d}{\bar{b}_0^d})(AC) + (\beta\frac{\bar{b}_2^i}{\bar{b}_0^i})(BD) + (\frac{g_A\tau_A}{g_B\tau_B})(\beta\frac{\bar{b}_2^i}{\bar{b}_0^i})(BD)]\}$$

and

$$\phi_{eff} = \frac{1}{\bar{b}_2^m}[\alpha \frac{\overline{\overline{b_2^d\phi_B}}}{\bar{b}_0^d} + \beta \frac{\overline{\overline{b_2^i\phi_A}}}{\bar{b}_0^i}].$$

In the expression for τ_B, the static rotation angle $\omega_A\tau_A$ has been written in terms of $\omega_B\tau_B$ using the fact that the internal field must be the same for both states $(\frac{\omega_A}{g_A} = \frac{\omega_B}{g_B})$.

Since ω_B and ϕ_{eff} both change sign when the external field direction is reversed, the measured rotation angle in our experiment corresponds to

$$\Delta\theta = \frac{1}{2\bar{b}_2^m}(\frac{Q-1}{Q+1}) = \omega_B\tau_{eff} + \phi_{eff} \qquad \text{(B-2)}$$

Written this way, the rotation angle can be interpreted as a point on a straight line, with slope ω_B and mean life τ_{eff}. From this point of view, one sees that the effects of indirect feeding of state B via state A are: (1) to produce an effective mean life for state B that is larger than τ_B (if g_A and g_B have the same sign), and (2) to produce a transient field effect that is a linear combination of the effects for state A and state B separately.

The relative importance of the correction factors A, B, C, and D depends mainly upon the mean lives of states A and B. Indirect feeding tends to be important in a relative sense when $\tau_A >> \tau_B$ as is the case with ^{103}Rh for which τ_A = 86.3 psec and τ_B = 10.4 psec. For this case, $A = 1 - \frac{t_s}{\tau_B}$, and B = 1, C = 1, $D = 1-4(\omega_A\tau_A)^2$, to better than 1%. On the other hand for ^{195}Pt, τ_A = 115 psec and τ_B = 97 psec, so A = 1, B = 1 to better than 1%, and $C = 1-4(\omega_B\tau_B)^2$, $D = 1-4[(\omega_A\tau_A)^2 + (\omega_B\tau_B)^2]$.

The use of an effective mean life τ_{eff} is somewhat awkward because the value of τ_{eff} is dependent upon the g factors of states A and B; as a result, this tends to obscure the role of the g factors in the data analysis. A more direct approach to the indirect feeding correction can be made by working directly from Equation B-1. For ^{103}Rh it can readily be shown that

$$\Delta\theta_B^{corrected} = \Delta\theta_B^{meas} - \frac{\beta}{\bar{b}_2^m}\left(\frac{\bar{b}_2^i}{\bar{b}_o^i}\right)\Delta\theta_A^{meas}$$

where

$$\Delta\theta_A^{meas} = \omega_A\tau_A[1-4(\omega_A\tau_A)^2] + \frac{\overline{\overline{b_2^i\phi_A}}}{\bar{b}_2^i} .$$

Then

$$\Delta\theta_B^{corrected} = \omega_B\tau_B \frac{1}{\bar{b}_2^m}\{\alpha(\frac{\bar{b}_2^d}{\bar{b}_o^d})(1 - \frac{t_s}{\tau}) + \beta(\frac{\bar{b}_2^i}{\bar{b}_o^i})[1-4(\omega_A\tau_A)^2]\} + \frac{\alpha}{\bar{b}_2^m}(\frac{\overline{\overline{b_2^d\phi_B}}}{\bar{b}_o}) .$$

If the correction factors $1 - \frac{t_s}{\tau}$ and $1-4(\omega_A\tau_A)^2$ are ≈ 1, then the factor multiplying $\omega_B\tau_B \approx 1$. For ^{103}Rh, $\omega_A\tau_A \approx .12$ and $t_s/\tau \sim .086$ so $1-4(\omega_A\tau_A)^2 \approx .94$ and $1-t_s/\tau \approx .91$. Since β is small, the factor multiplying $\omega_B\tau_B$ will be $\approx .94$. This number is subject to a few percent uncertainty due to the uncertainty in the values of t_s and τ. However, the value of τ_B is small (10.4 psec), so a 10% effective reduction in its value is not going to affect the results in a significant way. In the data analysis of the results for $Fe_{80}Rh_{20}$ alloy reported in the text, the multiplying factor for $(\omega\tau)_{295}$ has been assumed = 1. With regard to the transient field term, using this method of analysis, the effect of the inclusion of indirect feeding is, roughly speaking, to attenuate the observed transient rotation for state B by a factor α ($\sim$ .80 for Rh); the averaging over projectile scattering angle and energy can also affect the observed rotation value (see Figure 3-2).

For ^{195}Pt, the same kind of analysis can be applied. The $1 - \frac{t_s}{\tau}$ correction terms are both negligible, but the correction terms of the form $1-4(\omega\tau)^2$ can be as small as .95 for <u>both</u> A and B states because the mean life of both of these states is $\sim$ 100 psec.

The static rotation of state B then looks like:

$$(\omega_B\tau_B)[1-4(\omega_B\tau_B)^2]\{\frac{1}{\bar{b}_2^m}(\alpha(\frac{\bar{b}_2^d}{\bar{b}_o^d}) + \beta(\frac{\bar{b}_2^i}{\bar{b}_o^i})[1-4(\omega_A\tau_A)^2])\}$$

$\omega_A\tau_A$ can be approximated by $\Delta\theta_A^{meas}$. For the 239 kev state in ^{195}Pt, $\Delta\theta_A \sim .09$, so $1-4(\omega_A\tau_A)^2 \sim .97$; the correction is not serious and has been ignored for the analysis of the 211 kev state.

The second method of analysis (in which the measured rotation angle of state A is used to correct the rotation angle to state B) has been employed in this thesis because the role of the nuclear g factors in the data analysis is easier to interpret for this method. The indirect feeding calculations for the 295 kev state in ^{103}Rh and the 211 kev state in ^{195}Pt are summarized in Table 5-2.

REFERENCES

ABBREVIATIONS USED:

HSNR - Hyperfine Structure and Nuclear Radiations, ed. E. Matthias and D. A. Shirley (North Holland Publishing Company (1968).

HIEN - Hyperfine Interactions in Excited Nuclei, Gordon and Breach Science Publishers Inc., (1971).

A1 K. Alder, A. Bohr, T. Huus, B. Mottelson and A. Winther, Rev. Mod. Phys. 28, No. 4 (1956), 432.

A2 K. Alder, E. Matthias, W. Schneider, and R. M. Steffen, Phys. Rev. 129 (1963), 1199.

A3 H. Aeppli, et al., Phys. Rev. 84 (1951), 370.

A4 A. P. Agnihotry, Y. K. Agarwal, S. K. Bhattacherjee, H. C. Jain, M.C. Joshi, P. N. Tandon, T. R. Miller, International Conference on Nuclear Moments and Nuclear Structure, Osaka, Japan (1972). J. Phys. Soc. Japan (Supplement), to appear.

A5 K. Auerbach, K. Siepe, J. Wittkemper, H. J. Körner, Phys. Lett. 23 (1967), 367.

A6 Y. K. Agarwal, C. V. K. Baba, S. K. Bhattacherjee, Nucl. Phys. 79 (1966), 437.

A7 K. Auerbach, B. Harns, K. Siepe, J. Wittkemper, H. J. Körner, Phys. Lett. 23 (1966), 367.

A8 D. Agresti, E. Kankeleit, B. Persson, Phys. Rev. 155 (1967), 1339.

A9 M. Atac, P. Debrunner, H. Fraunfelder, Phys. Rev. Lett. 21 (1966), 699.

A10 A. Aharoni, HIEN, Vol. 1, p. 75.

A11 H. Appel and W. Mayer, Nucl. Phys. 43 (1963), 393.

B1 H. Bernas, M. O. Ruault, and B. J. Jouffrey, Phys. Rev. Lett. 27 (1971), 859.

B2 E. M. Baroody, Phys. Rev. 112 (1958), 1571.

B3 R. R. Borchers, HIEN, Vol. 4 (1971), 31.

B4 E. L. Brady, M. Deutsch, Phys. Rev. 78 (1950), 558.

B5 A. E. Berkowitz, F. J. Donahue, A. D. Franklin, R. D. Steijn, Acta. Met. 5 (1957), 1.

B6 S. K. Bhattacherjee, H. G. Devare, H. C. Jain and M.C. Joshi, HIEN, Vol. 4 (1971), 1081.

B7 I. Berkes, R. Rougny, M. Meyer-Lévy, R. Chéry, J. Danière, G. Lhersonneau, A. Troncy, Phys. Rev. C6 (1972), 1098.

B8 J. L. Black, W. J. Caelli, and R. B. Watson, Nuclear Phys. A125 (1969),545.

B9 J. D. Bowman, E. N. Kaufmann, S. K. Bhattacherjee, M. Levanoni, Phys. Rev. Lett. 20 (1968),1179.

B10 A. Buyrn, L. Grodzins, MIT Progress Report 2098, #142 (1964).

B11 R. Béraud, I. Berkes, J. Danière, M. Lévy, G. Marest, R. Rougny, H. Bernas, D. Spanjaard, HSNR (1968) 199.

B12 N. Benczer-Koller, J. R. Harris, G. M. Rothberg, Phys. Rev.140 (1965), B547.

C1 C. C. Chao, P. Duwez, C. C. Tsuei, J. Appl. Phys. 42, No. 11 (1971), 4282.

C2 D. C. Camp, A. L. Van Lehn, Nuclear Inst. and Meth. 76 (1969), 192.

C3 J. A. Cameron, A. W. Gibb, D. B. Kenyon, and L. Keszthelyi, Phys. Rev. Lett. 24, No. 9 (1970), 468.

G1 R. L. Graham, D. Ward, J. S. Geiger, AECL Report #3668.

G2 A. Gal, Phys. Lett. 20 (1966), 414.

G3 Y. Grunditz, S. Autman, M. Petterson, M. Saraceno, Nucl. Phys. A133 (1969), 369.

H1 Hyperfine Interactions, ed. A. J. Freeman and R. B. Frankel (Academic Press, New York, 1967).

H2 G. M. Heestand, Ph.D. Thesis, University of Wisconsin (1969).

H3 B. Herskind, R. R. Borchers, J. D. Bronson, D. E. Murnick, L. Grodzins, R. Kalish, HSNR, p. 735.

H4 J.C. Ho, N. E. Phillips, Phys. Rev. 140 (1965), A648.

J1 K. Johansson, L. O. Norlin, G. Carlsson, Arkiv Fysik 37 (1968), 445.

K1 G. H. Kinchin and R. S. Pease, Reports on Progress in Physics , No. 18 (1955), 1.

K2 B. T. Kelly, Irradiation Damage to Solids, Pergamon Press (1966).

K3 G. M. Kalvius, G. D. Sprouse, and S. S. Hanna, HSNR, North Holland (1968), 686.

K4 M. Kontani and J. Itoh, J. Phys. Soc. Japan 22 (1967), 345.

K5 M. Kontani, M. Ota, Y. Masudor, J. Phys. Soc. Japan 29 (1970), 1194.

K6 A. Kussmann and G. Rittberg, Metallkunde 41 (1950), 470.

K7 H. W.Kugel, R. R. Borchers, R. Kalish, Nucl. Phys. A137 (1969), 500.

K8 L. Keszthelyi, I. Berkes, Dészi, L. Pócs, Nucl. Phys. 71, (1965) 662.

K9 L. Keszthelyi, I. Demeter, Z. Szökefalvi-Nagy, L. Varga and G. Mezei, Phys. Stat. Sol. 52 (1972), 149.

K10 R. Kalish, L. Grodzins, R. R. Borchers, J. D. Bronson, B. Herskind, Phys. Rev. 161 (1967), 1196.

K11 R. Kalish and W. Kossler, HSNR, p. 752.

K12 P. G. Kerr, A.W. Gibb and J. A. Cameron, Can. J. Phys. (1973), in press.

K13 D. B. Kenyon, L. Keszthelyi, J. A. Cameron, Can. J. Phys. 48 (1970), 2730.

L1 J. Lindhard and A. Winther, Nucl. Phys. A166 (1971), 413.

L2 J. Lindhard, M. Scharff and H. E. Schiott, Mat. Fys. Medd. Dan. Vid. Selsk 33, No. 14 (1963).

L3 G. Liebfried, Radiation Damage in Solids, Proc. International School of Physics, Academic Press Inc., New York (1962) 227.

M1 M. Marmor, S. Cochavi and D. B. Fossan, HIEN, Vol. 1 (1971), 83.

M2 F. R. Metzger, Nuclear Physics 27 (1961), 612.

M3 F. K. McGowan and P. Stelson, Phys. Rev. 106 (1957), 522.

M4 F. K. McGowan and P. H. Stelson, Phys. Rev. 109 (1958), 901.

M5 J. Murray, T. A. McMath, J. A. Cameron, Can. J. Phys. 45 (1967), 1813.

M6 F. K. McGowan, P. H. Stelson, Phys. Rev. 116 (1959),154.

M7 D. E. Murnick et al, Proc. Roy. Soc. A311 (1969),111.

M8 J. Murray, T. A. McMath, J. A. Cameron, Can. J. Phys. 46 (1968), 75.

N1 Nuclear Data Sheets, A=195, ^{195}Pt.

R1 W. M. Roney, H. W. Kugel, G. M. Heestand, R. R. Borchers, and R. Kalish, Nuclear Reactions Induced by Heavy Ions, ed. R. Bock and W. R. Hering (North Holland, Amsterdam. 1960), 419.

S1 R. M. Steffen and H. Fraunfelder, Perturbed Angular Correlations, North Holland, Amsterdam (1964), 3.

S2 G. Shirane, C. W. Chen, P. A. Flinn, Phys. Rev. 131 (1963), 183.

S3 R. G. Stokstad, R. A. Moline, C. A. Barnes, F. Boehm, and A. Winther, HSNR, 699.

S4 G. D. Sprouse, HIEN, Vol. 3, 931.

S5 Z. Szökefalvi-Nagy, I. Demeter, L. Keszthelyi, G. Mezei and L. Varga, Nucl. Phys. A196 (1972), 858.

S6 R. O. Sayer, J. K. Temperly and D. Eccleshall, Nucl. Phys. A179 (1972),122.

V1 L. Varga, I. Demeter, L. Keszthelyi, G. Mezei, Z. Szökefalvi-Nagy, Phys. Rev. C6 (1972),388.

W1 A. Winther and J. de Boer, Coulomb Excitation, Academic Press (1966), 303.

W2 A. Winther, HIEN, Vol. 4 (1971), 1063.

Omissions :

G4 M.A.Grace,C.E. Johnson, N. Kurti, R.G. Scurlock, R.T.Taylor, Phil. Mag 4 (1955), 948.

S7 B.N. Samoilov, V.V. Skylarevskii, E.P. Stepanov, Soviet Phys. JETP 9 (1959), 972.